ABSTRACT

COMBUSTION OF NANOCOMPOSITE THERMITE POWDERS

by
Ian W. Monk

This work investigates combustion of nanocomposite thermite powders prepared by arrested reactive milling (ARM). The focus is on how ARM as a top-down approach to nano-thermite building generating fully-dense nanocomposite particles with dimensions of 1–100 μm affects the rates and mechanism of their combustion. A variety of thermites are milled using both aluminum and zirconium as fuels combined with several oxidizers (WoO_3, MoO_3, CuO, Fe_2O_3, and Bi_2O_3). The powders are ignited using both an electrostatic discharge (ESD) and a CO_2 laser beam.

A range of parameters vary in the first set of experiments in order to broadly understand the underlying combustion mechanisms of nanocomposite thermite powders. Only the aluminum thermites are considered in these experiments and had their particle sizes, preparation method (milled, mixed, or electrosprayed), and milling times adjusted in order to see their effects on combustion. Additionally the ESD ignition experiments vary the environment between air, argon, and vacuum, as well as varying the ignition voltages from 5 up to 20 kV at a constant capacitance of 2000 pF. The ignited particles are monitored using a photomultiplier tube (PMT) equipped with an interference filter. It is observed that the reaction rates of the ESD-initiated powders are unaffected by their particle size but are affected by their scale of mixing between their fuel and oxidizer within the particles themselves. The different preparation methods play a significant role in determining the powders performance. Mixed nano-powders agglomerated quite easily, which hinder their combustion performance. The electrosprayed powders perform well in all environments, and the milled powders perform best in oxidizer-free environments (when no reoxidation of the oxidizer could occur).

A set of experiments employing ESD ignition focus on the effects of powder load on its combustion properties. The experiments utilize a similar PMT setup with an additional 32-channel PMT coupled with a spectrometer to record optical emission in the range of 373-641 nm. It is discovered that when a monolayer of the powder was ignited, only single particles are ejected from the substrate and burned very rapidly. A thicker layer of powder (0.5 mm) struck by ESD produce an aerosol cloud, which ignite with a delay and burn substantially longer. It is theorized that the difference was due to different heating rates between the two experiments. In monolayer experiments, all ignited particles are ignited directly by ESD. Only a small fraction of particles in the thicker layered powder is heated directly by ESD; most particles are heated slower due to heat transfer from the initially ignited powder. More in depth experiments on the heating rate are conducted utilizing the fast heating of the thermites powders by ESD at ca. 10^9 K/s along with an experiment, in which the same thermite particles are heated and ignited by laser with the heating rate of ca. 10^6 K/s. It is discovered that laser-ignited particles combusted slower due to a loss of their nanostructure, while ESD-ignited particles maintained their nanostructure and burned much more quickly.

Utilizing the results from all the experiments, and combining them with combustion information previously obtained for Al and its ignition, with reaction controlled by polymorphic phase transformations in alumina (amorphous, gamma, and alpha), a model is developed enabling one to describe quantitatively the very high burn rates observed for the nanothermite particles rapidly heated by ESD. The model considers nanostructure accounting for the inclusion size distribution obtained from SEM images of actual milled particles, along with other considerations including heat loses, phase transformations, density changes, and particle size. The model is able to match combustion times and temperatures with those recorded from the earlier ESD combustion experiments.

COMBUSTION OF NANOCOMPOSITE THERMITE POWDERS

by
Ian W. Monk

A Dissertation
Submitted to the Faculty of
New Jersey Institute of Technology
in Partial Fulfillment of the Requirements for the Degree of
Doctor of Philosophy in Chemical Engineering

Otto H. York Department of Chemical and Materials Engineering

May 2018

APPROVAL PAGE

COMBUSTION OF NANOCOMPOSITE THERMITE POWDERS

Ian William Monk

Dr. Edward L. Dreizin, Dissertation Advisor — Date
Distinguished Professor of Chemical Engineering, NJIT

Dr. Robert B. Barat, Committee Member — Date
Professor of Chemical Engineering, NJIT

Dr. Mirko Schoenitz, Committee Member — Date
Associate Research Professor of Chemical Engineering, NJIT

Dr. Roman S. Voronov, Committee Member — Date
Assistant Professor of Chemical Engineering, NJIT

Dr. Demitrios Stamatis, Committee Member — Date
Research Engineer, Naval Sea Systems Command, Indian Head Division

BIOGRAPHICAL SKETCH

Author: Ian William Monk

Degree: Doctor of Philosophy

Date: May 2018

Undergraduate and Graduate Education:

- Doctor of Philosophy in Chemical Engineering,
  New Jersey Institute of Technology, Newark, NJ, 2018

- Bachelor of Science in Chemistry,
  Bucknell University, Lewisburg, PA, 2011

Major: Chemical Engineering

Presentations and Publications:

Monk, I., Schoenitz, M., Dreizin, E.L., *The Effect of Heating Rate on Combustion of Fully Dense Nanocomposite Thermite Particles*. *Combustion Science and Technology* 190 (2), p. 203-221 (2018).

Monk, I., *Rapid Reactions in Fully Dense Reactive Nanocomposite Materials*. Presented at the Materials Research Society (MRS) Annual Fall Meeting, Boston, MA, November 2017.

Monk, I., *Effect of Heating Rate on Combustion of Reactive Nanocomposites MgS and ZrS*. Presented at the AIChE Annual Meeting, Minneapolis, MN, November 2017.

Valluri, S. K., Monk, I., Schoenitz, M., Dreizin, E. L., *Fuel Rich Aluminum Metal Fluoride Composites*. Presented at the AIChE Annual Meeting, Minneapolis, MN, November 2017.

Monk, I., *A Correlation of Heating Rates and Combustion Dynamics for Fully-dense Nano-composite Thermite Powders.* Presented at the Defense Threat Reduction Agency (DTRA) Annual Review, McLean, VA, July 2017.

Monk, I., Schoenitz, M., Jacob, R.J., Dreizin, E.L., Zachariah, M.R., *Combustion Characteristics of Stoichiometric Al-CuO Nanocomposite Thermites Prepared by Different Methods*. *Combustion Science and Technology* 189 (3), pp. 555-574 (2017).

Monk, I., Schoenitz, M., Dreizin, E.L. *Modes of Ignition of Powder Layers of Nanocomposite Thermites by Electrostatic Discharge*. *Journal of Energetic Materials* 35 (1), p. 29-43 (2017).

Monk, I., *Effect of Heating Rate on Combustion of Nano-Composite Thermites Prepared by Arrested Reactive Milling*. Presented at the AIChE Annual Meeting, San Francisco, CA, November 2016.

Monk, I., *A Correlation of Heating Rates and Combustion Dynamics for Fully-dense Nano-composite Thermite Powders*. Presented at the Gordon Research Conference Meeting, Stowe, VT, July 2016.

Monk, I., *Electrostatic Discharge Ignition of Stoichiometric Al-CuO Nanocomposite Thermites Prepared by Various Means*. Presented at the Combustion Institute Annual Meeting, Princeton, NJ, March 2016.

Monk, I., *Combustion Regimes for Spark Ignited Nanocomposite Thermites*. Presented at the AIChE Annual Meeting, Salt Lake City, UT, November 2015.

Monk, I., Williams, R., Liu, X., Dreizin, E.L., *Electro-static discharge ignition of monolayers of nanocomposite thermite powders prepared by arrested reactive milling*. *Combustion Science and Technology* 187 p. 1276–1294 (2015).

Monk, I., *Nanocomposite Thermite ESD Ignition of Mono-layers*. Presented at the Materials Research Society (MRS) Annual Fall Meeting, Boston, MA, December 2014.

Monk, I., *Nanocomposite Thermite ESD Ignition of Mono-layers*. Presented at the AIChE Annual Meeting, Atlanta, GA, November 2014.

I would like to dedicate this work to my parents, John and Kathy Monk. Who have always supported my pursuits and dreams throughout my life, and been there every step of the way.

ACKNOWLEDGEMENT

I would like to thank my research advisors Dr. Edward Dreizin and Dr. Mirko Schoenitz for all their guidance and patience seeing me through my research.

Additional thanks to my thesis committee members, Dr. Robert Barat, Dr. Roman Voronov, and Dr. Demitrios Stamatis for their valued input and time in helping me improve upon my work.

I'd like to thank the Army Research Office (ARO) and the Air Force Office of Scientific Research (AFOSR) for their invaluable funding to allow me to pursue my research.

I would further like to thank my research group for always being there to lend invaluable advice

Finally I would like to thank my family for their constant support in the pursuit of my goals.

TABLE OF CONTENTS

TABLE OF CONTENTS
(Continued)

TABLE OF CONTENTS
(Continued)

TABLE OF CONTENTS
(Continued)

LIST OF TABLES

LIST OF FIGURES

LIST OF FIGURES
(Continued)

LIST OF FIGURES
(Continued)

LIST OF FIGURES
(Continued)

LIST OF FIGURES
(Continued)

LIST OF FIGURES
(Continued)

CHAPTER 1

INTRODUCTION

Reactive materials have been of interest to humankind as far back as our history dates. Wars, entertainment, mining, industrialization, space exploration, etc., accompanying the human progress stimulated our continued fascination with various reactive materials including solid fuels, like coal, explosives like gunpowder, fuel additives such as magnesium, aluminum, and pyrotechnics like thermites. Of these materials, thermites represent a "newer" addition to our arsenal of reactive materials. The first instance of thermite recorded in history came from the work of a German chemist named Hans Goldschmidt. Originally looking for a way to smelt ores without the use of carbon, he stumbled upon the reaction of a metal fuel (in his case, aluminum) being oxidized by a metal oxide oxidizer, such as rust (Fe_2O_3). Goldschmidt patented this reaction and used it to weld train tracks together throughout Germany [1-3], an application of thermites still in use today.

1.1 Limitations and Problems of Conventional Thermites

As described earlier, thermite reactions utilize a metal fuel and metal oxidizer to produce large heat release (and molten metals used in welding) in highly exothermic reactions. For example,

$$Al + Fe_2O_3 \xrightarrow{yields} Al_2O_3 + 2Fe \qquad 1.1$$

This reaction can produce about -850 kJ/mol and reach temperatures greater than 3000 K [4, 5]. The high temperatures allow thermites to be used in a variety of applications including welding [6, 7], preparation of cermet and ceramics [8, 9], and in incendiary/pyrotechnics [10, 11]. While the large heat release from these materials is highly desirable along with their high energy densities, conventional thermites have low reaction rates related to the transport processes of reacting species through condensed phases [12-16]. This limits their usability in such energetic systems as explosives where common monomolecular formulations, including TNT, HMX, RDX and CL-20 achieve much greater reaction rates. In an effort to approach similar reaction kinetics as the monomolecular formulations, current research is attempting to increase the mass transfer rates of the reaction in thermites by reducing the mixing length scales of the components: fuel and oxidizer [15, 17-19].

1.2 Nanocomposite Energetics

Reducing the length scales of these composite thermites can be done in a couple of ways. One of the most popular ways involves the "bottom-up" approach to composite formulations. This approach involves starting with nanomaterials (or nanoparticles of individual components) and combining them to create the nanocomposite thermites. This preparation allows for a convenient control over the composite composition. The "bottom-up" assembly methods includes mixing of powders, typically, assisted by ultrasonic agitation [14, 20-22], electrospray [23, 24], xerogel [25, 26], electrostatic self-

assembly [27], electrophoretic deposition [28, 29], and direct deposit lamination [29]. There are however, systemic problems common for all preparation methods of metal-based nanocomposite materials using nanomaterials as an initial building block. Nano-aluminum, for example, must be passivated; otherwise it can be rather dangerous to safely handle the material for risk of accidental ignition [30, 31]. While passivating the aluminum allows for safer handling it will decrease its overall energy density. Other problems with nanomaterials include agglomeration of particles. This can be seen in many nano-sized materials but is especially apparent in commercially available nano-boron [32] as illustrated in Figure 1.1 [33].

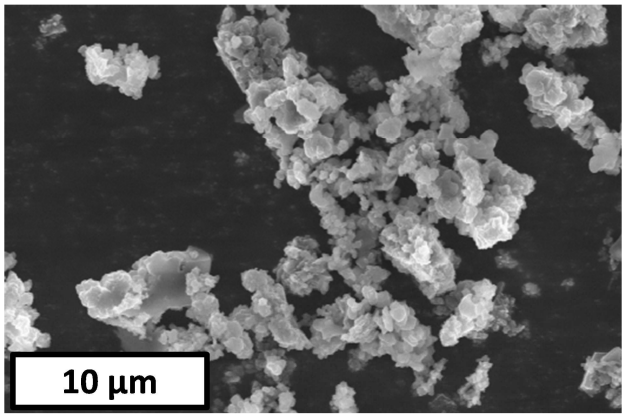

Figure 1.1 Commercially available nano-boron (agglomerated).
Source: [33].

Other problems arise for self-assembly in terms of their homogeneity. During assembly particles construct at random and without order creating inhomogeneity. To correct for this additives such as surfactants are used to create an ordered assembly of the particles; however, by adding a surface functionalizing agent for assembly energy density is decreased and porous systems are created [34-38]. A newer "bottom-up" method of assembly attempts to circumvent the problems faced by the other methods mentioned

earlier. This method utilizes molecular deposition like magnetron sputtering to create nanofoils [39, 40]. These multilayered materials allow for self-propagating high-temperature synthesis (SHS) reactions to take place between the layers (usually made up of Al-Ni). Additionally these nanofoils offer greater control over layer size and composition, allowing for greater homogeneity and consistency of the compositions in the layers [41-43]; however, scale-up for manufacturing is expensive. In addition, aside from selected niche applications, materials in the shape of foils are impractical and powder-like reactive materials are desired. More information is needed on bulk shapes built using nanolayered design, as mostly thin foils tested in laboratory settings have been used to investigate properties of such nanolaminate materials [44].

Another way to create these nanocomposite thermites is the "top-down" approach. This involves utilizing micron-sized materials as the starting components and creating nanoscale interfaces through the composite formulation processes. An example of this type of approach is milling, specifically Arrested Reactive Milling (ARM) [13, 45]. Disadvantages to this method include contamination of the material from the milling media and inconsistency in the material mixing. However, this method provides easy scalability and preparation suitable essentially for any combination of material components. The interfaces are created by mechanical attrition and shear, resulting in no passivating layer (such as an oxide, normally covering surfaces of commercial metal powders) present at the reactive interfaces [17]. The reactive interfaces created by the milling process occur all throughout the particle, as shown in Figure 1.2, allowing for high reaction rates. Additionally this versatile method allows for nanocomposite particles that are fully dense and contain no inert additives [13, 45, 46].

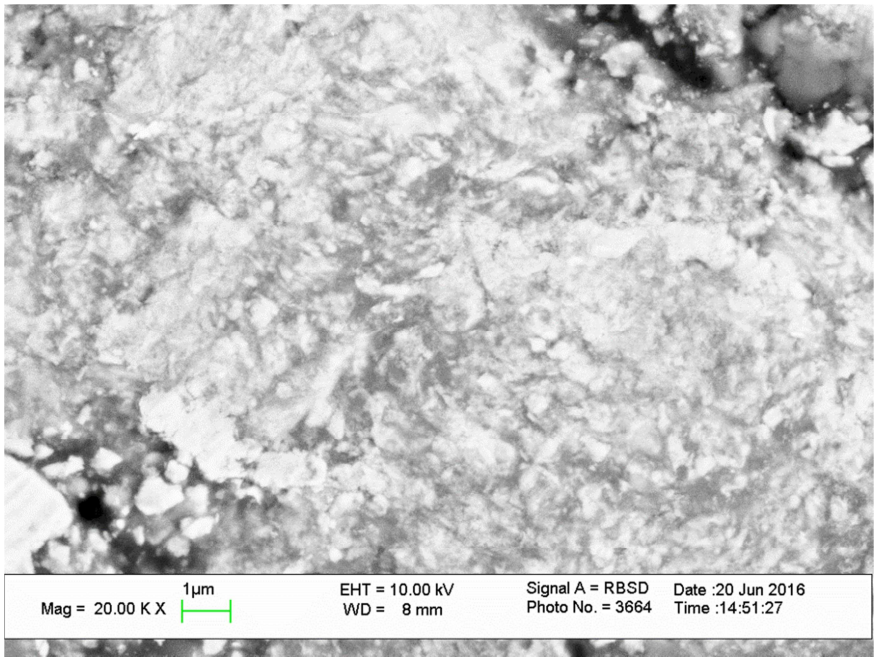

Figure 1.2 ARM prepared 2Al-3CuO thermite (CuO "white" material, Al "dark gray" material).

1.3 Previous Work on ARM Prepared Nanocomposite Thermites

In previous work, a large variety of ARM prepared nanocomposite thermites have been made, as shown in Table 1.1, where selected Al-based thermites are listed. Research have focused largely on aluminum as a fuel combined with different metal oxide oxidizers. The fuel/oxidizer ratios varied from an ideal stoichiometric ratio (e.g., 2Al-3CuO) to fuel rich ratios (e.g., 12Al-3CuO). Milling of these materials was carried out in a variety of mills including a SPEX Certiprep 6815 Freezer/Mill (FM) [47], an 8000 series by Spex CertiPrep shaker mill (SM) [48, 49], and a Retsch 400 PM planetary mill (PM) [50]. Most formulations utilized the planetary mill for its larger loadings (30g) over the other two mills (5g) and its ease of use. The most consistently used milling media in preparation of reactive composites was hardened steel balls, with a process control agent

of hexane to minimize partial reactions that may occur during milling as well as prevent cold welding [51].

Table 1.1 Various Aluminum-based Nanocomposite Thermites Prepared by ARM

Fuel	Oxidizer	Stoichiometries Fuel:Oxidizer (mols)	Mill	Ref.
Al	CuO	2:3, 8:3, 10:3, 12:3	PM*, CM, SM	[18, 47, 50, 52-60]
	MoO_3	2:1, 4:1, 8:1, 12:1, 16:1	PM, SM	[48-50, 54, 56-58, 60-63]
	Fe_2O_3	4:1	PM	[60]
	Bi_2O_3	2.35:1	PM	[60]

*PM – Planetary Mill, CM – Cryomill, SM – Shakermill

Characterization of the composites was carried out by various methods. For thermoanalytical techniques, differential scanning calorimetry (DSC) and thermogravimetric analysis (TGA) was utilized. These provided information about phase changes and reactions that the composites were undergoing as can be seen in Figure 1.3. It shows a sequence of exothermic events occurring in the sample upon its heating, in this case for the 8Al-MoO_3 nanocomposite [61]. Peak positions as a function of the heating rate are studied to determine the reaction kinetics for each reaction; areas under the peaks are used to assess the associated heat release. These data are later correlated with the ignition experiments for the same materials, in which samples are heated at much greater rates than in DSC/TGA experiments.

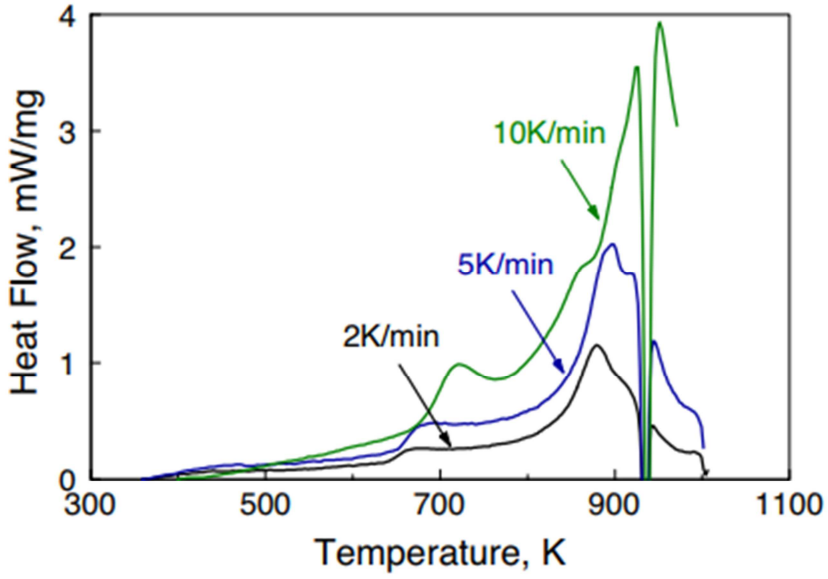

Figure 1.3 DSC curves for nanocomposite 8Al-MoO_3.
Source: [61].

For particle ignition and combustion tests, a broad variety of equipment and methods were used. These included devices such as a heated wire ignition setup [49, 53, 59, 60, 63], constant volume explosion chamber (CVE) [48], an electrostatic discharge (ESD) apparatus [50], and a CO_2 laser ignition setup [62, 64]. These allowed for pressures, temperatures, and other various combustion performance parameters to be ascertained. In the case of wire ignition, which was used most frequently, as shown in Figure 1.4a, ignition temperatures and emission traces were typically captured. Powder was placed on a Ni-Cr filament (Figure 1.4b) then a current was run through the wire, producing varying heating rates depending on the voltage used, which then could be correlated to the ignition temperature (temperature at which the composite would ignite off the wire filament). Figure 1.5 shows a correlation between ignition temperatures for various thermites and their corresponding heating rates [60].

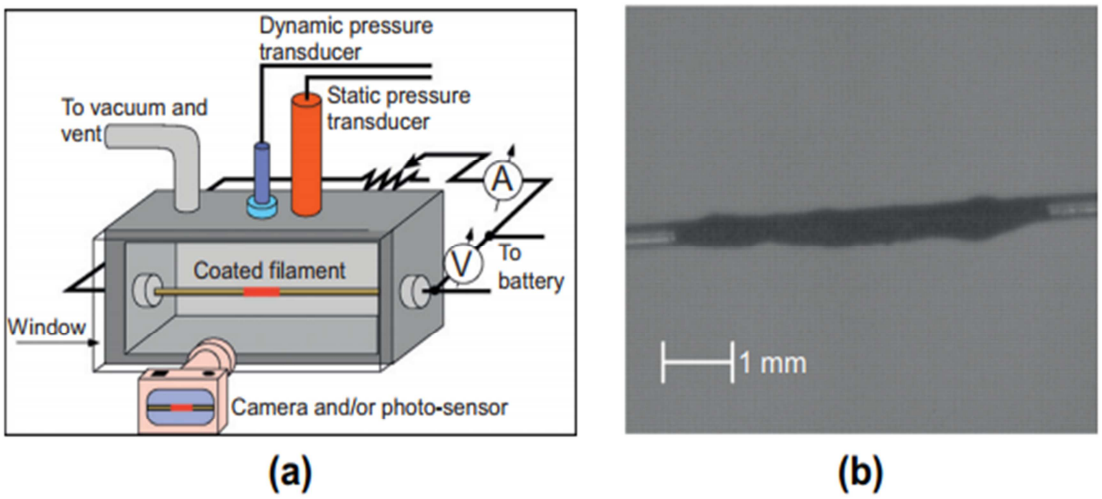

Figure 1.4 (a) Schematic layout of the heated filament ignition apparatus and (b) A close-up image of the Ni-Cr coated with 2Al·3CuO powder.
Source: [60].

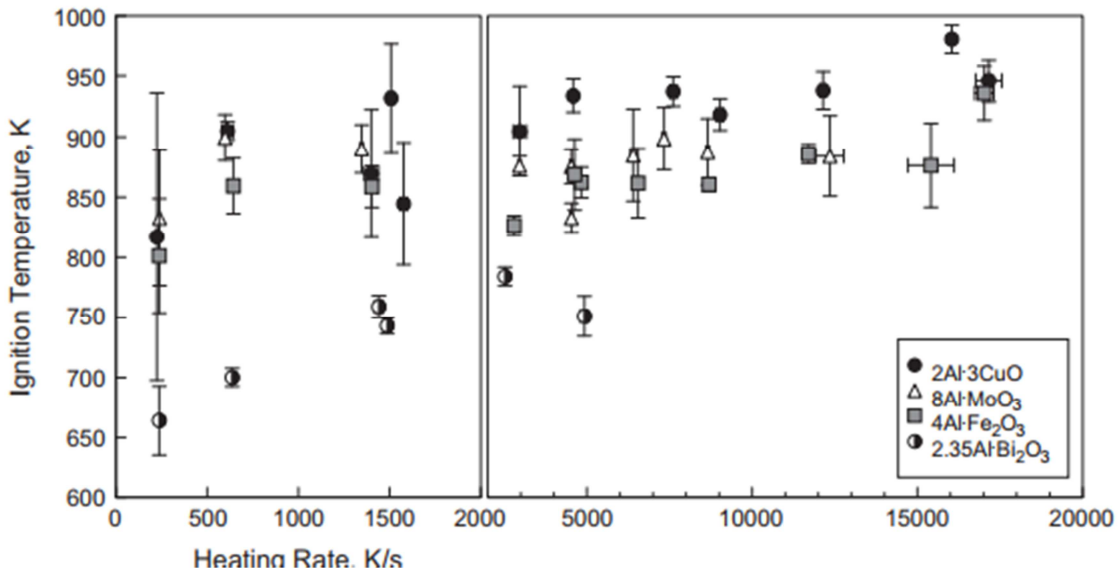

Figure 1.5 Ignition temperatures as a function of the heating rate.
Source: [60].

This earlier work combined both the thermal analysis from the DSC/TG (identifying the early reactions leading to ignition) and the experimental combustion work to propose a model for thermal ignition of thermites. Two models were developed,

one for 2Al-3CuO [65] and the other for 8Al-MoO_3 [61]. Both models utilized the same basic principles behind nanocomposite ignition. While the amorphous alumina layer surrounding the oxidizer inclusion is very thin, the reaction is accelerated by Cabrera-Mott (CM) potential [66, 67]. This mechanism results in a rapid growth of the amorphous alumina layer even at relatively low temperatures (Figure 1.6a). As the amorphous layer gets thicker, CM potential decreases and the reaction becomes rate limited by the conventional thermally activated diffusion. Eventually the amorphous layer begins to change into γ -Al_2O_3. When the overall oxide thickness is smaller than the size of a single γ -Al_2O_3 crystallite (several nm), the polymorphic phase transition causes disruption in the continuity of the alumina layer. Thus, the grain boundary diffusion is enabled so that the oxidation accelerates again (Figure 1.6b). Finally the gamma alumina becomes continuous, when it reaches a certain thickness so that a polycrystalline oxide layer is formed, and the reaction rate is reduced (Figure1.6c) [65]. The model, however, was only built to describe the initial ignition kinetics of the particle; it was assumed that the morphology described in the model is completely destroyed soon after aluminum melts. However, some of the most recent experiments described in this dissertation suggest that the nanostructure might be preserved in some combustion scenarios, so that further research is needed to explore this reaction pathway and possibly extend the model to describe higher temperatures, characteristic of the particle combustion. Additionally the model only considers relatively low heating rates, while it is greater heating rates that seem to change the ignition and combustion mechanisms as seen in the ESD experiments [50]. The previous work also fails to address what happens to the nanocomposite thermites during the combustion process. It was seen in mixed powders that rapid

reactive sintering of particles occurs causing those particles to “forget” their initial nano-structure [68]. There remains a need to further understand these nanocomposite thermites if a fully mechanistic model is to be developed to correlate ignition characteristics and combustion properties with the structure and composition of the nano-composite thermite particles.

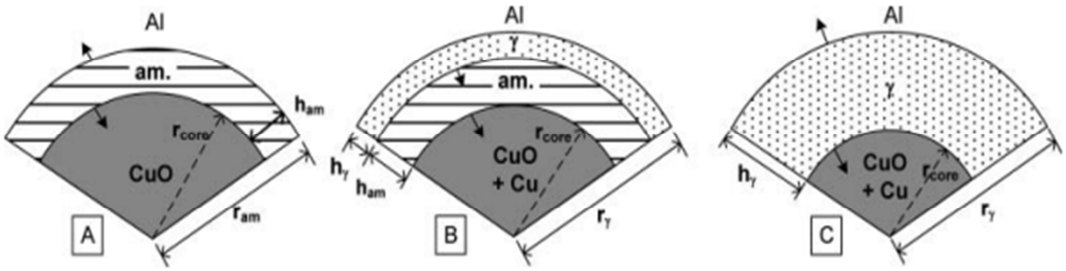

Figure 1.6 Configurations of CuO core and Al_2O_3 shells for different reaction progress. *Source: [65].*

1.4 Objectives

This research is aimed at continuing to build upon the understanding of the mechanisms behind the reaction of the fully-dense nanocomposite thermites prepared by ARM; specifically looking at the ignition delays for different ignition stimuli, e.g., with various heating rates, and at the burn rates, as affected by composition, ignition process, and environment. Experimentally, optical emission from burning thermite particles and powder clouds is captured and interpreted. Quenched samples are also collected and characterized. The effect of material composition, including types of fuel and oxidizer, is addressed in particular. The range of compositions is substantially extended to include fuels other than aluminum and oxidizers other than common metal oxides. Understanding these effects and underlying reactions governing thermite combustion would allow for

greater tunability of newly developed reactive materials. It would also allow one to model combustion of energetic systems involving such nanocomposite thermite additives.

CHAPTER 2

ELECTRO-STATIC DISCHARGE IGNITION OF MONOLAYERS OF NANOCOMPOSITE THERMITE POWDERS PREPARED BY ARRESTED REACTIVE MILLING

2.1 Abstract

Reactive nanocomposite powders with compositions Aluminum Copper (II) Oxide ($2Al{\cdot}3CuO$), Aluminum Bismuth(III) Oxide ($2.35Al{\cdot}Bi_2O_3$), Aluminum Iron(III) Oxide ($2Al{\cdot}Fe_2O_3$), and Aluminum Molybdenum Trioxide ($2Al{\cdot}MoO_3$) were prepared by arrested reactive milling, placed in monolayers on a conductive substrate and ignited by an electro-static discharge (ESD) or spark in air, argon, and vacuum. The ESD was produced by discharging a 2000 pF capacitor charged to a voltage varied from 5 to 20 kV. Emission from ignited particles was monitored using a photomultiplier equipped with an interference filter. Experimental variables included particle sizes, milling time used to prepare composite particles, surrounding environment, and starting ESD voltage. All materials ignited in all environments, producing individual burning particles that were ejected from the substrate. The spark duration varied from 1 to 5 μs; the duration of the produced emission pulse was in the range of 80 – 250 μs for all materials studied. The longest emission duration was observed for the nanocomposite thermite using MoO_3 as an oxidizer. The reaction rates of the ESD-initiated powders were defined primarily by the scale of mixing of and reactive interface area between the fuel and oxidizer in composite materials rather than by the external particle surface or particle dimensions. In vacuum, particles were heated by ESD while remaining on the substrate until they began generating gas combustion products. In air and argon, particles initially pre-heated by

ESD were lifted and accelerated to ca. 100 m/s by the generated shock wave; the airborne particles continued self-heating due to heterogeneous redox reactions.

2.2 Introduction

Electrostatic discharge (ESD) or spark is a well-known and ubiquitous ignition stimulus for energetic and reactive materials [69-72]. However, related ignition mechanisms remain poorly understood. The issue of ESD ignition sensitivity became particularly important for nano-energetic composites [70, 73, 74], including those considered for use in lead-free electric primers [75, 76]. For composite reactive powder mixtures [73] and for pure metals [77-79], it was recently shown that the Joule heating is the primary mechanism of energy transfer from the ESD to the powder. Respectively, the electrical conductivity of the powder was found to affect the ESD ignition sensitivity substantially. It was also reported that different ignition regimes, involving individual burning particles or aerosolized powder clouds, were observed when the thickness of a metal powder layer struck by ESD varied [77]. Most recently, ESD ignition of reactive nanocomposite thermite powders prepared by Arrested Reactive Milling (ARM) [80] was studied [81, 82]. Such powders contain particles with dimensions in the range of 1 – 100 μm, in which metal and oxidizer are mixed on the scale of ca. 100 nm; they are of interest as potential additives to solid propellants [58], reactive structural materials [83], and components of other energetic formulations. It was reported that two distinct spark-initiated ignition regimes were observed for nanocomposite thermites using Al as a fuel and CuO and MoO_3 as oxidizers: monolayers of composite particles ignite within 100-200 ns after the spark discharge onset producing multiple individually burning particles

[82], whereas thicker powder layers ignite following a substantial (~ 0.1-5 ms) delay after the spark discharge and generate burning powder clouds [81]. In addition to vastly different ignition delays, the burn times observed for individual particle and cloud combustion were dramatically different. The burn times for clouds were on the order of several ms, well comparable to the burn times of individual particles of the same thermites ignited by a CO_2 laser beam [54]. However, the particle burn times observed in the monolayer ESD ignition experiments were as short as 100 – 200 μs. It remains unclear what are the causes of different ignition regimes, varied ignition delays, and widely varied burn times, which may be observed for the same nanocomposite powders. Experimental data on ESD ignition of nanocomposite thermite powders remain limited, effects of particle sizes, morphology of the mixed components, surrounding environment, and different material compositions have not been explored systematically. This work is aimed to begin addressing the above deficiencies focusing on ignition of monolayers of different nanocomposite thermites prepared by ARM.

2.3 Materials

Four aluminum-based nanocomposite thermite powders were prepared by ARM. The powders used were as follows: aluminum powder, −325 mesh, 99.5% purity by Atlantic Equipment Engineers; copper(II) oxide powder, 25 μm, 99+ % purity by Sigma Aldrich; bismuth(III) oxide powder, -325 mesh, 99% purity by Alfa Aesar; molybdenum trioxide powder, -325 mesh, 99.95% purity by Alfa Aesar; iron(III) oxide powder, -325 mesh, 99.5% purity by Alfa Aesar. Oxidizers included CuO, Bi_2O_3, MoO_3, and Fe_2O_3. All powders had compositions close to stoichiometric thermites. They were prepared using a

customized Retsch PM400 planetary mill, 3/8" diameter hardened steel balls as milling media, and hexane as a process control agent. Custom-made hardened steel vials were used capable of withstanding a pressure increase that might occur if the material reacts during the milling run. Each vial was loaded with 30 g of powder; the ball to powder mass ratio was 3 and the amount hexane varied from 24 to 48 ml per vial. Milling times are given in Table 2.1. Prepared powders were kept under hexane.

Particle sizes were characterized using a Beckman-Coulter LS230 Enhanced Particle Analyzer. Average particle sizes are listed in Table 2.1. Scanning electron microscope (SEM) images of the nanocomposite powders used in experiments are shown in Figure 2.1. All materials include powders with characteristic shapes and broad size distributions, typical of materials prepared by ball milling. Oxides and aluminum are identified by their coloration and shape. For $2Al{\cdot}Fe_2O_3$, ultrafine particles which could be unattached Fe_2O_3 appear in images in addition to the composite particles. Almost no individual oxide particles are visible for both $2Al{\cdot}3CuO$ and $2.35Al{\cdot}Bi_2O_3$ powders, which are very well mixed. For $2Al{\cdot}MoO_3$, some micron-sized MoO_3 crystallites can be seen along with the composite particles.

Table 2.1 Milling Times and Average Particle Sizes for the Materials used in Experiment

Material Composition (Moles)	**Milling time** (min)	**Average particle size (volume based)** (μm)
$2Al{\cdot}3CuO$	30	16.3
	60	10.6
	80	9.9
$2.35Al{\cdot}Bi_2O_3$	150	10.2
$2Al{\cdot}Fe_2O_3$	60	9.3
$2Al{\cdot}MoO_3$	60	9.4

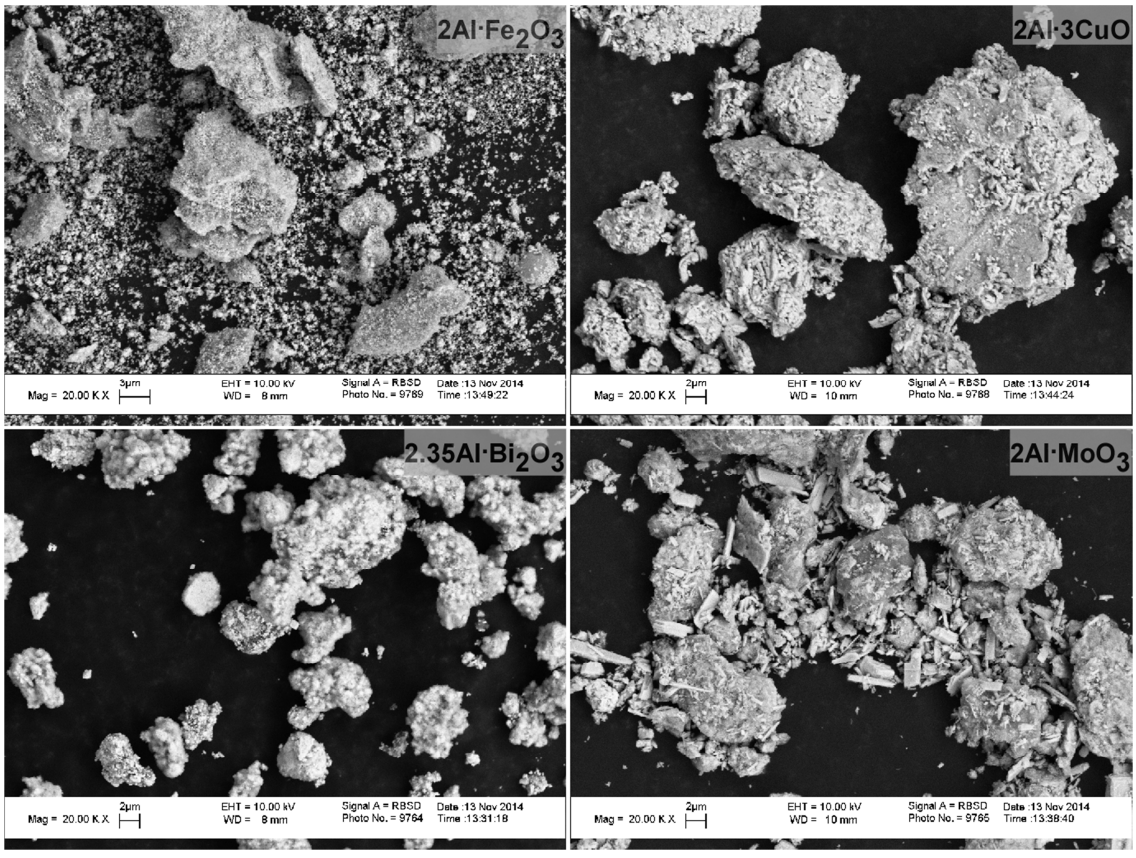

Figure 2.1 SEM images obtained using backscattered electrons and showing nanocomposite thermite powders used in experiments.

2.4 Experimental Details

The ESD ignition apparatus based on model 931 firing test system by Electro-Tech Systems, Inc., was described in detail previously [77, 81]. Briefly, a selected capacitor is charged to a high voltage in the range of 1 – 20 kV. An electronic trigger is activated to enable the capacitor's discharge through a high-voltage pin-electrode to the powder sample. Powder is placed in a holder attached to the second grounded electrode. The high-voltage pin electrode was connected to a positive plate of the capacitor. Both electrodes were mounted inside a sealed test-chamber, enabling the experiments to be performed in different environments. In this study, powder samples were prepared as monolayers adhered to a double-sided carbon tape attached to a brass substrate. The spark gap was maintained close to 1 mm in all experiments. Induction coils by Pearson Electronics were used to monitor the spark current and voltage in real time. Optical emission produced by the ignited samples was recorded using filtered photomultipliers (PMTs). Emission traces as well as the current and voltage traces were recorded using a LeCroy WaveSurfer 64Xs Series oscilloscope. PMTs were used with and without coupled fiber optic cables for different measurements. A Fiber optics cable placed about 5 cm from the sample, was coupled to the PMTs for measurements addressing the effect of particle size and ESD voltage on emission traces. The cable was also used in initial measurements comparing emission produced at different wavelengths to one another. For the measurements addressing the effect of environment and powder milling time, a PMT was placed outside of the experimental chamber about 15 cm from the sample and did not use fiber optics. The former configuration was better suited to distinguish details of radiation originated from the sample surface, while the latter captured better the

emission produced away from the sample. The results were qualitatively consistent between themselves for both configurations; however, specific temporal characteristic between emission traces recorded with and without fiber optics are not compared directly to each other.

Prior to an experiment, a slurry of powder in hexane was prepared; the slurry was applied to a double-sided carbon tape attached to a brass substrate using a small paintbrush. After the slurry dried, compressed air was used to blow off excess powder to achieve a monolayer coating. The prepared sample was placed under the ESD needle in the test-chamber. For experiments in vacuum, the chamber was sealed and evacuated. For experiments in argon, the chamber was evacuated and flushed with argon three times before being refilled to atmospheric pressure with argon. All experiments used a 2000 pF capacitor. A discharge voltage was selected, the capacitor was charged, and the spark was triggered. For each voltage, a blank shot with uncoated carbon tape adhered to the brass substrate was also performed; respective current, voltage, and optical traces were recorded. For each experimental condition, at least five runs were repeated. The standard deviations of the obtained emission and current pulse characteristics are shown as error bars while presenting the results.

2.5 Results

2.5.1 Preliminary Observations

Scanning electron microscope images of the imprints left by ESD produced at different voltages on a powder-coated carbon tape are shown in Figure 2.2. For a 5-kV discharge, a blank spot, from which the powder was removed has dimensions of about 200 – 300

μm. Multiple spots indicating the presence of several discharge channels are observed at increased ESD voltages. Powder outside of the blank spots appears to be undisturbed, although strips of carbon tape are ejected from the areas struck by the spark and land on the unburned powder. The images are shown for only one nanocomposite powder; however, similar spark imprints were observed for all materials.

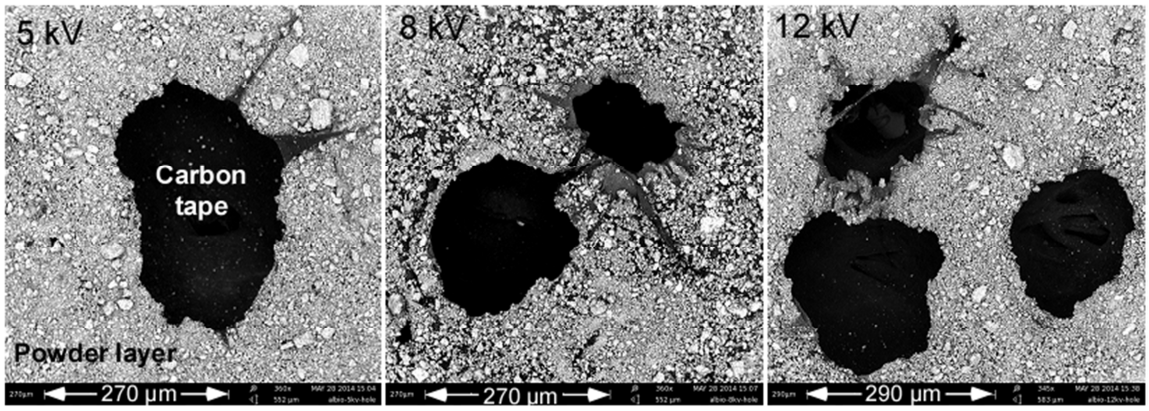

Figure 2.2 Imprints produced by ESD discharges with different voltages on carbon tape coated with $2.35Al{\cdot}3Bi_2O_3$ powder.

Photographs of spark discharges igniting different materials at different spark voltages obtained using a still camera with an open shutter are shown in Figure 2.3. An inset in the top left image illustrates the shape of the sample holder and pin electrode. It also shows the fiber optics cable placed behind the sample. The image in the inset was taken with an external light source, whereas all spark discharges were photographed in the dark. In all discharge images, individual particle streaks are visible originating from the powder coating on the carbon tape. The lengths of particle streaks are greater for the discharges produced at higher voltages. In many streaks, brightness jumps characteristic of metal combustion [84, 85] are observed. Almost all streaks are observed to end before

reaching the walls of the test-chamber. Somewhat surprisingly, the shortest streaks are observed for $2.35Al{\cdot}Bi_2O_3$ material.

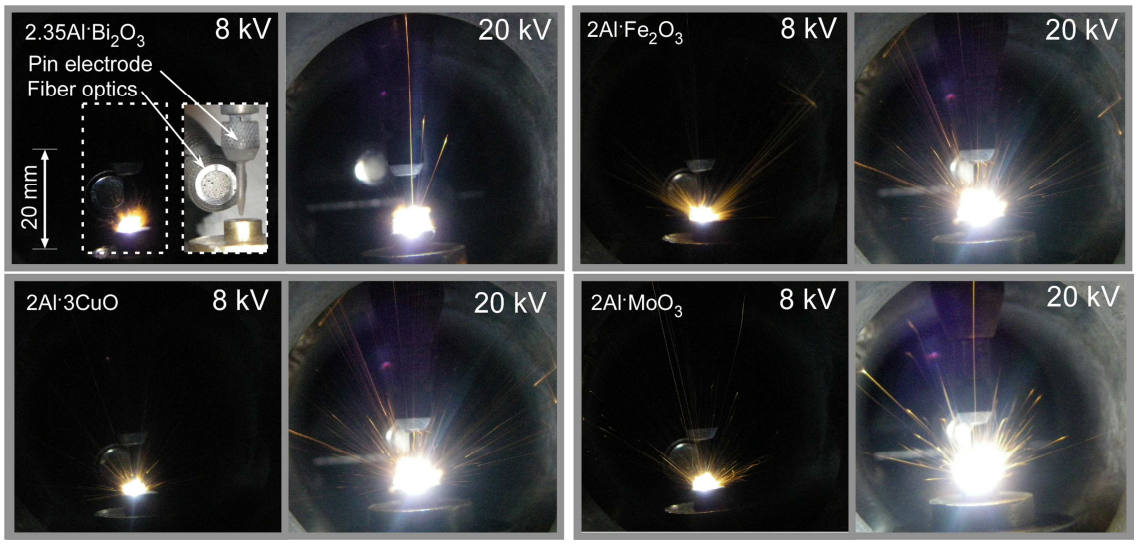

Figure 2.3 Pictures of the four powders being ignited with 8kV and 20kV sparks. An inset in the top left image shows the sample holder/electrode configuration.

Typical recorded traces representing the ESD current, emission produced by the igniting powder, and emission produced by an empty sample holder are shown in Figure 2.4. The initial rise in the emission signal is observed within 100 – 200 ns after the initiation of the ESD, in agreement with [82]. For the example shown in Figure 2.4, the spark duration equal to the duration of the current trace, is about 2 μs. The blank emission signal decays after about 10 μs. The emission signal produced by the ignited powder peaks at about 40 μs and remains above the noise level up to ca. 200 μs. For further processing, the blank signal emission was subtracted from the emission trace obtained with the powder sample, as illustrated in Figure 2.4. For the obtained, blank-corrected trace, a peak onset instant was identified as the inflection point leading to the maximum. In addition, peak position and peak width measured when the signal was at

one half of its maximum value were obtained. Finally, the overall duration of the combustion event or burn time, was identified (not shown in Figure 2.4) as the time when the blank-corrected signal decreased to 10% of its peak value.

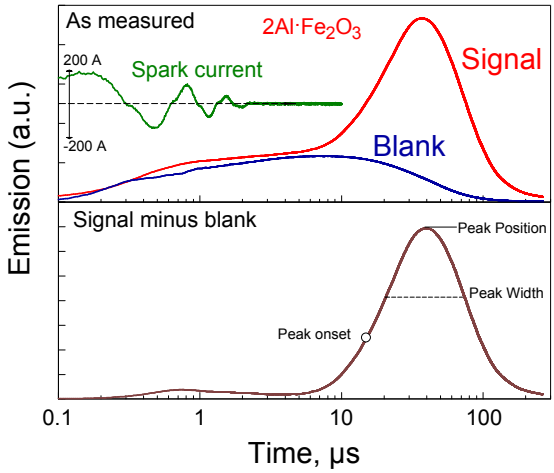

Figure 2.4 Top: experimental current and emission traces with (signal) and without powder on the carbon tape (blank). Capacitor charged to 8 kV. Bottom: experimental emission trace corrected for the blank emission signal.

In preliminary experiments, emission of the igniting samples was monitored using photomultipliers filtered in both infra-red (700 – 900 nm) and visible (486 – 589 nm) ranges. The traces recorded at different wavelengths did not have the same shapes, as illustrated in Figure 2.5, where blank-corrected traces filtered at both 568 and 900 nm are shown for all four tested nanocomposite thermite powders. The 900-nm signals exhibit broad peaks with their maxima located between 2 and 15 µs after the spark initiation. The emission filtered at 568 nm has a small peak at very short times, below 1 µs, followed by a stronger peak occurring at around 20 – 50 µs. The optical emission filtered at 900 nm tracks mostly thermal radiation of the heated particles and combustion products, scaling with the temperature and the available radiating surface. The emission filtered at 568 nm, was selected to not coincide with the AlO molecular emission bands

[86], nonetheless, it could be affected by combustion as indicated by the time-integrated spectra produced by different ignited samples and collected using an EPP2000 High Resolution Spectrometer by StellarNet Inc. The time-integrated spectra are omitted for brevity. Emission signals filtered at 568 nm were used in all of the following data analyses as better indicators of combustion reactions of interest due to less influence by combustion events and temperatures. Despite even possible interference in the optical signals, the trends and comparisons between powders are accurate.

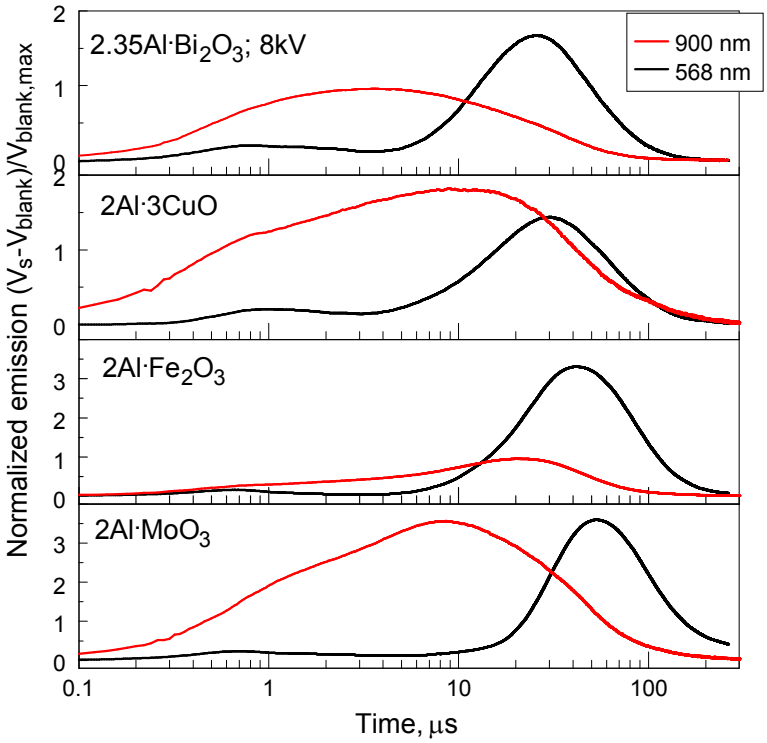

Figure 2.5 Emission traces filtered at 568 and 900 nm produced by igniting monolayers of different nanocomposite thermite powders.

2.5.2 Effect of Particle Size

One of the prepared powders, $2Al{\cdot}Fe_2O_3$, was size classified using a 325 Mesh sieve (opening size of 44 μm). Ignition experiments were then performed with both coarse and fine fractions of the powder. Results are illustrated in Figs. 6 and 7. Somewhat

surprisingly, the streaks produced by the ignited finer particles are longer compared to those generated by the ignited coarse powder fraction (Figure 2.6). The peak onset occurs earlier for the finer particles; however, there is no significant difference between the fine and coarse fractions considering their peak positions, peak widths, and the overall burn times (Figure 2.7).

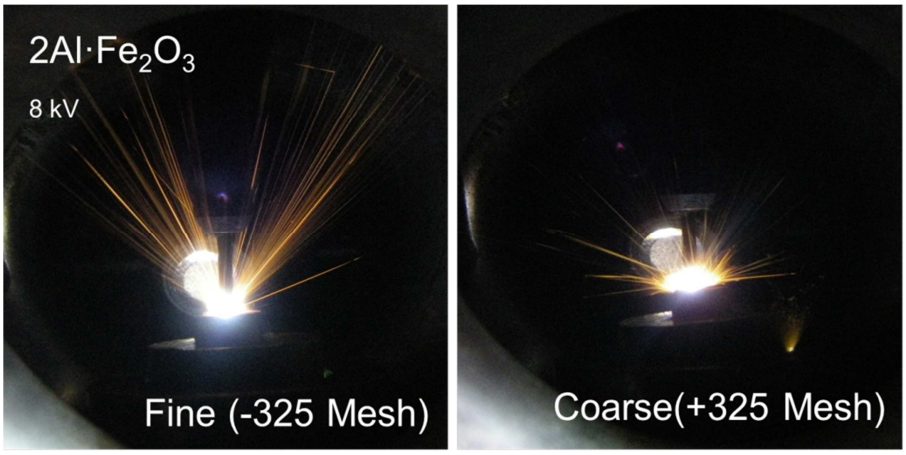

Figure 2.6 Photographs of the ignited fine and coarse fractions of the $2Al{\cdot}Fe_2O_3$ nanocomposite powder taken with a camera with an open shutter.

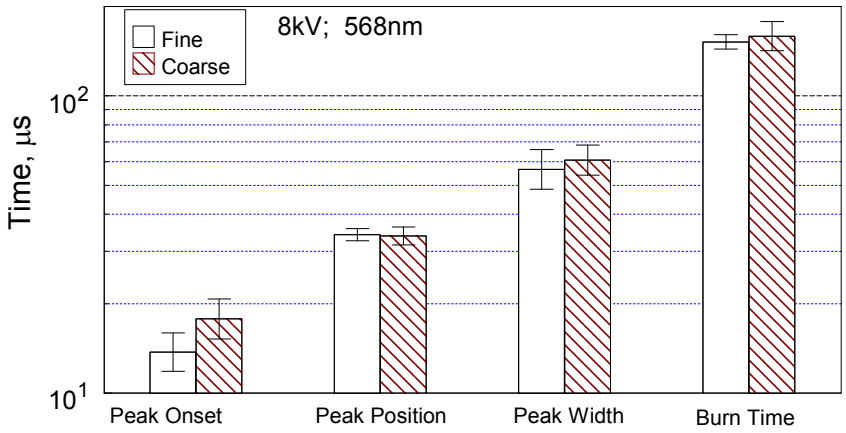

Figure 2.7 Temporal characteristics of the emission signals produced by fine and coarse fractions of the $2Al{\cdot}Fe_2O_3$ nanocomposite powder.

2.5.3 Effect of Milling Time

Powders with nominal composition 2Al·3CuO were prepared with three different milling times: 30, 60, and 80 min. It was shown by [52] that varied milling times result in different numbers of oxide inclusions per unit mass of the composite material, whereas the sizes of oxide inclusions remain nearly unchanged. In other words, at shorter milling times, some of the CuO particles remain unattached to the composite, and the composite is more metal rich compared to the bulk material composition.

As illustrated in Figure 2.8, for the ESD produced at 8 kV, the only difference observed between powders prepared at different milling times is for the peak onset. All other temporal characteristics of the emission signal are effectively identical for different materials. However, at a higher ESD voltage, 20 kV, there is a consistent increase in the peak onset delay, in the peak position, and peak width observed for the powders prepared using longer milling times. The total burn times remain the same for all materials.

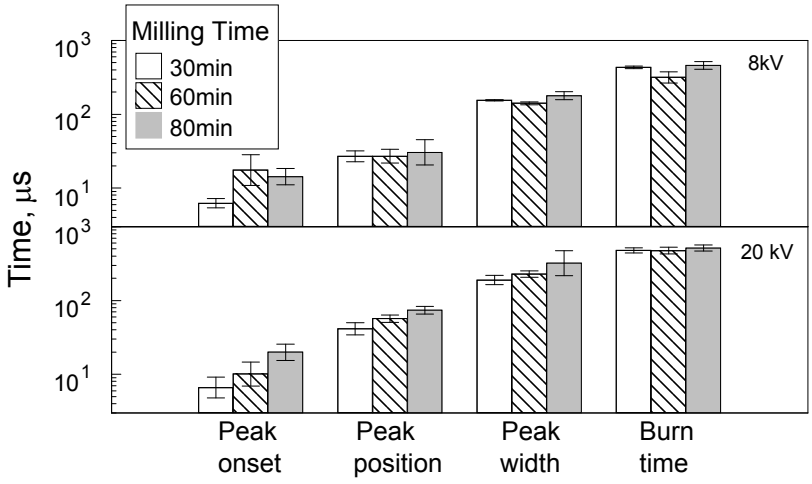

Figure 2.8 Temporal characteristics of the emission signals produced by the 2Al·3CuO nanocomposite powders prepared using different milling times.

2.5.4 Effect of ESD Voltage

When the voltage to which the capacitor was charged was increased from 5 to 20 kV, the spark current pulse duration respectively increased in the range of 1 – 5 μs. Effect of ESD voltage on temporal characteristics of recorded emission traces for different thermites is illustrated in Figure 2.9. For all materials, all characteristic emission times become longer at higher voltages. Comparing different materials to one another, it is apparent that the peak onset is consistently more delayed and peak width is greater for the $2Al{\cdot}MoO_3$ nanocomposite powder compared to other materials. Furthermore, the total burn time for the $2Al{\cdot}MoO_3$ nanocomposite powder is consistently longer than for other powders, for all ESD voltages.

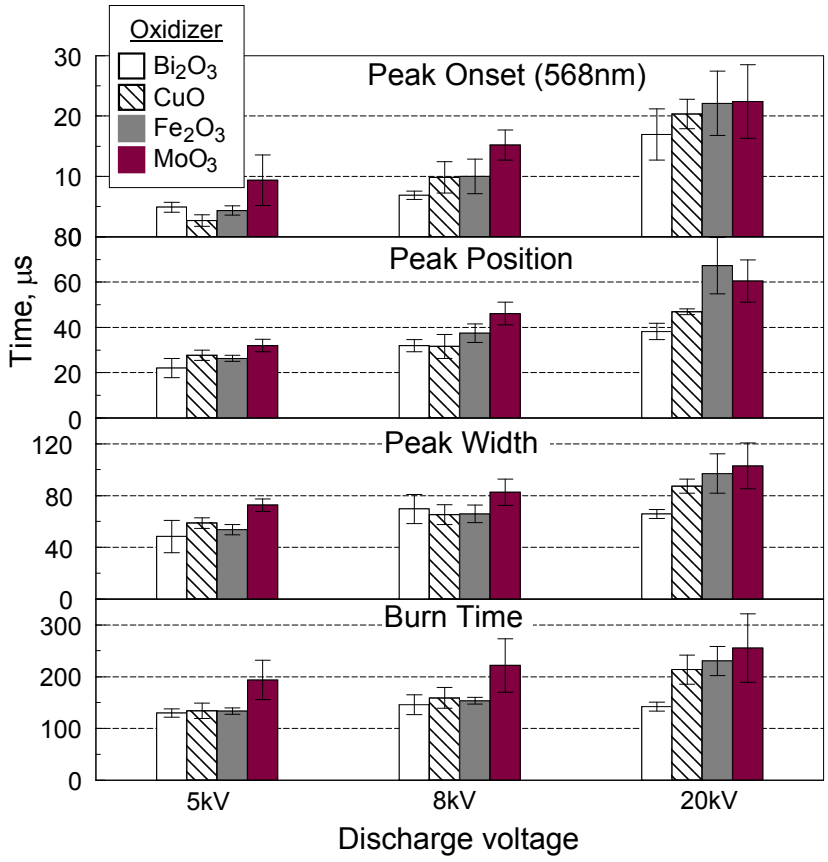

Figure 2.9 Temporal characteristics of the emission signals produced by different nanocomposite powders initiated by ESD at different voltages.

2.5.5 Effect of Environment

Characteristic emission traces recorded for different materials ignited in vacuum, argon, and air are shown in Figure 2.10. Blank signals are subtracted for all traces. For all traces, plotted with a logarithmic time scale, initial oscillatory patterns show interference with the ESD. It appears that the main emission peak observed in argon begins consistently later than the peaks in air and vacuum for all materials. Peak amplitudes vary; for $2Al{\cdot}3CuO$ and $2.35Al{\cdot}Bi_2O_3$, the strongest peaks are observed in argon. For $2Al{\cdot}MoO_3$ and $2Al{\cdot}Fe_2O_3$, the strongest peaks occur in air.

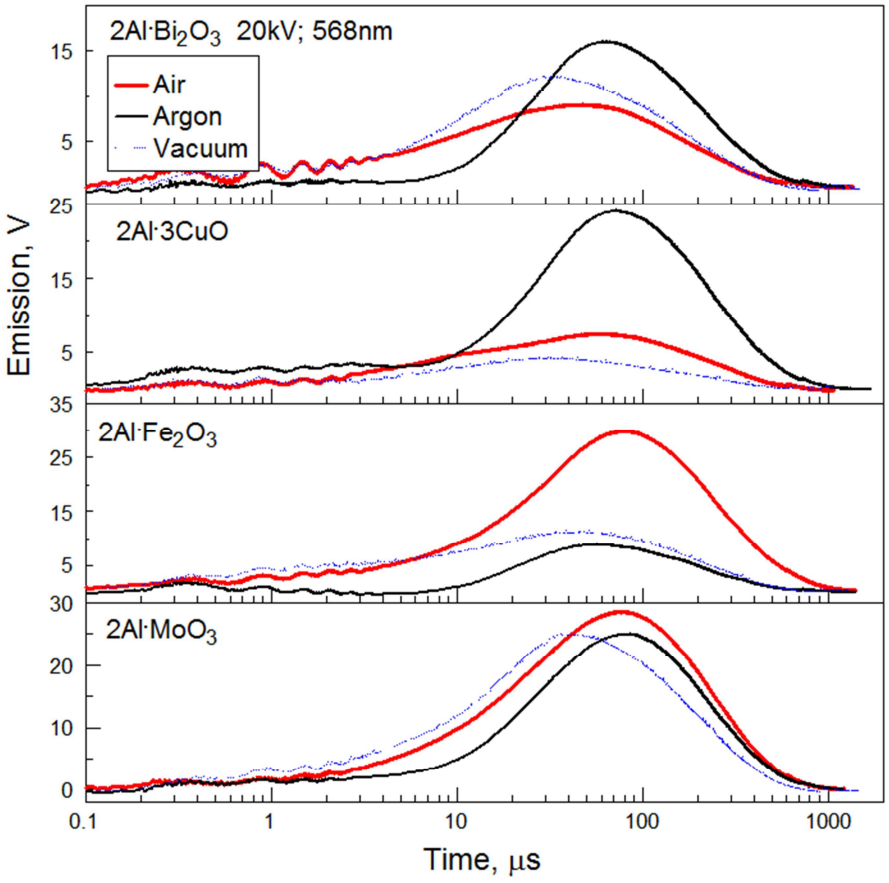

Figure 2.10 Characteristic emission traces recorded for different materials ESD-ignited in different environments.

Results of processing the recorded emission traces are shown in Figure 2.11. Peak onset times are consistently short for vacuum and air, and are much longer for ignition in argon. This is in agreement with the delayed main peak observed in Figure 2.12 for traces recorded in argon.

The shortest times for both the peak width and position are observed for ESD ignition in vacuum for all materials. For the nanocomposite thermites with oxidizers CuO and Bi_2O_3, the peaks are more delayed and wider in argon compared to air. Conversely, for the nanocomposite thermites with oxidizers Fe_2O_3 and MoO_3, the peaks occur at an earlier time and are narrower in argon compared to air.

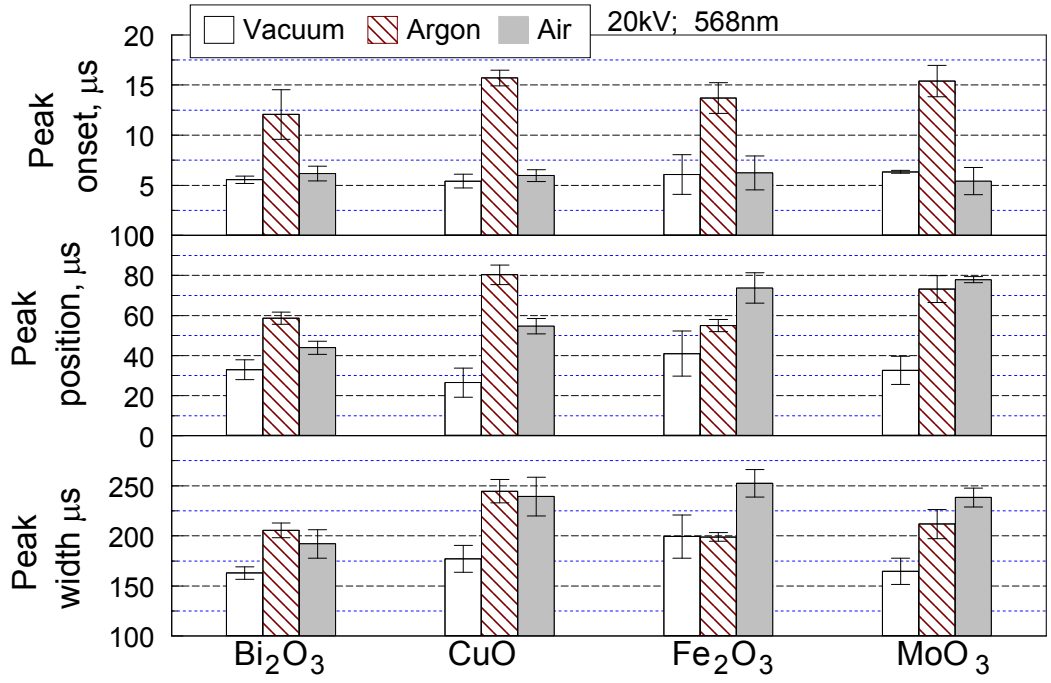

Figure 2.11 Temporal characteristics of the emission signals produced by different nanocomposite powders initiated by ESD in different environments.

ESD current traces were recorded for all environments. Based on the observed decay in the oscillatory current pattern, the equivalent resistance was determined for each material for each environment. Respective blank cases were also processed. The difference between the equivalent resistances of a powder loaded and blank sample holders was assigned to the powder resistance. Using this resistance and an integrated current trace, the total Joule energy transferred to the powder by ESD was evaluated for each material. Details of this processing are available elsewhere [87]. Obtained Joule energies for different materials are shown in Figure 2.12. The greatest Joule energies are observed to be transferred to the powder in vacuum for all materials. For the nanocomposite thermites with oxidizers CuO and Bi_2O_3, the Joule energy transferred to the powder is greater in argon compared to air. Conversely, for the nanocomposite thermites with oxidizers Fe_2O_3 and MoO_3, the Joule energy transferred to the powder is smaller in argon compared to air.

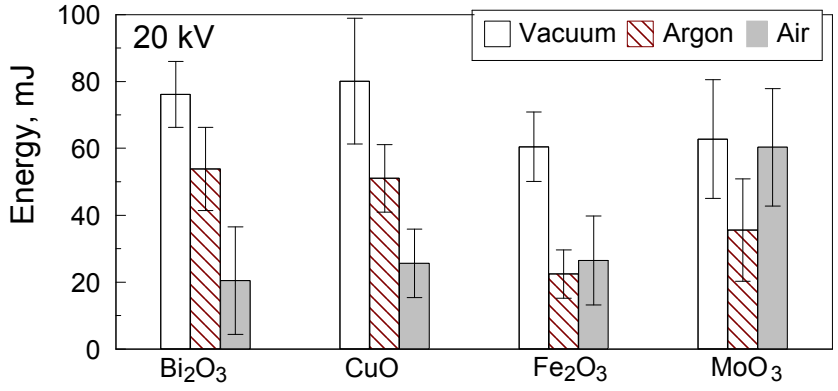

Figure 2.12 Joule energies transferred to powders from ESD in different environments.

2.6 Discussion

An increase in the ESD voltage results in formation of multiple imprints on the substrate, as illustrated in Figure 2.2. This suggests that multiple discharge channels formed between the pin electrode and the powder. The breakdown potential of the spark gap is a function of the gap length, electrode materials, and environment; it does not depend on the initial voltage on the discharging capacitor [88]. Respectively, when the discharge is initiated across the same gap, between the same electrodes, and in the same environment, the breakdown occurs at the same voltage. A higher capacitor voltage causes a greater discharge current and a longer discharge duration. At some voltages, a greater current causes additional channels to form through the discharge gap and through the powder.

An electric spark results in a rapid gas expansion from the discharge kernel, producing a shock wave, which rapidly decays after the current ceases [89]. This rapid gas expansion explains why the spark ignited particles are lifted from the substrate, as shown in Figure 2.2 and why they are rapidly accelerated, as evidenced by their long luminous streaks shown in Figure 2.3. The characteristic size of the spark imprint is 0.3 mm, it is consistent with a sound wave expanding at ~ 340 m/s for approximately 1 μs, a characteristic spark duration time. The velocities of the lifted particles can be roughly evaluated by the length of their luminous streaks and taking into account the overall emission times, measured optically. For ESD at 20 kV, the streak lengths are in the order of 20 mm whereas characteristic emission times are limited by approximately 200 μs for all materials. This yields a particle velocity of about 100 m/s. Considering particle deceleration, this is consistent with particles being lifted by a shock wave generated by the spark.

The above discussion indicates that the particles can only be heated by the spark's Joule energy during a fraction of the total spark duration. As soon as the particles are lifted and removed from the substrate, they are no longer exposed to the ESD current and cannot be heated by its Joule energy. Note, however, that the spark streamers may move along the substrate and heat different particles at different times. Because not all particles are lifted or heated simultaneously, the particles that are lifted and heated later in time, are exposed to a decaying spark current, and thus to a reduced Joule energy, compared to the particles that were heated as soon as the spark commenced.

With the above understanding of the interaction between the spark and the powder, different observations reported here can be consistently interpreted. The effect of particle sizes on the lengths of the produced luminous streaks shown in Figure 2.6 is explained by a greater acceleration caused by the shock wave produced by the spark for smaller particles compared to larger ones. A shorter time leading to the peak onset for smaller particles (Figure 2.7) is also explained by a faster direct heating of smaller particles by the ESD's Joule energy due to their lower per-particle heat capacity.

The lack of difference in the peak position, peak width, and the total burn time between fine and coarse particles can be understood considering that, as suggested earlier [82], the burn time of these nanocomposite particles ignited by the ESD is likely controlled by heterogeneous reactions within the particles rather than reactions involving the external particle surface. In other words, the reaction is initiated before the scale of mixing between aluminum and metal oxide inclusions can be substantially changed, despite aluminum melting. Thus, composite particles continue reacting nearly volumetrically, with reaction products forming inside composite particles, at the

interfaces between metal and oxidizer. This reaction scenario also explains very short total burn times observed in this work and earlier [82] for all nanocomposite materials initiated by ESD.

Schematically, the difference between reactions occurring for slowly and rapidly initiated composite particles is illustrated in Figure 2.13. A starting particle contains an aluminum matrix with embedded nano-scale oxidizer inclusions. When heated slowly, so that the temperature gradients in the heated particle are negligible, an aluminum molten drop is formed that is in contact with agglomerated or coalesced oxidizer inclusions. Aluminum surface tension pools the metal into a single droplet, pushing oxide inclusions together. The area of the reaction interface between aluminum and oxidizer is markedly reduced. The reaction occurs both at the surface of the formed aluminum particle and across the reduced aluminum/oxidizer interface. When the particle is heated rapidly, and when the temperature gradients are significant inside the particle, it is possible that a portion of the particle is molten and even heated above the melting point, while the rest of the particle remains solid. Thus, reaction between aluminum and oxidizer will initiate across initial metal-oxide interfaces existing in the nanocomposite material. Once initiated, the thickness of the product layer (aluminum oxide) at such interfaces would increase, which would stabilize the composite structure and make it more difficult for different oxide inclusions to coalesce or agglomerate. A characteristic time, τ, separating fast and slow cooling can be roughly evaluated as that necessary for the temperature to equilibrate across the particle,

$$\tau = \frac{d^2}{\kappa} \qquad 2.1$$

Where d is characteristic particle dimension, e.g., 10 μm, and κ is the characteristic thermal diffusivity that can be conservatively evaluated taking it as characteristic of pure aluminum, e.g., $9.6 \cdot 10^{-5}$ m^2/s. This estimate yields $\tau \approx 1$ μs; for composite particles, this time would certainly be noticeably longer because of lower thermal diffusivity. Characteristic time of heating for ESD-initiated particles is of the order of 1 μs or shorter; therefore, the heating is fast and the nanostructure existing in the starting material is likely to be preserved.

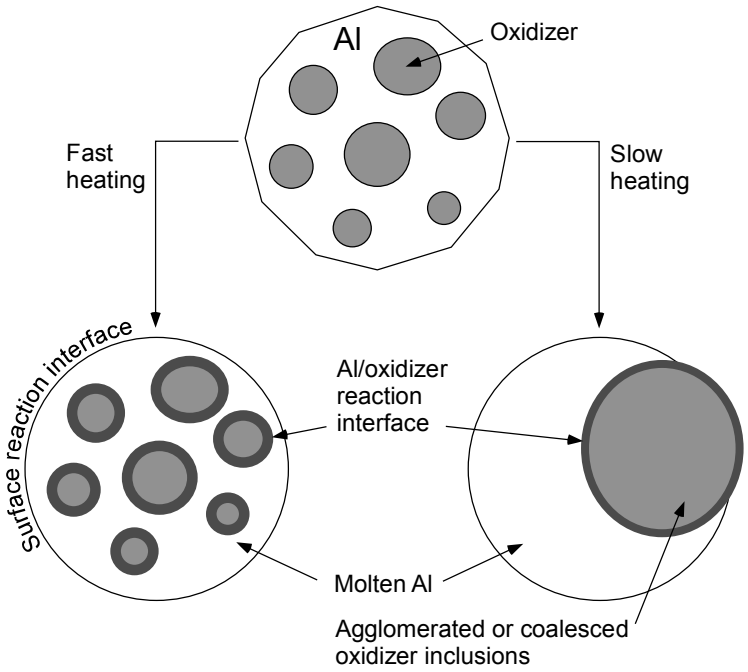

Figure 2.13 Schematic illustration of structures of reacting composite particles initiated at different heating rates.

The effect of milling time on the temporal characteristics of the emission signals produced by the 2Al·3CuO nanocomposite powders shown in Figure 2.8 appears somewhat surprising. The lack of difference in the peak position time, peak width, and

the overall burn time for the particles prepared using different milling times and initiated by a 8-kV ESD suggests that all of the listed characteristic times are controlled by the heterogeneous reaction between CuO inclusions and Al matrix. The dimensions of the CuO inclusions do not depend on the milling time [52], and thus characteristic times of their reactions are also expected to be the same for different composite powders. However, a noticeable increase in all characteristic times is observed for particles prepared with longer milling times when the powder is initiated by a 20-kV ESD. At 20 kV, the discharge pulse lasts longer; respectively, a larger number of particles from the substrate are heated by its Joule energy and lifted by the produced shock wave. The interaction between the discharge and powder is extended in time; however, at longer times, the discharge current diminishes and the Joule energy transferred to the particles becomes smaller. It is thus reasonable to suggest that the particles prepared using shorter milling times and containing a more metal-rich composite may be more difficult to ignite. For such less reactive powders, the ESD-powder interaction leading to generation of ignited particles may cease sooner than for particles milled longer, which will continue igniting even when the ESD current is substantially reduced. As a result, for the powders prepared with shorter milling times, the generation of ignited particles by the spark will stop sooner than that for the powders prepared with longer milling times. This can explain the shift of both emission peak position and peak width to shorter times, as observed in Figure 2.8.

The effect of ESD voltage on the temporal characteristics of powder emission shown in Figure 2.9 can be understood considering that the higher voltage can lift a greater number of particles. Also, at higher voltage particles can be accelerated to a

greater velocity, and larger size particles can be lifted. A delayed ignition is associated with lifting larger size particles; in addition, particles moving faster in a cold environment are cooled more effectively, also leading to an extended ignition delay. The burn times extended at higher ESD voltages can be explained by an increased effect of interaction between burning particles, in the cases when more particles were lifted and ignited by the ESD.

It is also interesting to consider the effect of environment on the observed particle emission traces. Spark discharges produce shock waves in both air and argon; however, no similar shock could have formed in vacuum. Respectively, ESD heated but not yet burning powder particles could have been lifted in air and argon; such lifted particles would then be expected to self-heat due to exothermic redox reactions up to the vapor phase flame combustion temperature. On the other hand, in vacuum the particles were not lifted until they were burning generating volatile combustion products. Thus, particle velocities must be substantially reduced compared to air and argon. Particles would also be expected to be ESD heated to higher temperatures in vacuum because, unlike in air or argon, they remained on the substrate in the absence of a shock wave.

In agreement with the above discussion, all characteristic times for the emission signatures produced by all powders ignited in vacuum in Figure 2.11 are short. The peak onset occurs sooner because the particles remaining on the substrate can be heated longer in the ESD, and reach high temperatures faster compared to particles lifted by the shock in air and argon, and igniting due to their continuing self-heating. Particles that were more significantly pre-heated by remaining on the substrate and lifted due to generation

of the vapor phase products would also be more consumed before being airborne, generating respectively shorter ensuing emission pulses.

Shorter peak onset times observed for the powders ignited in air compared to those in argon can be explained considering that during these times lifted particles self-heat due to redox reaction. In argon, such reactions are limited to those between aluminum and oxide inclusions, whereas in air the particle surface can also react with surrounding oxygen. It is proposed that the additional reaction with air accelerates self-heating. Note that in addition to direct aluminum-oxygen reaction, oxide inclusions exposed to air can be re-oxidized readily while being simultaneously reduced by reaction with aluminum.

Relative values of peak positions and peak widths of the emission pulses generated in air and argon can be correlated with the respective Joule energies of ESD measured in these environments. In both cases, the data show different trends for different materials. For both composites using Bi_2O_3 and CuO as oxidizers, a greater Joule energy is supplied from ESD to the powder in argon than in air. Respectively, both emission peak width and peak position for these materials are greater in argon. Conversely, for the composites with Fe_2O_3 and MoO_3 as oxidizers, the ESD in air generates more Joule energy than in argon (Figure 2.12). Both emission peak width and peak position for these materials are greater in air. It is generally understood that a greater Joule energy causes more particles to ignite, generating respectively longer burn times. The difference in Joule energies transferred to different powders in different environments must be assigned to individual properties of powder particles serving as the discharge electrodes.

Because correlations between observed Joule energies and emission peak characteristics are noted, these correlations are shown graphically in Figure 2.14. The plot shows peak position vs. Joule energy for all materials; a similar plot could have been made for the peak width. It is interesting that two distinct correlations are observed. For vacuum, a greater Joule energy causes shorter times for the emission peak position. This trend is, indeed expected for the particles that are more heated and more consumed directly by the spark while remaining on the substrate, resulting in shorter emission pulses associated with their ensuing vapor phase combustion. An opposite trend, with longer times for the emission peak position for greater Joule energies is observed for both air and argon. At greater Joule energies, it is expected that a stronger shock was generated by ESD, lifting more particles and accelerating them to greater speeds. Respectively, longer emission pulses were produced in these environments.

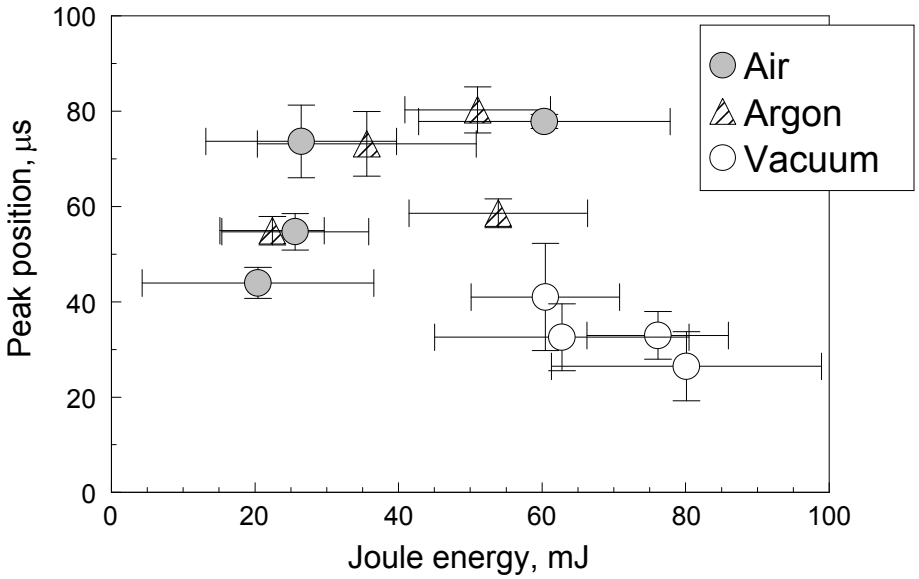

Figure 2.14 Correlation between ESD Joule energy and emission peak position for different environments (each symbol represents a different material, cf. Figs. 12, 13).

Finally, it is discussed whether the present observations correlate with recently quantified kinetics of thermally activated reactions in nanocomposite thermites [52, 65] [61]. Based on thermo-analytical measurements, the models for Al·CuO [60, 65] and for Al·MoO_3 [61] nanocomposite thermites presented the redox reaction as a sequence of individual steps. At low temperatures, the reaction was described by Cabrera Mott mechanism [66], in which the reaction rate decreases with the increase in thickness of the produced layer of product, Al_2O_3. For higher temperatures and thicker oxide layers, polymorphic phase changes in the growing Al_2O_3 are considered, affecting its diffusion resistance. It is interesting whether the models derived based on the very low heating rate measurements can predict a meaningful self-heating of the nanocomposite thermite powders pre-heated by the ESD at very high rates. In order to be meaningful, the self-heating should raise the powder temperature substantially, enabling accelerated redox reaction and formation of vapor-phase reactants expected during combustion of these materials. In addition, the self-heating should occur in the time frame comparable to the experimental peak onset times.

The self-heating anticipated based on the proposed reaction kinetics is estimated here with several simplifying assumptions. It is first assumed that the particles are pre-heated by the ESD instantaneously to a specific initial temperature, so that no redox reaction has occurred during this pre-heating. It is further assumed that only Cabrera-Mott kinetics should be accounted for, considering that the reactions of interest occur with very thin initial oxide layers.

With the assumptions above, it was first established that particles of 2Al·3CuO and 2Al·MoO_3 should be pre-heated to 449 and 540 K, respectively, in order for them to

continue self-heating due to the redox reaction while being exposed to the quiescent room temperature air. This threshold temperature increases when particle motion in air is accounted for. Separate estimates considering the experimental spark energies suggest that such low temperatures can be reached after only 15 – 20 ns exposure of composite particles to the ESD. Particles are expected to be lifted by the shock wave after about 3-30 ns, once they are shifted by a distance comparable to their diameter, 1 – 10 μm, by a shock wave propagating at about 300 m/s. Thus, a very rapid initial heating of composite particles is indeed expected to occur in the ESD, leading to their further self-heating due to heterogeneous exothermic reactions.

The initial self-heating may be very slow from the threshold temperature, although its rate increases when the initial pre-heating temperature becomes higher. As the initial particle temperature becomes greater, the particles were predicted to self-heat faster and reach higher temperatures.

Results of calculations for both $2Al{\cdot}3CuO$ and $2Al{\cdot}MoO_3$ nanocomposite thermites are shown in Figure 2.15. Particles with average sizes shown in Table 2.1 were considered in a room temperature environment. All curves show an increase in the particle temperature due to heterogeneous exothermic reactions followed by cooling, when most of the material is consumed and reaction slows down. Vertical lines show times when peak onset and peak positions are observed experimentally, cf. Figure 2.11. When a $2Al{\cdot}3CuO$ particle is initially heated to about 550 K, it begins to self-heat appreciably only after 100 μs. Such a particle is, therefore, unlikely to ignite. However, if the same particle is pre-heated to about 900 K, it self-heats much faster and may rich about 1200 K after a few microseconds, in time comparable to the experimental delay

until the peak onset. Still greater initial temperatures do not affect the self-heating rate noticeably, while leading to the proportionately greater particle temperatures achieved in a several microseconds. For $2Al{\cdot}MoO_3$ particles, the initial temperatures should be greater in order for the predicted self-heating to become substantial. This is consistent with the observed greater Joule energies that must be transferred to the powder in air prior to its ignition (cf. Figure 2.12). During several microseconds, particles are predicted to self-heat by about 100 K, when their initial temperatures vary from 1000 to 1500 K. This self-heating is relatively weak, implying that additional processes, not accounted for in the reaction model, may assist ignition. Such processes may involve accelerated transport mechanisms of reacting species, Al and O ions, through a very thin Al_2O_3 layer, which can be heated to high temperatures without appreciable increase in its thickness, a situation that cannot be achieved in thermo-analytical experiments.

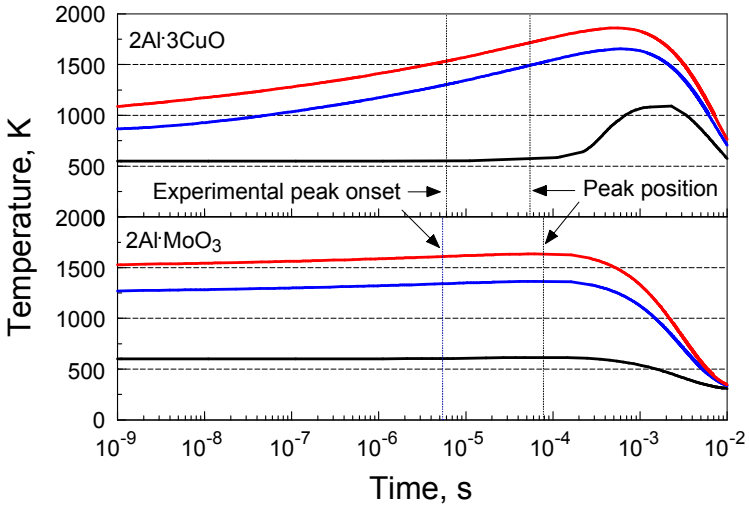

Figure 2.15 Temperatures predicted to be achieved at different times as a result of self-heating of $2Al{\cdot}3CuO$ and $2Al{\cdot}MoO_3$ particles pre-heated by ESD instantaneously to various starting temperatures.

2.7 Conclusions

Reactive nanocomposite $2Al{\cdot}3CuO$, $2.35Al{\cdot}Bi_2O_3$, $2Al{\cdot}Fe_2O_3$, and $2Al{\cdot}MoO_3$ powders prepared by arrested reactive milling placed in monolayers on a conductive substrate are ignited by ESD in air, argon, and vacuum, generating multiple individual burning particles. The onset of the emission pulse produced by the burning particles occurs after the ESD current ceases. The duration of the produced pulse is in the range of 80 – 250 μs for all materials studied. The longest emission duration is observed for the nanocomposite thermite using MoO_3 as an oxidizer. The reaction rates of the ESD-initiated powders are defined primarily by the scale of mixing of and reactive interface area between fuel and oxidizer in the composite materials rather than by the external particle surface or particle dimensions. In vacuum, particles are heated by ESD while remaining on the substrate until they begin generating gas combustion products. In air and argon, particles initially pre-heated by ESD are lifted by the generated shock wave and continue self-heating while being airborne due to heterogeneous redox reactions. Greater ESD voltages result in longer electrical pulses and, respectively, longer lived shock waves. Accordingly, more particles are pre-heated and lifted up at greater ESD voltages in air and argon, producing more delayed and longer emission pulses. The ESD current diminishes in time, so that particles pre-heated and lifted by the end of the current pulse are less likely to ignite. Shock-lifted particles move at very high speeds (~100 m/s), so that cooling by the surrounding gas is substantial. In an oxidizing environment, this cooling is partially offset by an exothermic particle surface reaction with gas. The Joule energy transferred from ESD to powder depends on both the gas environment and the particle compositions; in turn, the Joule energy affects the number of the ignited

particles, their initial velocities, and respective temporal characteristics of the produced emission pulses. During the time comparable to the experimental onset time for the emission peak, kinetic model obtained from thermo-analytical measurements for nanocomposite thermites using MoO_3 and CuO as oxidizers predict appreciable self-heating for the particles assumed to be pre-heated by ESD instantaneously. This self-heating is more substantial for the particles with CuO oxidizer; additional processes not accounted for by the present reaction kinetics may assist ignition for powders with MoO_3.

CHAPTER 3

MODES OF IGNITION OF POWDER LAYERS OF NANOCOMPOSITE THERMITES BY ELECTRO-STATIC DISCHARGE

3.1 Abstract

Nanocomposite powders with aluminum as a fuel and oxides of molybdenum, copper, bismuth and iron as oxidizers were prepared by arrested reactive milling. The powders were placed in 0.5-mm thick layers and ignited by electrostatic discharge (ESD) in air. In different tests, time-resolved light emission was recorded at 568 nm or in the range of 373-641 nm. The amount of material consumed was recorded as well. Time-resolved temperatures were determined. Two distinct ignition regimes were observed. Prompt ignition occurred within 10 μs of the electric discharge, comparable to what had previously been observed for corresponding powder monolayers. This ignition mode was observed for composites with Bi_2O_3 and Fe_2O_3 ignited with a 12 kV discharge, while it only occurred at higher spark voltage (20 kV) and energy for CuO and MoO_3 composites. Delayed ignition, occurring after 0.1-1 ms following the discharge, was observed for all composites with consistently stronger light emission. Analysis of quenched, partially burned particles showed that the original nanostructure was preserved after prompt, but not after delayed ignition. It is proposed that prompt ignition represents direct ESD initiation of composite particles rapidly and adiabatically preheated to high temperatures while keeping the nanostructure intact, resulting in a heterogeneous reaction consuming most of the aluminum. Delayed ignition occurs when particles preheated to lower temperatures start oxidizing at much lower rates leading to cloud combustion, in which

thermal interaction between individual aerosolized burning particles is substantial. During this process the nanostructure may be lost. Temperature measurements show that nanocomposites with CuO and MoO_3 burned superadiabatically with flame temperatures exceeding thermodynamic predictions.

3.2 Introduction

Recent work suggested that two different ignition modes occur for nanocomposite thermite powders ignited by electrostatic discharge (ESD) [50]. Monolayers of powders ignited instantaneously as reported in detail in Ref. [90]. It was also shown that timing of such instantaneous ignition is comparable to that of shock initiation in the same materials [91, 92]. Respective burn times did not exceed 100 – 200 μs. Thicker layers of nanocomposite thermite powders were observed to ignite with certain delays; the burn times were also longer, spanning several ms. These longer burn times were comparable to those observed for individual nanocomposite thermite particles of the same materials ignited by a laser beam [54]. Qualitative differences between the observed ignition modes are interesting and indicative of different combustion mechanisms. Because of a wide range of potential applications for thermite combustion, including pyrotechnic compositions [93, 94], propellants [58, 95], and explosives [96-98], understanding related combustion mechanisms would enable one to tune and control the burn rate and other parameters, such as flame temperature of the respective energetic materials.

The objectives of this study are twofold. First, it is desired to expand the range of available experimental data describing ignition of reactive nanocomposite thermite powders by ESD. These data are useful for better understanding of the ESD ignition

mechanisms. In particular, it is of interest whether a recently developed model of ESD ignition of metal powders [79] is applicable for describing ignition of nanothermites. Second, it is of interest to understand why the same nanocomposite thermites can burn differently depending on the mode of their initiation. Mechanisms of combustion of nanocomposite thermites are poorly understood; better experimental characterization aimed to understand such mechanisms would enable one to design energetic systems and devices using novel nanocomposite thermites with broadly variable and tunable performance.

3.3 Materials

Following our recent work [90], four aluminum-based nanocomposite thermite powders were prepared by Arrested-Reactive Milling (ARM) ($2.35Al{\cdot}Bi_2O_3$, $2Al{\cdot}Fe_2O_3$, $2Al{\cdot}3CuO$ and $2Al{\cdot}MoO_3$). The starting powders used were: aluminum -325 mesh, 99.5% purity by Atlantic Equipment Engineers; copper(II) oxide, 25 μm, 99+% purity by Sigma Aldrich; bismuth(III) oxide, -325 mesh, 99% purity by Skylighter; molybdenum trioxide, -325 mesh, 99.95% purity by Alfa Aesar; and iron(III) oxide, -325 mesh, 99.5% purity by Alfa Aesar. All prepared composite powders had compositions close to stoichiometric thermites: $2Al{\cdot}3CuO$, $2.35Al{\cdot}Bi_2O_3$, $2Al{\cdot}Fe_2O_3$, and $2Al{\cdot}MoO_3$. They were prepared using a customized Retsch PM400 planetary mill, 9.525 mm (3/8")-diameter hardened steel balls as milling media, and hexane as a process control agent. The custom-made hardened steel vials used were capable of withstanding a pressure increase that might occur if the material reacts during the milling. Each vial was loaded with 30 g of powder; the ball to powder mass ratio was 3 and the amount of hexane varied from 24 to 48 ml

per vial. The milling times are shown in Table 3.1. Prepared powders were kept under hexane. The storage time varied from several months to 2 years; no change was observed by differential scanning calorimetry for the powders stored under hexane. Particle sizes were characterized using a Beckman-Coulter LS230 Enhanced Particle Analyzer. Average particle sizes are listed in Table 3.1. The size distributions are consistent with previously published results [50],[90]. All powders have broad size distributions and characteristic shapes typical of materials prepared by ball milling. Electron microscopy images of the prepared powders were presented elsewhere, showing characteristic produced structures of aluminum matrix with nano-sized oxide inclusions [48, 51].

Table 3.1 Average Particle Sizes and Milling Times for the Composites used in the Experiments

Material Composition (Moles)	**Milling Time** (min)	**Average Particle Size (volume based)** (μm) Standard Deviation in parentheses
2Al·3CuO	60	10.6 (7.9)
2.35Al·Bi_2O_3	150	10.2 (7.9)
2Al·Fe_2O_3	60	9.3 (9.1)
2Al·MoO_3	60	9.3 (8.3)

3.4 Experimental Details

The ignition device used was a 931 model firing test system from Electro-Tech Systems, Inc. ESD apparatus. A capacitor was charged to a voltage between 1 and 20 kV. The capacitor was then discharged through a high-voltage pin-electrode placed about 1 mm above the powder sample. The pin-electrode was connected to the positive plate of the capacitor. The negative plate of the capacitor was grounded. The powder was placed in a 0.5-mm deep, 6.7-mm diameter cylindrical cavity in a brass plate serving as a grounded

sample holder. Powder filled the cavity completely; a razor blade was used to remove excess material from the holder and obtain a flat top surface for the loaded powder. Using this sample holder ensured a powder layer thickness of 0.5 mm for all experiments. The discharge was triggered electronically. A 2,000 pF capacitor was used in most experiments. In selected experiments, 10,000 pF capacitors were used as specified below.

This setup was described in further detail elsewhere [50, 77]. For particle collection, an aluminum foil cleaned with acetone was placed 18 – 22 mm away from the sample holder. The aluminum foil was mounted on scanning electron microscopy (SEM) stubs with double-adhesive carbon tape in order to not unnecessarily disturb the particles after collection. The electrode, sample holder, and the ESD chamber walls were also cleaned using acetone before and after every use to ensure no contamination between samples. The brass sample holder was weighed before and after each experiment using an Acculab ALC-80.4 balance. Thus, the portion of the powder consumed during the ignition test was quantified.

Two types of photo sensors were used. A set of measurements relied on a single Hamamatsu E849-34 photomultiplier tube (PMT) equipped with an interference filter centered at 568 nm. The PMT output was connected to a LeCroy WaveSurfer 64Xs Series oscilloscope. The signal was acquired with a time step of 0.1 μs. For other measurements, a 32-channel H7260 series linear array multianode PMT assembly by Hamamatsu was used. The PMT assembly was combined with a spectrometer; the wavelength range covered was 373.4 – 641.0 nm. The signal output from each anode was sent to a separate channel of a 32-channel data acquisition system combining four NI

PCI-6133 DAQ-boards by National Instruments. The data acquisition system was coupled to a virtual instrument custom-designed using LabView 8.5 software. The 32-signal sets were acquired with a time step of 5 μs, limited by the DAQ board speed. Data processing was performed in MATLAB using a custom-designed code.

For temperature measurements, spectra recorded for each acquired time step were matched with Planck's law treating temperature as an adjustable variable. The emissivity, ε, was assumed to be constant, implying a gray body emission. A wavelength-depending emissivity, e.g., following a $\varepsilon \sim \lambda^{-2.94}$ trend [99] was tried; however, the goodness of fit for the respective Planck's curves (see below for details) was substantially reduced; thus the gray body assumption was maintained. Before the measurements the output of the 32-channel spectrometer was calibrated. For calibration, emission spectra produced by a tungsten filament lamp were recorded and compared to those obtained using a StellarNet EPP-2000 spectrometer. A calibration function adjusting output of each channel was generated and applied for all subsequent measurements. Calibration was performed for the range of temperatures 1500-2800 K.

An example of recorded emission signals and respective spectra matched with different Planck's curves is shown in Figure 3.1. It is apparent that the Planck's curve is shifting for different times, indicating a change in the inferred gray body temperature. Goodness of fit of the measured spectra with the Planck's curve was evaluated using the coefficient of multiple determination, or R^2 calculated in MATLAB. The R^2 values became greater than 0.9 at the emission peaks for all spectra. The values of R^2 ranged between 0.9 and 1.0 while the emission signals decayed from their peak values. R^2

smaller than 0.9 but greater than 0.8 were noted at earlier times, in particular, when very high temperatures were implied by the Planck's curves.

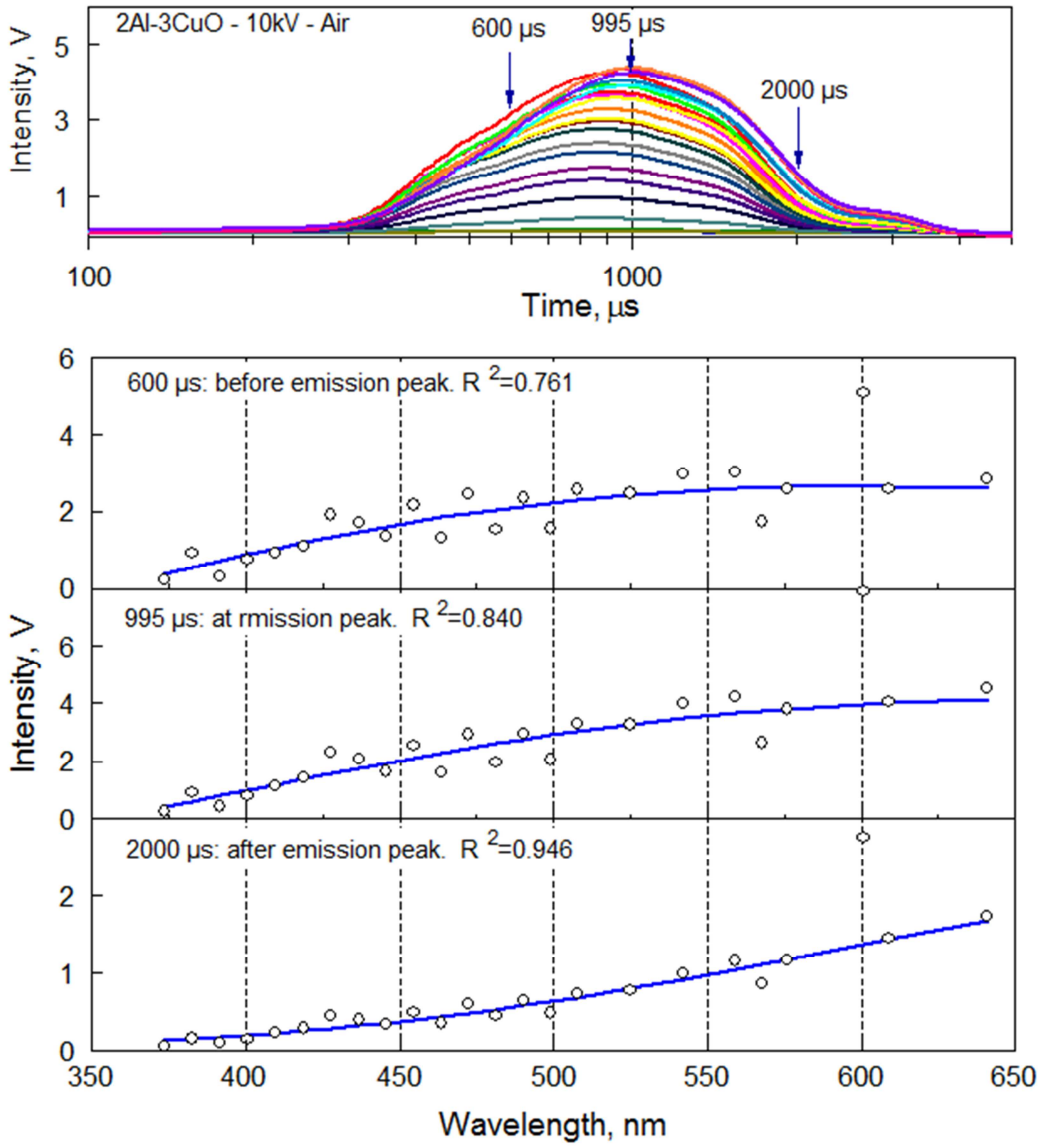

Figure 3.1 Emission traces obtained using the 32-channel PMT/spectrometer assembly and spectra recovered at three characteristic times along with respective Planck's blackbody fits. The signal is recorded for the ESD-ignited 2Al·3CuO nanocomposite thermite.

3.5 Results

3.5.1 Ignition Modes

Emission traces recorded by a single PMT filtered at 568 nm are shown in Figure 3.2. Note that the signals produced by the spark without a powder load are much weaker than those shown and decay well before 10 μs. Two distinct ignition modes for the nanothermites were observed; they will be referred to as prompt and delayed ignition. Prompt ignition resulted in an optical emission with an onset of less than 10 μs, immediately after the electric spark. The onset was defined as the leading inflection point. This timing was comparable to that observed in experiments where the same thermite powders were ESD-ignited as monolayers [90]. Prompt ignition was observed for $2Al{\cdot}Fe_2O_3$ and $2.35Al{\cdot}Bi_2O_3$ powders at 12 kV, but for $2Al{\cdot}3CuO$ and $2Al{\cdot}MoO_3$ only at 20 kV and using a 10,000 pF capacitor. Delayed ignition caused an emission peak around 1 ms or later. Delayed ignition was observed for all powders. Powders with CuO and MoO_3 serving as oxidizers showed only delayed ignition at lower ignition voltages.

Ignition was generally accompanied by sound. At 12 kV and 2,000 pF, the sound produced by the ignited powder was substantially stronger when only delayed ignition occurred (oxidizers CuO and MoO_3) compared to cases of prompt ignition (oxidizers Bi_2O_3 and Fe_2O_3).

Figure 3.2 illustrates differences in signals produced by experiments, in which prompt ignition was or was not observed. For $2Al{\cdot}Fe_2O_3$ and $2.35Al{\cdot}Bi_2O_3$ powders, the prompt ignition peak originated during the ESD discharge pulse. The discharge pulse has a duration in the range of 0.5 – 5 μs, depending on the voltage. For $2Al{\cdot}3CuO$ and $2Al{\cdot}MoO_3$, ignited at 10 and 12 kV, respectively, emission was only detected more than

100 μs after the end of the ESD discharge. Emission signals are normalized in Figure 3.2, so it is not apparent that the overall intensities of the emission signals produced by delayed peaks for $2Al{\cdot}3CuO$ and $2Al{\cdot}MoO_3$ were much greater than those for $2Al{\cdot}Fe_2O_3$ and $2.35Al{\cdot}Bi_2O_3$.

When the ESD voltage was increased to 20 kV and the capacitor used was 10,000 pF, emission signal for the ignited $2Al{\cdot}3CuO$ and $2Al{\cdot}MoO_3$ originated immediately after the spark, indicating prompt ignition. The delayed ignition still occurred in those experiments following the prompt ignition, as illustrated in Figure 3.2, where large secondary peaks are observed for the signals describing experiments with 20-kV discharges. Respective traces shown in Figure 3.2 were acquired with a reduced voltage applied to the PMT, to accommodate a much stronger overall light intensity.

For $2Al{\cdot}Fe_2O_3$, emission traces always included two overlapped peaks. To determine the characteristics for prompt and delayed ignition separately, the signal was curve-fitted with two separate peaks. Free software, Fityk, was used for the curve fitting; it was found that two log-normal peaks can describe the experimental traces relatively well, as illustrated in Figure 3.2.

For $2.35Al{\cdot}Bi_2O_3$, only the prompt ignition peak was observed in most experiments. In some cases, however, a second, well delayed emission peak was observed. When the delayed peak was observed, it was noted that the entire powder load was ejected from the brass holder resulting in the formation of a large burning aerosol cloud. As further discussed below, delayed ignition is attributed to the combustion of aerosolized powder cloud in this and other cases. The example shown in Figure 3.2 includes a portion of such a delayed peak. The shape of the prompt peak did not appear

to change whether or not the delayed emission was observed. Attempts to identify specific conditions for which the delayed peak occurred reproducibly were not successful.

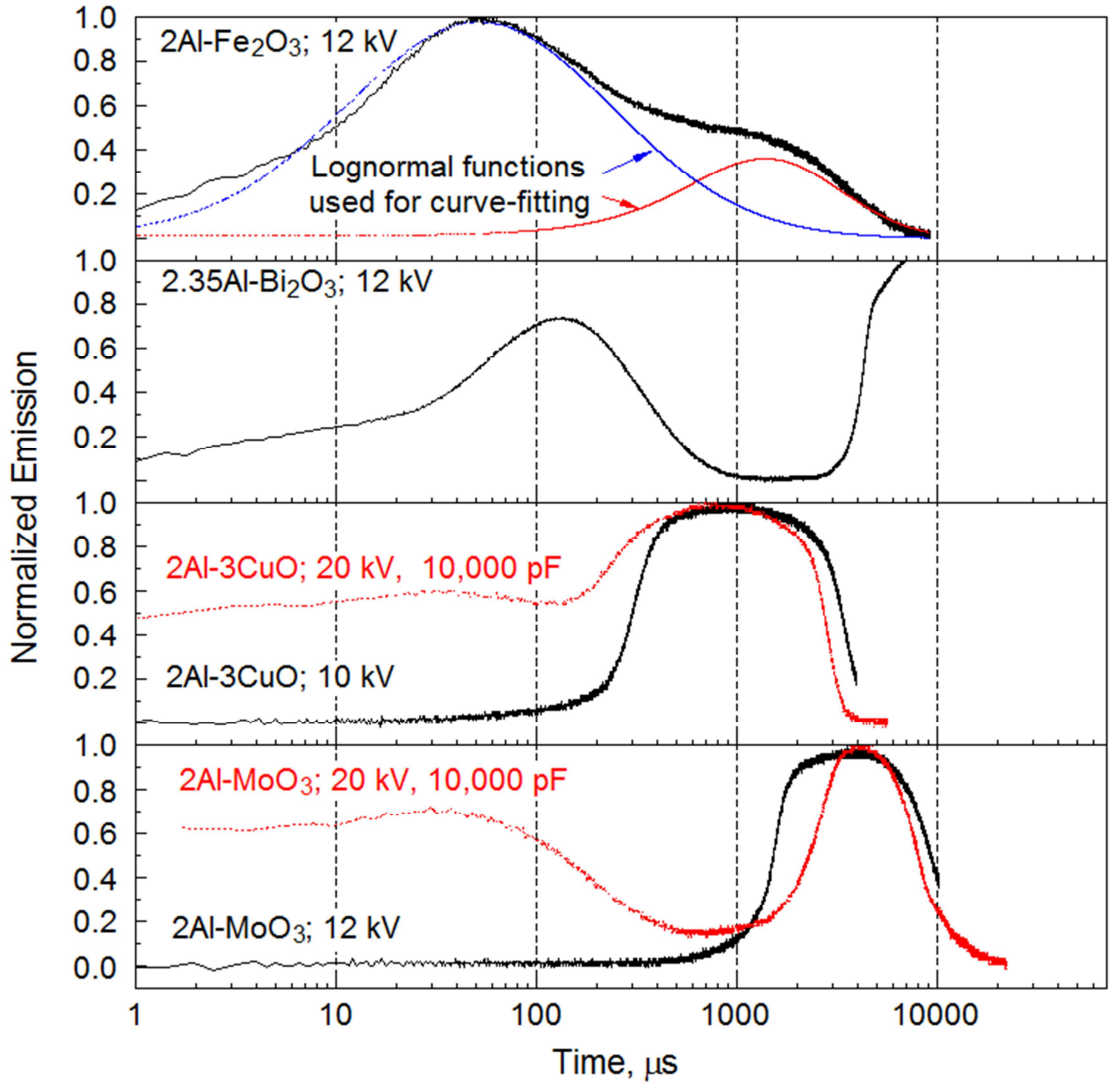

Figure 3.2 Normalized emission traces recorded at 568 nm for different nanocomposite thermite powders ignited by ESD. Sensitivity of the PMT is reduced for the thermites with CuO and MoO_3 as oxidizers to accommodate substantially brighter emission. For $2Al{\cdot}Fe_2O_3$, results of curve-fitting using two lognormal functions are also shown.

In addition to different optical emission signatures, different ignition modes ejected different amounts of powder in a single experiment. In a set of experiments, the

sample holder containing powder was weighed before and after each ignition test. Table 3.2 shows the results of the powder loss measurements. For experiments at a lower voltage and using 2,000 pF capacitor, the powders that did not show a prompt ignition peak lost the most material, with only a small amount of powder remaining in the sample holder. Conversely, powders exhibiting prompt ignition lost less than a third of the available mass; thus most of the material remained in the sample holder after the ESD ignition test.

Table 3.2 Portion of Material Lost after Ignition of the Powders by ESD

Material	Ignition Voltage (kV)	Capacitor (pF)	Runs	Material loaded (mg)	Percentage of Material Lost	Prompt ignition
$2Al{\cdot}Fe_2O_3$	12	2,000	4	12.2 ± 1.5	23.5 ± 10.4	Yes
$2.35Al{\cdot}Bi_2O_3$	12	2,000	4	15.8 ± 1.1	32.6 ± 22.6	Yes
2Al·3CuO	10	2,000	5	17.8 ± 4.6	89.0 ± 1.1	No
$2Al{\cdot}MoO_3$	12	2,000	4	7.8 ± 1.4	81.4 ± 3.9	No
2Al·3CuO	20	10,000	2	14.7 ± 0.1	89.0 ± 6.4	Yes
$2Al{\cdot}MoO_3$	20	10,000	2	14.6 ± 0.1	71.7 ± 3.8	Yes

3.5.2 Prompt Ignition

Traces recorded using a single filtered PMT, such as those shown in Figure 3.2, were used to determine temporal characteristics of the prompt ignition peaks. These characteristics were the same as identified in Ref. [90] for emission signals produced by the ignited monolayers of the same powders. The peak onset was determined as the inflection point leading to the maximum. The peak position was obtained from the signal directly, or from the curve fit in the case of overlapping prompt and delayed emission peaks. The peak width was measured when the signal was at one half of its maximum

value. Finally, the burn time was found as the time from the instant of the spark initiation until the signal decreased to 10% of its peak value.

For $2Al{\cdot}Fe_2O_3$, the temporal characteristics of the prompt ignition were based on the first of the overlapping lognormal peaks obtained as a result of curve fitting. Results are shown in Figure 3.3, where for comparison, similar temporal characteristics are also shown for the ignited powder monolayers [90]. General trends are the same for both $2Al{\cdot}Fe_2O_3$ and $2.35Al{\cdot}Bi_2O_3$ powders. The present data for prompt ignition for 0.5 – mm thick powder layers indicate a faster peak onset compared to the respective monolayers. It is possible that, at least partially, the accelerated onset of reaction is associated with a higher ESD voltage: 12 kV and 10 kV (depending on the thermite, see table 2) for 0.5-mm thick layer vs. 8 kV for monolayer. Conversely, all other characteristic times corresponding to the peak position, width, and duration of the emission signal are somewhat greater for the 0.5-mm thick powder layers.

For $2Al{\cdot}3CuO$ and $2Al{\cdot}MoO_3$ powders, the onset of the prompt ignition peak occurs very rapidly, within a few μs, and is difficult to distinguish from the end of the ESD. The onsets are shifted to somewhat longer times for the 0.5-mm thick powder layers. The peak positions are similar to those observed for respective monolayers, as well as to those of the other materials. As for the other powders, peak widths and duration are greater for 0.5-mm thick powder layers compared to those of monolayers.

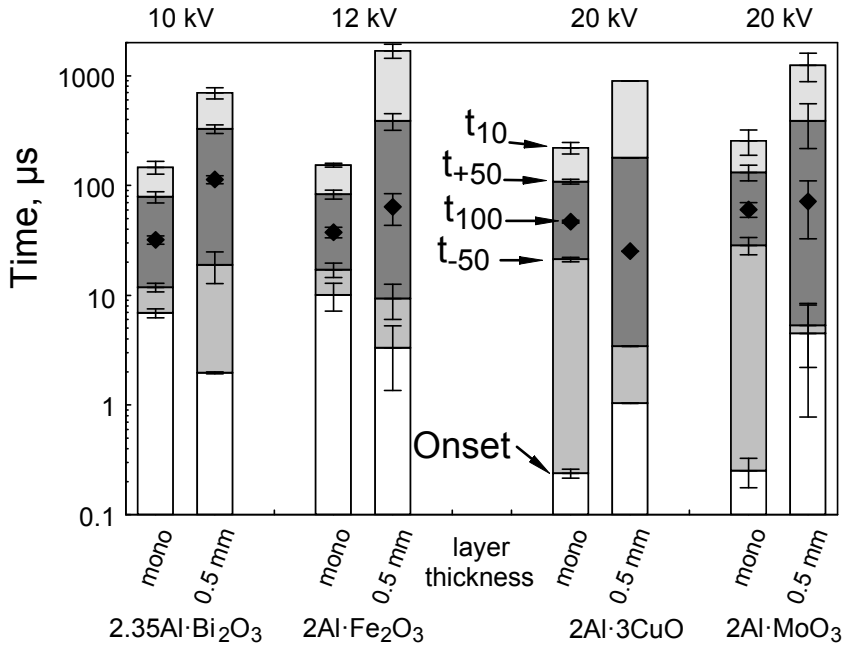

Figure 3.3 Temporal characteristics of prompt combustion peaks for 0.5-mm thick layers of nanocomposite thermites ignited by ESD compared to respective combustion characteristics of the same materials ignited as powder monolayers. ESD voltages are shown on top of the respective bar plots. Labels correspond to the following: t_{-50} and t_{+50} are peak width (front and back); t_{100} is peak position; t_{10} is burn time.
Source: [90].

Signals recorded using the 32-channel PMT/spectrometer assembly were processed to evaluate the temperatures observed for prompt-ignited powders. Unfortunately, limited time resolution restricted useful readings at short times, immediately following ESD. Results are illustrated in Figure 3.4. For $2.35Al{\cdot}Bi_2O_3$, a signal was selected that showed both prompt and delayed ignition peaks. For $2Al{\cdot}Fe_2O_3$ the prompt ignition peak is poorly resolved and the signal is initially saturated.

The Planck's fit for the $2.35Al{\cdot}Bi_2O_3$ emission shows relatively small changes in the temperature around 2500 K during the prompt ignition event; for the delayed ignition, the temperature is slightly higher, reaching 2800 K. For $2Al{\cdot}Fe_2O_3$ the temperatures are obtained only for the delayed ignition. The Planck's fit to the measured emission signals

indicates that the maximum temperature is around 2800 K. In both cases, the goodness of fits was acceptable (R^2>0.9) indicating that the gray body emission was dominant in the measured radiation signals.

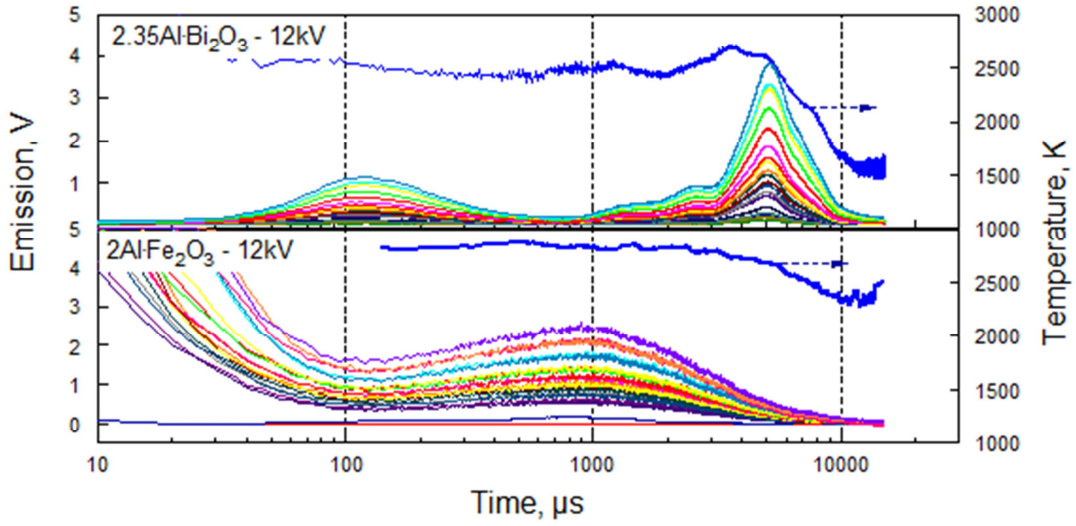

Figure 3.4 Emission traces recorded using the 32-channel multianode PMT/spectrometer assembly for cases of prompt ignition of 2.35Al·Bi_2O_3 and 2Al·Fe_2O_3 nanocomposite thermites. Temperature traces obtained from the recorded spectra are also shown.

Combustion products collected on aluminum foil placed in proximity of the sample holder were examined using an SEM; characteristic images are shown in Figure 3.5. Combustion products of both 2.35Al·Bi_2O_3 and 2Al·Fe_2O_3 contain molten and oxidized particles, which clearly experienced high temperatures, mixed with particles that appear unignited and thus could have remained cold. The latter particles have the same shapes, sizes, and surface morphology as the powders originally prepared by ARM. Some of the molten and oxidized particles, especially for products of 2.35Al·Bi_2O_3, have interesting shapes showing precipitation of a brighter, Bi-rich phase from the melt. No large scale separation between aluminum oxide and bismuth or iron-rich phases was

observed, similar to the products obtained from the powder monolayers [90]. It is also interesting that many molten and unignited particles were observed to be in direct contact with each other. Such contacts could cause ignition of the colder particles and, conversely, quenching of the burning particles.

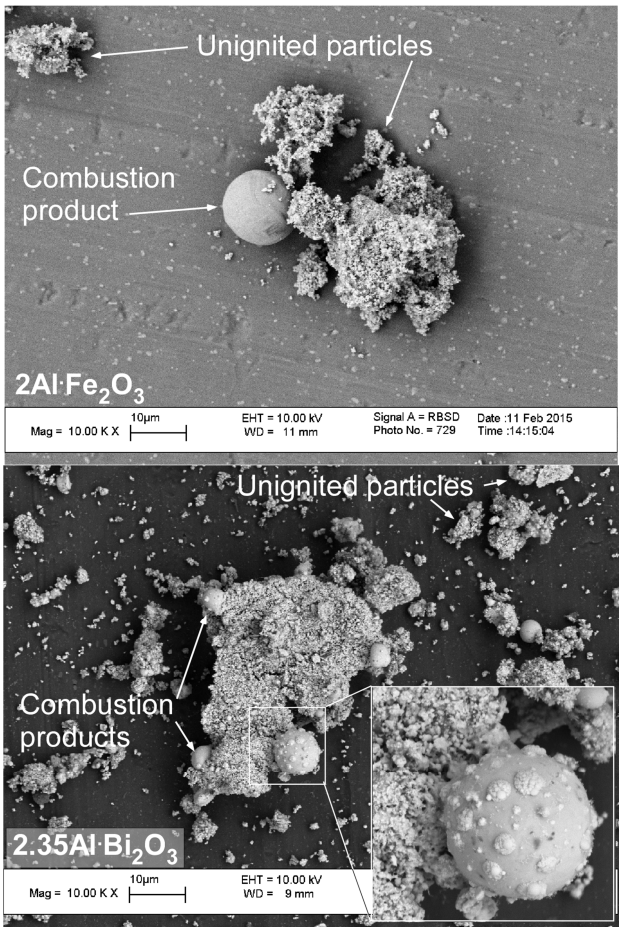

Figure 3.5 SEM images of product particles collected after prompt combustion events.

3.5.3 Delayed Ignition

Characteristic emission traces recorded using a 32-channel multianode PMT/spectrometer assembly are shown in Figure 3.6 for both nanocomposite thermite powders, which exhibited only delayed ignition at reduced ESD voltages. Respective temperatures are

also shown for both materials. The Planck's formula did not fit the experimental spectra well at earlier times, when the emission intensity was increasing (R^2<0.9). The goodness of fits improved substantially for the decaying parts of the emission traces (R^2 approaching 1.0). This suggests that the growing portion of the emission traces was accompanied by substantial vapor phase reaction generating optical emission different from the gray body radiation. Respectively, the temperatures inferred from fitting the recorded spectra by Planck's curve prior to the emission peak may be erroneous. The accuracy of temperature measurements for the decaying portions of the traces is better. Observed temperatures are substantially greater than those shown in Figure 3.4 for promptly ignited powders.

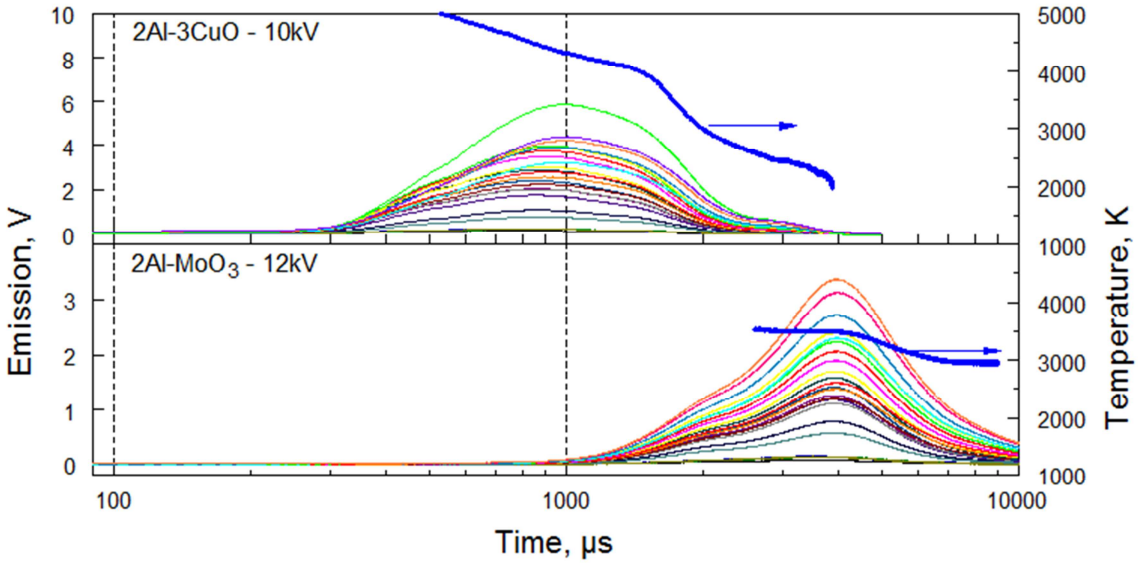

Figure 3.6 Emission traces recorded using the 32-channel multianode PMT/spectrometer assembly for cases of delayed ignition of 2Al·3CuO and 2Al·MoO_3 nanocomposite thermites. Temperature traces obtained from the recorded spectra are also shown.

Average temperatures obtained from such traces as shown in Figures 3.4 and 3.6 are shown in Figure 3.7. Clearly, the powders exhibiting prompt ignition have

substantially lower flame temperatures compared to those, which only show delayed ignition pattern.

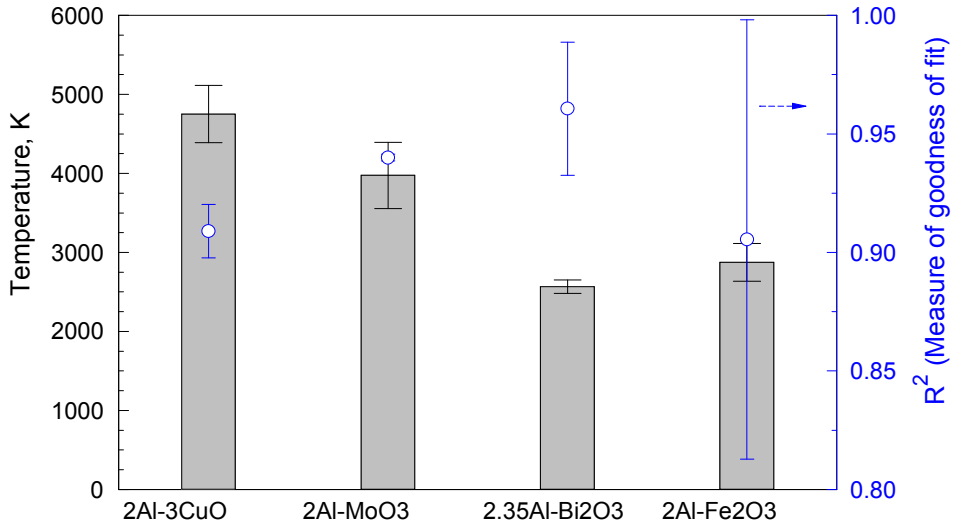

Figure 3.7 Temperatures corresponding to the delayed ignition peak position obtained from the measured emission spectra.

Temporal characteristics of the emission pulses produced by the delayed combustion are shown in Figure 3.8. For all materials, peaks recorded using a single PMT filtered at 568 nm were used for this analysis. For $2Al{\cdot}Fe_2O_3$, the processing used the second peak inferred from the curve-matching (see Figure 3.2). Aside from substantial differences in the peak onset, other characteristics are fairly similar for all materials. The peak position shifts within a few ms. Similarly consistent between materials are the peak width and burn time. Overall, the characteristic times are longest for the nanocomposites with MoO_3 as an oxidizer.

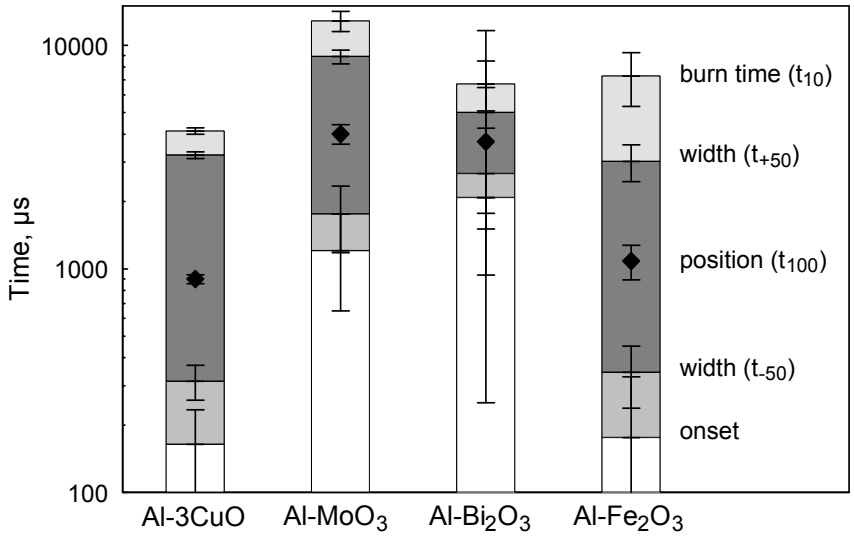

Figure 3.8 Temporal characteristics of the emission signals produced from ESD ignitions.

Combustion products quenched on an aluminum foil placed about 18 mm away from the powder are shown in Figure 3.9 for both materials, for which only delayed ignition peaks were observed at reduced ESD voltages. Unlike combustion products shown in Figure 3.5, almost no unreacted particles are found. Shapes of most particles are indicative of solidification of high-temperature molten droplets. For products of both 2Al·3CuO and 2Al·MoO_3, aluminum oxide is separated from the reduced metal or its oxide. Darker portions of the particles in both left and right images in Figure 3.8 show Al_2O_3, while brighter portions show compositions rich in Cu and Mo, respectively. The scale of separation between phases is substantially greater for these materials compared to the products collected for the powders exhibiting prompt ignition (cf. Figure 3.5). This coarser structure suggests that the nano-scaled structure of the ARM-prepared materials was destroyed upon their ignition. The separation of molten aluminum and oxidizer

inclusions caused longer characteristic reaction times, consistently with the experimental optical emission traces.

For products of 2Al·3CuO, product particles are very close to one another, indicating that agglomeration could have been substantial. Particles are also more deformed from spherical shapes, suggesting that they struck the substrate with relatively high velocities. Conversely, products of $2Al \cdot MoO_3$ are fairly spherical. Their shapes suggest that particles could have solidified before striking the surface. It is also possible that they did not move at appreciable velocities before the impact. It is also noted that particles are further apart from one another.

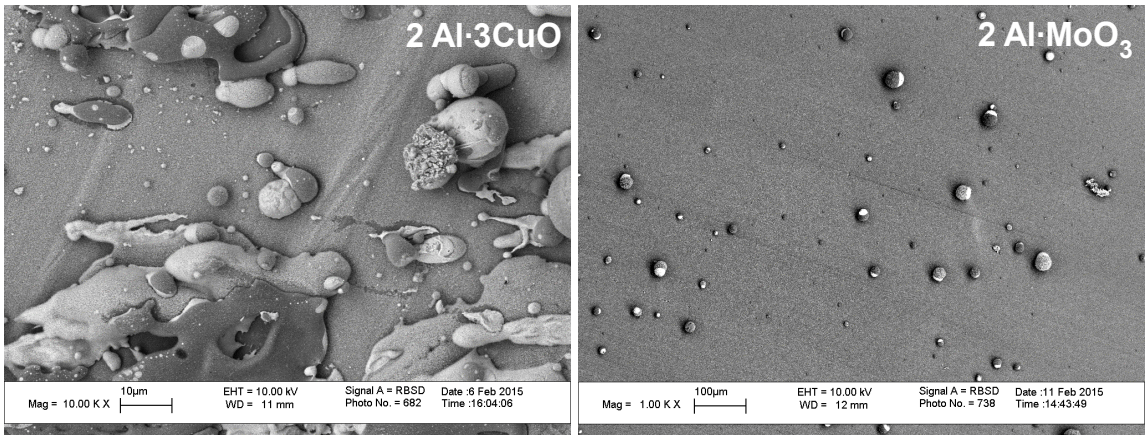

Figure 3.9 SEM images of combustion products for 2Al·3CuO and $2Al \cdot MoO_3$ composite powders, exhibiting only delayed ignition.

3.6 Discussion

3.6.1 Prompt Ignition

Qualitatively, present results agree with recent reports describing different ESD ignition modes observed for nanocomposite thermite powders [50, 90]. The present approach

involving a broader range of materials and extended measurements is helpful in elucidating the material characteristics leading to different ignition modes.

Ignition temperatures measured for the same materials as used in the present work, but placed on an electrically heated filament were reported in Ref. [60]. The heating rates were close to 10,000 K/s, much lower than those anticipated for ESD ignition. Interestingly, nanothermites with both Bi_2O_3 and Fe_2O_3 serving as oxidizers and showing prompt ESD ignition in the present experiments at reduced voltages, were reported to ignite at lower temperatures when placed on a heated filament compared to the thermites with oxidizers CuO and MoO_3. This correlation supports qualitatively the ESD ignition mechanism involving Joule heating of the powder by the discharge current [79]. The present observations show that the ESD energy was sufficient to heat particles of $2Al{\cdot}Fe_2O_3$ and $2.35Al{\cdot}Bi_2O_3$ above their ignition threshold before the end of the ESD pulse. On the contrary, pre-heating particles of $2Al{\cdot}3CuO$ and $2Al{\cdot}MoO_3$ by low voltage ESD triggered a self-sustaining but slow, low-temperature reaction causing the observed ignition delay. Only at higher ignition energies was prompt ignition observed for CuO and MoO_3 based composites.

Prompt ignition observed here for powders placed in 0.5-mm thick layers appears to be qualitatively similar to the immediate ignition observed for the nano-thermite powders placed in monolayers, described in Refs. [50, 90]. Rapid combustion of particles placed in monolayers and heated nearly instantaneously by ESD was interpreted in Ref. [90] suggesting that the nano-structure of the reacting particles was preserved because the reaction occurred primarily over the interfaces existing in the mechanically milled nanocomposite material. This hypothesis is consistent with the observed

structures of the combustion products shown in Figure 3.5, where products containing Fe and Bi are well dispersed in molten Al_2O_3. Additional images of the collected combustion products are shown in Figures 3.10 and 3.11 for $2Al{\cdot}Fe_2O_3$ and $2.35Al{\cdot}Bi_2O_3$ powders ignited as both 0.5-mm thick and monolayers. For $2Al{\cdot}Fe_2O_3$, the combustion products from the ignited powder monolayer (Figure 3.10, left image) include composite particles with dimensions comparable to those of the initial milled material. Parts of the composite clearly formed from molten reacted material; other parts have not obviously reacted. Combustion products from the 0.5-mm thick powder layer (Figure 3.10, right image) consist of clearly molten and reacted material, while what appears to be unreacted composite particles are present as well. Whether these unreacted particles belong to the same original composite particle, or were deposited coincidentally is not yet clear. The particle sizes are somewhat greater than for the starting powder, suggesting that particles agglomerated. The reacted material shows components mixed in a broad range of scales. A large, deformed portion of the particle comprises Al_2O_3. The brighter part decorated with multiple spherical inclusions is a mixture of iron-rich, partially oxidized material and Al_2O_3.

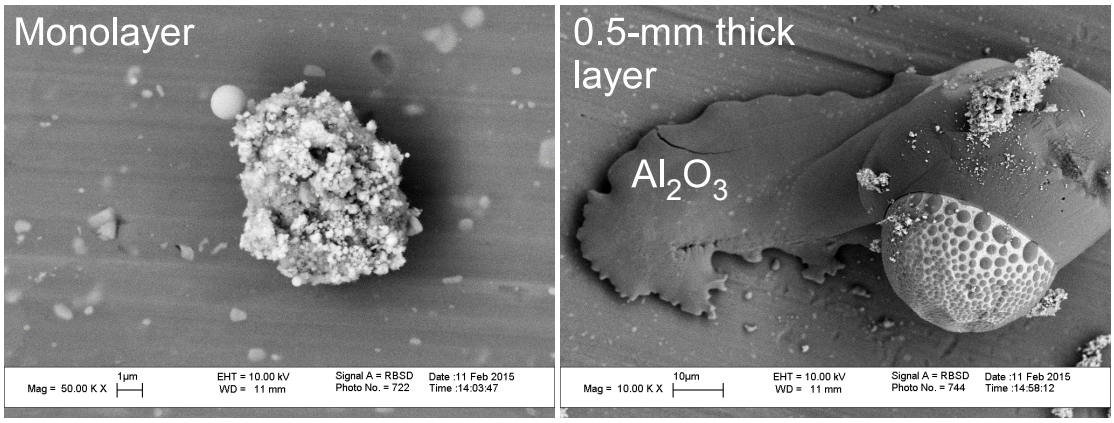

Figure 3.10 SEM images of combustion products for $2Al{\cdot}Fe_2O_3$ composite powder ignited as a monolayer and as a 0.5-mm thick layer.

For $2.35Al{\cdot}Bi_2O_3$, the combustion products from the ignited powders from both the monolayer and the 0.5-mm thick layer are compared side by side in Figure 3.11. In both cases, the components appear to be mixed in a broad range of scales. For the monolayer (Figure 3.11, left image), the particle appears to crack open, possibly upon impact on the collection substrate. The interior of the particle is mostly Al_2O_3. The external part is mixed, including fine composite structure and larger molten particles, with mixed oxide phases. Similarly, for the products collected from the 0.5-mm thick layer, some particles include Bi-rich exterior and Al_2O_3-rich interior. In Figure 3.10, right image, that for one of the particles, the interior is exposed in a fracture in the particle. The Bi-rich surface layer itself is not homogeneous and consists of mixed oxide phases. The structure with Bi-rich shell and Al_2O_3 filled core is likely produced as a result of a difference in surface tension of the respective molten phases, with the surface tension of molten Al_2O_3 being substantially higher (~0.6 N/m [100]) compared to that of Bi-rich liquid (~0.37 N/m [101]). Parts of the product, similar to those for monolayers, consist of finely mixed, composite particles with structures similar to those of the starting ball-milled materials. As for $2Al{\cdot}Fe_2O_3$, the products collected from the 0.5-mm thick layer include somewhat coarser particles, suggesting that some agglomeration had occurred.

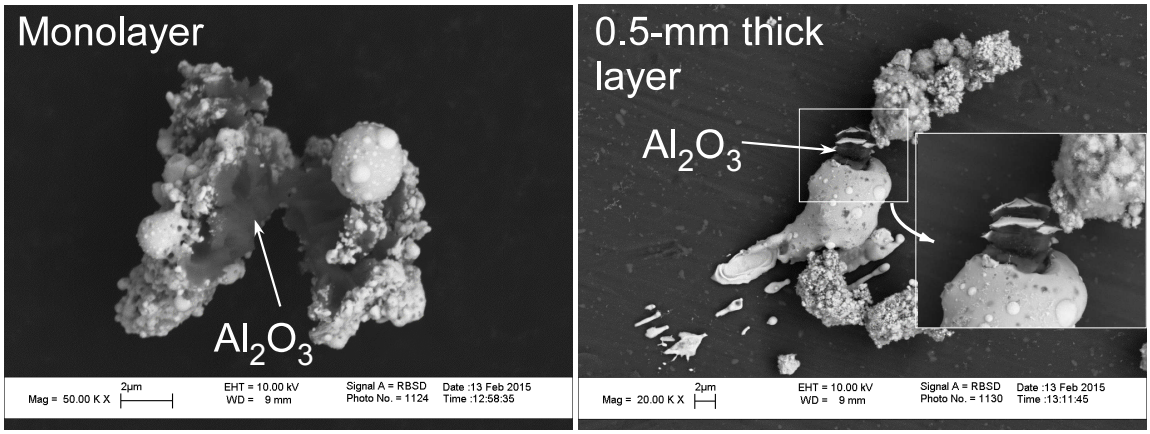

Figure 3.11 SEM images of combustion products for $2.35Al{\cdot}Bi_2O_3$ composite powder ignited as a monolayer and as a 0.5-mm thick layer.

Similarities in the product structures for the mono-layers and 0.5-mm thick layers of the same thermites suggest that most promptly-ignited particles react heterogeneously while preserving their nano-structure generated by milling. However, presence of larger particles suggests that agglomeration occurred; larger particles explain somewhat delayed peak positions and longer overall burn times for thicker layers, as shown in Figure 3.3. Interaction among a large number of particles directly heated and ejected by the spark may also explain the accelerated peak onset, observed for the thicker layers. Particles located in the middle of the ejected powder cloud were surrounded and thus thermally shielded by other igniting particles. Such shielded particles would heat up faster because of reduced heat losses. This faster heating would cause a faster increase in the optical emission, registered as the emission peak onset. For monolayers, the number of ejected particles is much smaller, and thus interactions between different igniting and burning particles are negligible.

3.6.2 Delayed Ignition

Delayed ignition was observed for all materials and the differences in timing of the delayed emission pulses were relatively minor. For a characteristic delay of the peak position of about 1 ms, the heat in air can propagate over about 1 mm. As observed from Figure 3.9, the density of the ejected powder cloud is sufficiently large to include many particles within a 1-mm radius. Thus, delayed ignition likely represents a collective or group combustion within clouds of ejected particles. The intensity of the produced emission (and sound) pulses is most likely associated with the size of the burning powder cloud.

For $2Al{\cdot}3CuO$ and $2Al{\cdot}MoO_3$, for which only delayed ignition was observed at lower ignition energies, the igniting clouds must have been substantially greater compared to those of $2Al{\cdot}Fe_2O_3$ and $2.35Al{\cdot}Bi_2O_3$. This difference is likely associated with a greater disparity in the temperatures and speeds of ejected particles between the two groups of materials.

For the powders experiencing prompt ignition, some of the ejected particles are burning. Such particles are expected to move faster than cold ejected particles. The difference in speed is due to both natural convection and self-propulsion due to ejected gases, well documented in the early literature for metal particle combustion [102-107]. Because of the difference in speed, the zone of thermal influence for such burning particles is relatively narrow and is lined along their trajectories.

If the discharge does not trigger prompt ignition, many ejected particles are instead pre-heated; however, none of them are burning. Preheated ejected particles produce a cloud that is initially heated rather homogeneously. The temperature of such a

pre-heated cloud continues to increase nearly uniformly throughout the entire group of lifted particles. This leads to nearly simultaneous ignition of a much greater number of particles compared to those heated by a few rapidly moving hot particles for the promptly igniting powders. It is further likely that ignition of a relatively large powder cloud causes ejection and ignition of powder remaining in the sample holder. This secondary ejection and ignition are more likely when the size of the initially ignited cloud is greater, in agreement with the data in Table 2.

It is interesting to compare temperatures achieved at the delayed ignition peak with the adiabatic flame temperatures anticipated for respective materials. Such adiabatic temperatures were calculated using NASA CEA code [108] and are shown in Table 3.3 (99 wt. % air (O_2/N_2 mixture) and 99 wt. % N_2 were used for diluents). Two calculations were performed for each material, except for $2.35Al{\cdot}Bi_2O_3$, because of lacking necessary thermodynamic data. In both calculations, constant pressure configurations were considered at 1 atm. In one calculation, 1 atm of air was included in the reaction; in the other, the thermites were considered to react in nitrogen. For completeness, reaction temperatures reported in Reference [5] for all the studied thermites are also shown. These latter temperatures represent the adiabatic thermite reactions without heat exchange with surroundings. For $2Al{\cdot}Fe_2O_3$, the experimental flame temperature (Figure 3.7) is between the values shown in Table 3.3. However, for both $2Al{\cdot}3CuO$ and $2Al{\cdot}MoO_3$, the experimental temperatures are higher; the discrepancy is particularly significant for $2Al{\cdot}3CuO$. The implied temperatures are outside of the calibrated temperature range and thus are extrapolated using the obtained calibration. Experimental values were obtained from fitting a rather broad portion of the emission spectra with

Planck's formula and the fits were quite good, especially at the peak and the decaying portion of the measured emission traces. Therefore, even if there is an error due to extrapolation, it is likely that the measurements represent superadiabatic heating achieved in the burning nano-thermite clouds in these experiments. Such superadiabatic combustion could occur if powder, which was being ejected from the sample holder, was entering air, substantially pre-heated by combustion of the powder ejected and ignited previously. Clearly, the temperature distribution was non-uniform, whereas optical temperature measurements must have been biased to the highest temperature in optically thin clouds.

Table 3.3 Adiabatic Flame Temperatures for Thermite Predicted by NASA CEA Code

	Adiabatic flame temperature (K)			Experiment
Material	**In air**	**In nitrogen**	**Ref. [5]**	(K)
$2Al{\cdot}3CuO$	2460	2530	2843	4400 - 5100
$2Al{\cdot}MoO_3$	2957	2612	3253	3500 - 4400
$2Al{\cdot}Fe_2O_3$	2916	2360	3135	2600 - 3100
$2.35Al{\cdot}Bi_2O_3$			3253	2400 - 2700

Source: [108].

3.7 Conclusions

Two distinct ESD-induced ignition regimes were observed for aluminum-based nanocomposite thermite powders placed in 0.5-mm thick powder layers. Promptly ignited powders began burning immediately during the ESD pulse. Prompt ignition occurred for the powders using Bi_2O_3 and Fe_2O_3 as oxidizers when low-voltage ESD was used. Because these powders were reported to ignite at lower temperatures compared to

other thermites studied here, their prompt ignition indicated that a threshold ignition temperature was achieved as a result of Joule heating of selected particles even in the relatively weak, low-voltage ESD. Combustion that followed prompt ignition was dominated by individual burning particles; however, some of the ejected particles agglomerated causing longer burn times compared to those reported earlier for the same powders ignited by ESD as monolayers. The burn rates of the promptly ignited particles were high and their combustion products contained components mixed on a fine scale, comparable to the scale of mixing in the starting nanocomposite materials prepared by arrested reactive milling. Delayed ignition was observed for all materials. At low voltage ESD, much stronger delayed ignition pulses were observed for powders with CuO and MoO_3 as oxidizers that did not exhibit prompt ignition. Respective combustion products contained phases mixed on a substantially coarser scale compared to that in the starting powders, suggesting that the nano-scale fuel-oxidizer structure of the prepared materials was destroyed upon their ignition. Delayed ignition represents combustion of clouds of interacting powder particles. Larger clouds were produced for powders with CuO and MoO_3 as oxidizers as a result of more homogeneous self-heating among powder particles pre-heated and ejected by ESD. Larger clouds of burning nanothermites burned superadiabatically so that their measured flame temperatures exceeded significantly those predicted by thermodynamic calculations. The effect was particularly strong for 2Al·3CuO, which also showed higher burn rates for powder clouds.

CHAPTER 4

COMBUSTION CHARACTERISTICS OF STOICHIOMETRIC AL-CUO NANOCOMPOSITE THERMITES PREPARED BY DIFFERENT METHODS

4.1 Abstract

Three nanocomposite materials with the same nominal stoichiometric thermite composition of 2Al-3CuO were prepared by three different methods: ultrasonic mixing (USM) of constituent nanopowders, electrospraying (ES), and arrested reactive milling (ARM). Prepared powders were placed in a 6.7-mm diameter, 0.5-mm-deep cavity in a brass substrate and ignited by electro-static discharge. The experiments were performed in air, argon, and helium. The mass of powder removed from the sample holder after ignition was measured in each test. Using a multi-anode photo-multiplier tube coupled with a spectrometer, time resolved light emission traces produced by the ignited samples were recorded in the range of wavelengths of 373–641 nm. Time-resolved temperatures were then determined by fitting the recorded spectra assuming Planck's black body emission. Temporal pressure generated by ignition events in the enclosed chamber showed that the powder's combustion properties were tied to both their preparation technique as well as the environment they were ignited in. We found that agglomeration of nanoparticles hindered combustion of USM powders; while it was not observed for the ES powders. In oxygen-free gas environments, lower temperatures and pressures were observed for USM and ES powders prepared using starting nano-particles. For the ES powders, the effect of gas environment was less significant, which was interpreted considering that ES materials included gasifying nitrocellulose binder, enhancing heat,

and mass transfer between individual Al and CuO particles. Higher pressures and temperatures were observed in inert environments for the ARM-prepared powder.

4.2 Introduction

Nanocomposite thermites have attracted attention recently due to a range of potential applications, especially those in pyrotechnics [17, 109-112]. Their fast energy release combined with high energy densities make nano-thermites more attractive than conventional thermites made of micron-scale powder particles [12, 14, 15]. The increased reactivity of nanocomposite thermite is due to a highly developed interface between metal fuel, typically aluminum, and an oxidizer comprising a metal oxide, most commonly, CuO, Fe_2O_3, MoO_3, Bi_2O_3, etc.

Several methods have been recently developed to prepare nanocomposite thermites, with each method imparting specific structural characteristics to the generated nanocomposite. The most common technique employs physically mixing nanopowders of individual components [113, 114]. The powder is suspended in a liquid, commonly hexane, and is mixed using ultrasonic agitation, following which the liquid is evaporated. The produced materials, often referred to as metastable intermolecular composites or MIC's, are explored as potential reactive or energetic materials. Due to the inherent agglomeration of the as produced nanopowders, such samples can exhibit poor mixing at the nanoscale if such agglomerates are not broken up during the ultra-sonication. Moreover, during the evaporation of the solvent fuel and oxidizer nanopowders may re-agglomerate preferentially, leading to a poorly mixed composite. A modified method for enhancing the nanoscale mixing of nanopowders involves the addition of an organic

binder to the ultrasonicated mixture of nanopowders. The generated suspension is dispersed into an aerosol using an electrospray [23, 29] which generates uniformly sized (<10 μm) droplets of the suspension. When the solvent dries from the electrosprayed droplets, it leaves behind a composite particle, held together by the binder. The resulting composite particles are micron-sized (~ 1 μm) albeit mixed at the nanoscale and offer processing advantages compared to nanopowders. Upon ignition, the binder is gasified at a temperature below the ignition temperature of the MIC, causing particle-particle separation, which is thought to diminish sintering and rapid loss of reactive surface area [115]. Yet another method for the preparation of well mixed nanocomposite material is Arrested Reactive Milling or ARM [80], which uses high energy ball milling of starting micron-sized components, to prepare fully dense composite powders. Sizes of produced composite powder particles vary in the range of 1 – 100 μm with each particle containing starting materials mixed on the nanoscale.

This work is aimed to characterize the similarities and differences between combustion behaviors of reactive materials comprising a nanocomposite thermite: stoichiometric Al-CuO (2:3 per mole basis), prepared in three distinct ways. The methods of preparation include traditional ultrasonic mixing (USM) of nano-powders [112, 116-118], electrospraying (ES) [23, 24, 115, 119], and ARM [46, 80, 120]. The results are expected to emphasize the effect of the material structure and morphology on its ignition and combustion. Such material comparisons are needed to guide further developments in the reactive material preparation technologies as well as to enable fine-tuning of specific characteristics of different materials.

4.3 Materials

The ES and USM composites were created using 50-nm copper oxide from Sigma-Aldrich and 50-nm aluminum from Argonide Corporation (70% active). The USM materials were prepared through the ultrasonication of copper oxide in ethanol for 1 hr. before aluminum was added; whereby an additional 1 hr. of ultrasonication was performed to ensure good physical mixing of particles. For the ES composites, the precursor mixing procedure was similar. Collodion solution of 4-8wt.% nitro cellulose in ethanol/diethyl ether (Sigma-Aldrich) was diluted with a diethyl ether (99.8%)/ethanol (99.8%) mixture (1:3 volume ratio) to which stoichiometric mixture of aluminum and copper oxide was added, limiting the nitrocellulose content to 5 wt. % of the total solids loading. The mixture was sonicated for an hour followed by 24 hours of magnetic stirring. The precursor solution was subsequently loaded into a syringe pump and electrosprayed onto an aluminum foil. The foil was placed at a suitable distance away from the needle such that the field necessary for the electrospray was maintained as well as sufficient transit time was available for the solvent in the droplet to evaporate. The sprayed composite powder was subsequently harvested off the foil for further experiments. A more detailed explanation of the process can be found in Reference [23].

The ARM materials were prepared as described elsewhere [46]. The starting materials were -325 mesh (less than 44 μm), 99.5% pure aluminum by Atlantic Equipment Engineers and 25 μm, 99+% pure copper (II) oxide by Sigma Aldrich. A Retsch PM400 planetary mill was used with custom-made thick-walled hardened steel vials. The Al and CuO were milled using 9.525 mm (3/8”) diameter hardened steal balls with the ball to powder mass ratio of 3:1. Hexane was used as a process control agent

(24 mL per vial). The material was milled for approximately 60 min and stored under hexane. The powder used in the experiments was stored for up to 2 years. Its reaction was preliminarily examined using differential scanning calorimetry (DSC) in argon, which showed no detectable effect of aging on the observed thermite reactions.

Figure 4.1 shows scanning electron microscope (SEM) images of all three types of thermite powders. The images were taken using backscattered electrons which offered brightness contrast based on the molecular weight of the involved phases. The brightness difference between Al and CuO is detectable, with CuO particles generally appearing slightly brighter than Al owing to the larger atomic mass of copper. Mixing between Al and CuO appears to be somewhat more homogeneous for ES and USM materials compared to the ARM-prepared composite. Individual inclusions of CuO in the ARM material are slightly coarser than particles of CuO in both ES and USM composites. USM composite appears to be most porous, although substantial porosity is also observed in the ES particles. Conversely, most of the ARM particles are fully dense.

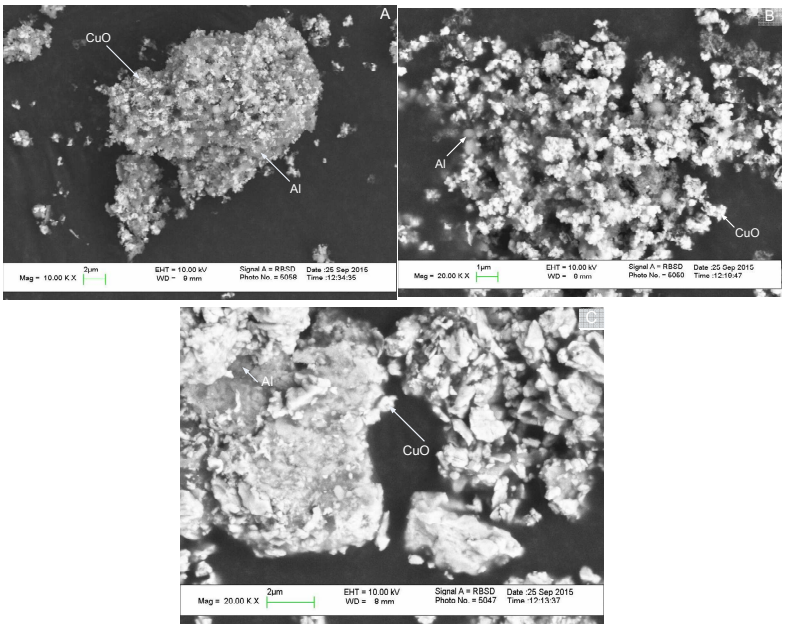

Figure 4.1 SEM images of different 2Al-3CuO nanocomposite powders: A: ES, B: USM; C: ARM.

4.4 Combustion Experiments

All powders were ignited using an experimental setup based on a 931 model Firing Test System by Electro-Tech Systems, Inc. The experiment was discussed in detail earlier [50, 77, 90] and only a brief summary is given here.

The powders were loaded to completely fill a 0.5-mm deep, 6.7-mm diameter cylindrical void in a brass sample holder. Excess powder was removed using a razor blade to ensure a flat top surface. The mass of the loaded powder depended on porosity of the sample. Typically, the mass loads of the ES, USM, and ARM composites varied in the ranges of 3.87 – 4.53, 6.11 - 7.21, and 16.4 – 19.4 mg, respectively. The powder-filled sample holder was placed 1 mm away from the pin-electrode. Experiments were performed inside a sealed chamber (6.24×10^{-4} m^3) filled with air, argon, or helium up to 101.325 kPa. For experiments in argon and helium, the chamber was evacuated to 67.7 kPa and then filled with the corresponding gas. This process was repeated three times to minimize the oxygen concentration down to 1.55 mol/m^3 or to a total of 8.85×10^{-4} mol of oxygen in the chamber. In most experiments, the electro-static discharge (ESD) was produced by discharge of a 2000-pF capacitor, preliminarily charged to a voltage of 10 kV. To ignite the ES powder in helium, it was necessary to increase the voltage to 20 kV and use a 10000-pF capacitor (all ES He runs will be noted by an asterisk* throughout the paper). The capacitor discharge was triggered electronically. Three runs were performed for each environment and powder for a total of nine runs per powder.

Aluminum foil preliminarily cleaned with acetone was mounted onto SEM stubs using double-sided carbon tape to collect combustion products. The foil was placed 18-22 mm from the powder-loaded sample holder. All parts of the ESD apparatus were cleaned with

acetone prior to each test to avoid cross contamination between products of different materials. Samples were weighed before and after ignition using an Acculab ALC-80.4 balance, in order to determine the amount of powder removed from the sample holder and thus participated in each combustion event.

Emission signals produced by ignited materials were collected using a 32-channel spectrometer based on a Hamamatsu H7260 series linear array multi-anode photo-multiplier tube (PMT). The wavelengths for the 32 channels were in the range of 373.4 - 641.0 nm. The time resolution of the individual emission traces recorded for each wavelength was 5 μs, which was determined by the National Instruments PCI-6133 DAQ-boards used for data acquisition. National Instrument's Labview 8.5 software was used to collect the data; the results were processed using a customized code in MATLAB. The data processing included calculation of the temperature based on the recorded spectrally resolved emission traces using Planck's formula. The spectrometer output was calibrated using a tungsten filament lamp and a NIST traceable StellarNet EPP-2000 spectrometer. Additional details are available elsewhere [121]. Pressure measurements were made using a PCB Piezotronics Model 106B51 Pressure Transducer installed in the ESD chamber and connected to a PCB Model 482A21 signal conditioner and to a LeCroy WaveSurfer 64Xs Series oscilloscope.

4.5 Results

4.5.1 Material Ejected From the Sample Holder

Fractions of the powder mass ejected from the sample holder for different materials are shown in Table 1. It is observed that most of the loaded powder was ejected and thus expected to burn in all experiments. However, it is unclear whether the reaction was complete for all materials. The effect of gas environment on the fraction of the powder ejected from the sample holder is relatively minor. Note that the absolute masses of the powders ejected for each material are affected by the density of the sample. The densities are also shown in Table 4.1; the ARM-prepared powder has the highest density, followed by the USM, and then by ES materials.

Table 4.1 The Percent of Powder Ejected upon ESD Ignition

Composite type	Loading Density (g/cm^3)	Percent of 2Al-3CuO lost after ignition Environment		
		Air	Argon	Helium
ES	0.080 ± 0.012	76.1 ± 9.0	83.6 ± 8.9	90.3 ± 6.0
USM	0.13 ± 0.04	91.8 ± 2.9	85.7 ± 7.8	87.5 ± 2.1
ARM	0.32 ± 0.03	88.2 ± 1.2	87.6 ± 1.1	82.9 ± 2.9

4.5.2 Emission Data

An example of the light emission traces collected using the 32-channel spectrometer is shown in Figure 4.2. The emission pulses produced by the spark itself were no longer than 5 – 6 μs, i.e., they were much shorter than the traces shown. Emission intensity peaks between 500 and 600 nm. It is also apparent that the emission at longer wavelengths becomes stronger for longer times, indicating a decreasing temperature.

For clarity, comparisons between different types of thermite powders are illustrated in Figure 4.3 using one selected emission trace corresponding to 567.7 nm. This wavelength was chosen due to its similarity to the filtered emission traces recorded in previous experiments [90, 121]. It is also not expected to interfere significantly with molecular emission bands of AlO [122]. Typical traces of all three composite powders (ES, USM, and ARM) ignited in various environments (air, argon, and helium) are shown in Figure 4.3. Signal amplitudes differ, with the signal produced in air being the strongest for all powders. Comparison of pulse amplitudes for different materials may be misleading because of systematic difference in the total amount of burning material caused by the difference in densities among different types of powders filling the sample holder. As shown in Table 4.1, the density was highest for the ARM-prepared powder. Respectively, more material was loaded and ignited in each test, causing stronger overall emission intensity.

The signals peak at the shortest times for the USM powder; the peak position is most delayed for the ES material (except for ignition in He, when a higher ESD energy was used). It appears that the preparation method has a stronger effect on the temporal position of the peak intensity than the gas environment.

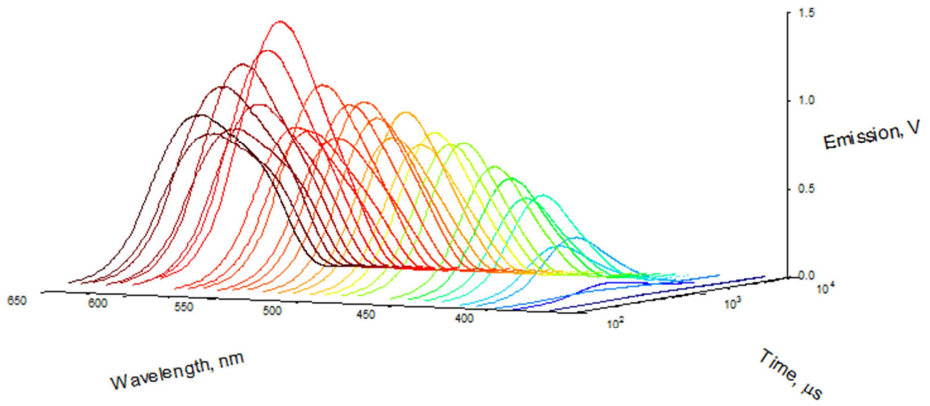

Figure 4.2 Characteristic emission traces recorded using the 32-channel spectrometer for a USM-prepared 2Al-3CuO nanocomposite thermite ignited in air.

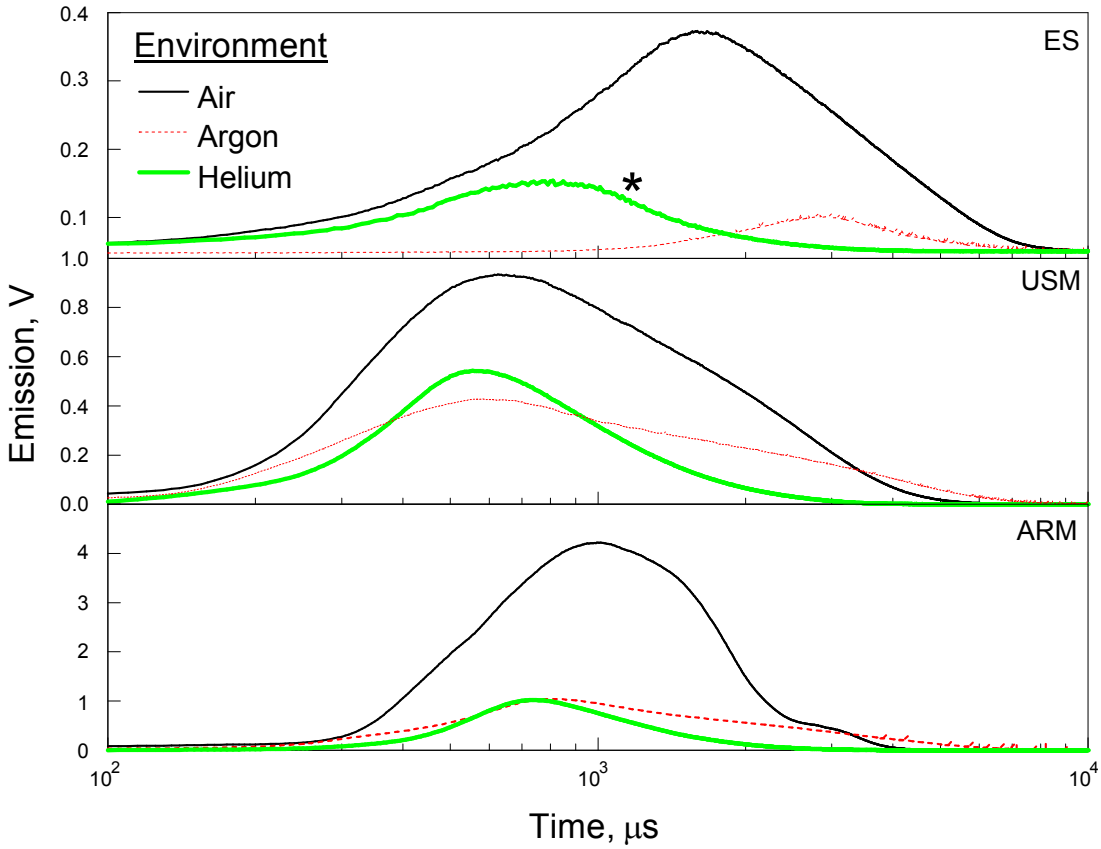

Figure 4.3 Emission traces (567.7nm) for different nanocomposite thermite powders ignited by ESD in different environments.

Collected 567.5-nm emission traces were processed to establish their main temporal characteristics. The parameters of interest include peak onset (determined by the first peak of the signal's time derivative), peak position (determined at 100% of the peak height or t_{100}), peak width (determined as the time while the signal exceeds 50% of its peak value (or period between characteristic times t_{-50} and t_{+50}), and burn time (determined when the signal decreases to 10% of its peak value, t_{10}). The processing results are shown in Figure 4.4. Note the logarithmic time scale when comparing times. The peak onset times as well as t_{-50} and t_{100} are the longest for the ES and the shortest for the USM powders, except for the ES powder in helium, when a higher ESD energy (20 kV, 10000 pF) was used. In that latter case, all three initial characteristic times occur much earlier, although the overall duration of the emission pulse is nearly the same for all materials. The peaks observed in helium are shorter than in air or argon for all materials. For ES and USM powders, the emission traces ended at approximately the same time in both air and argon. For ARM-prepared powder the trace in argon was longer. For all materials, the peak width is greater in air than in inert gas environments. In air, the peak width is greater and peak position is further delayed for the ES material. The narrowest peak and shortest peak position delay (t_{100}) is observed for the USM powders for all environments.

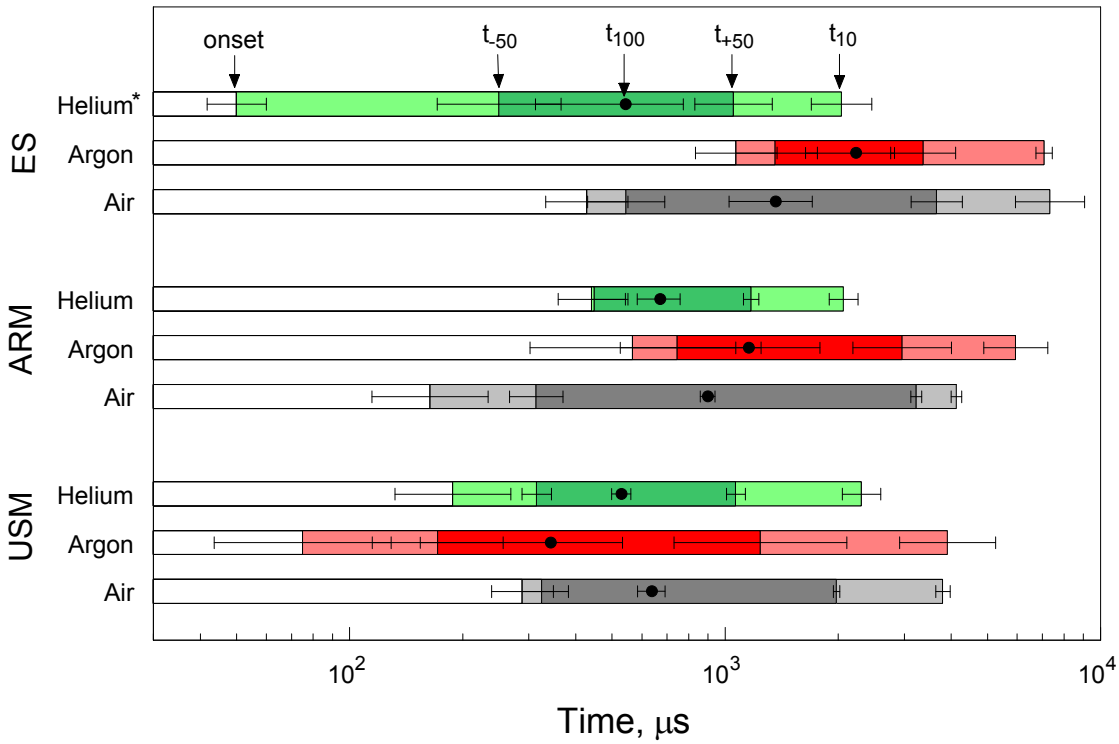

Figure 4.4 Temporal characteristics of Al-CuO powders at 567.7nm wavelength in various environments.

4.5.3 Temperature and Pressure Data

Emissivity was assumed to be independent of the wavelength to obtain black body emission temperatures using all 32 recorded filtered emission traces. A wavelength-depending emissivity, e.g., following a $\varepsilon \sim \lambda^{-2.94}$ trend [99] was considered; however, the goodness of fit for the respective Planck's curves was substantially reduced; thus the gray body assumption was maintained. Figure 4.5 shows a typical 32-channel trace for ARM powder in air overlaid with the respective temperature. The error bars for temperature indicate 95% confidence intervals. The temperature peaks when the emission intensity is increasing, at around 400 μs. The peak temperature is about 2830 K, close to the adiabatic temperature of 2810 K predicted for the stoichiometric Al-CuO reaction by the CEA equilibrium code [108]. The temperature is reduced to about 2500 K by 1 ms, when

most emission traces are close to their maximum values. The presently measured temperatures are slightly higher than 2250 – 2400 K, the range of temperatures measured for the USM-prepared Al-CuO nanothermites burning in an unconfined pile or in an open tube [123]. Furthermore, the present temperatures exceed ca. 2300 K obtained for individual ARM-prepared 2Al-3CuO particles [54]. Qualitatively, the temperature traces appeared to be similar to one another for all materials. Therefore, no additional temperature traces are shown.

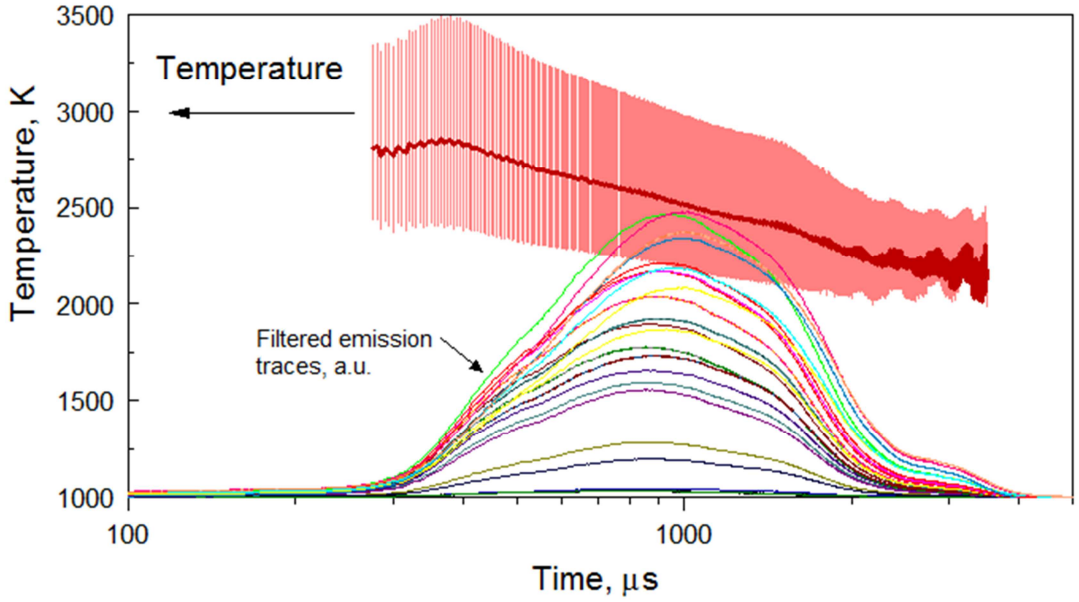

Figure 4.5 Temperature (in bold red) overlaid with filtered emission traces for ARM-powder.

For comparisons between materials, the single temperature value taken at the peak position (t_{100}) of the emission trace filtered at 567.7 nm was considered for all samples. Temperatures for different powders ignited in different gas environments are shown in Figure 4.6. For ARM materials, temperatures in air are somewhat lower than those reported for argon and helium. Conversely, for USM and ES powders, the temperatures

measured in air are higher than those observed in inert gas environments. The effect of temperature is weaker for ES than for USM powder.

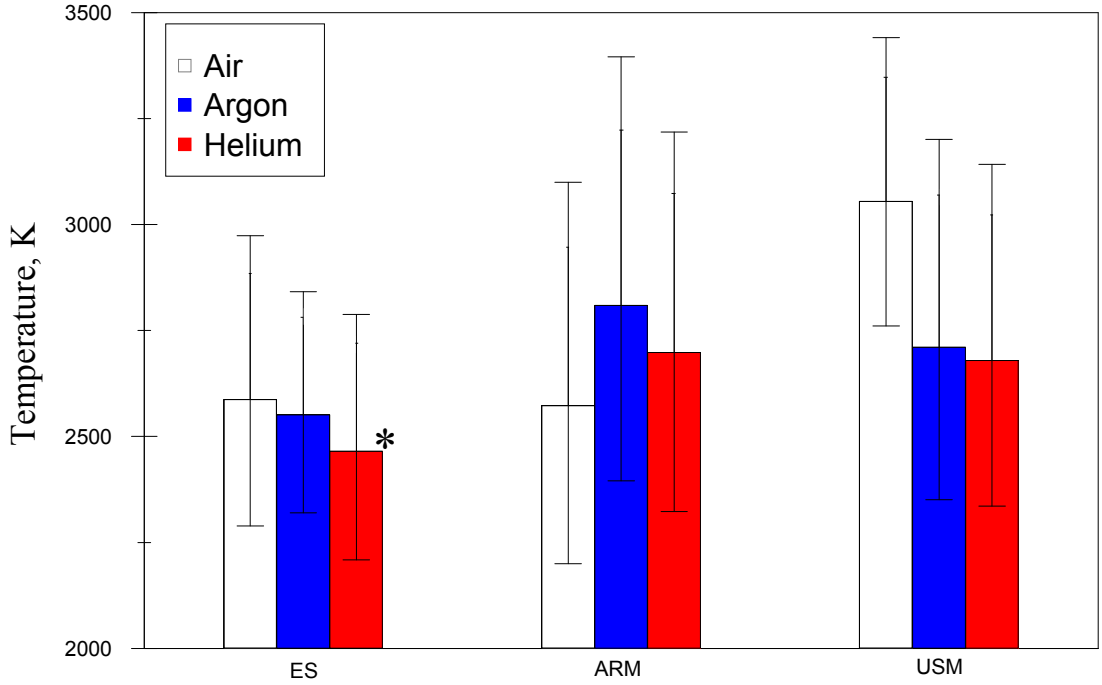

Figure 4.6 Temperatures taken at the emission peak measured for the 567.7-nm emission for different materials ignited in different environments.

Pressures recorded for different powders ignited in air are shown in Figure 4.7 along with filtered 567.7-nm emission traces. The pressures are normalized per unit mass of the powder ejected from the sample holder, and thus expected to participate in the reaction. Therefore, normalized pressures shown can be directly compared for different types of powders. The pressure signals are expected to be delayed from the emission by the time the sound wave needs to travel from the ignited powder to the pressure transducer. This time can be estimated as approximately 0.6 ms, assuming the speed of sound in the chamber to be 340 m/s and the distance to the pressure transducer to be close to the chamber characteristic dimension, e.g., 20 cm. Indeed, the pressure trace begins

after a 0.6-0.7 ms delay. However, the pressure peak is observed some 10 ms following the peak of the emission signal, indicating a truly delayed signal. This delay suggests that the exothermic reaction continues for the entire duration of the observed emission signal, even during its decay, causing further heating of the gas inside the chamber. This heating of the gas in an enclosed chamber combined with the release of gas phase combustion products creates the respective pressure rise. Oscillatory patterns observed in the pressure traces occur with an approximately 0.5-ms period, and thus are likely to represent reflections of the sound wave within the chamber. The oscillations are stronger for signals with higher overall pressures.

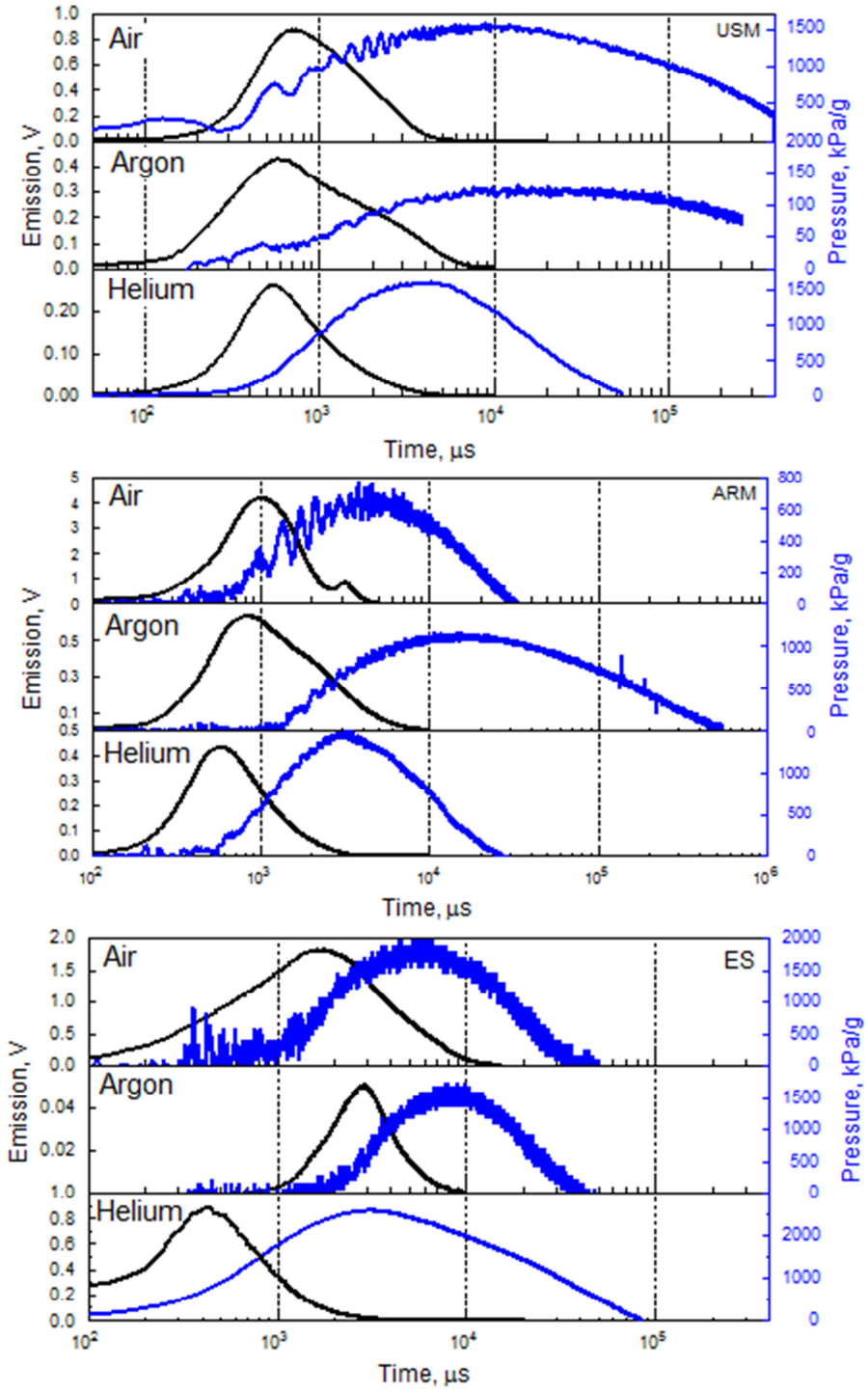

Figure 4.7 Pressure traces (thick blue lines) overlaid with emission traces for all environments and materials.

The temporal characteristics of pressure traces are summarized in Figure 4.8, similar to the analogous plot for the emission traces in Figure 4.4. The onset of the pressure pulse occurs sooner for USM materials, except for the case of ES powder ignited in He, when a higher voltage was used. Aside from the case of ES powder ignited in He, the onset of the pressure pulse occurs sooner in air than in inert gases. The pressure peak positions (t_{100}) follow the same trend for all materials: pressures first peak in He, then in air, and finally in Ar. For the ES powder, despite a delayed pressure peak position observed in Ar, the overall pressure signal in Ar is shorter than in other gases. Conversely, for ARM powder the duration of pressure peak in Ar is much longer than in air and He. For USM powder, the pressure peaks have approximately the same duration in Ar and air; the peak in He is much shorter.

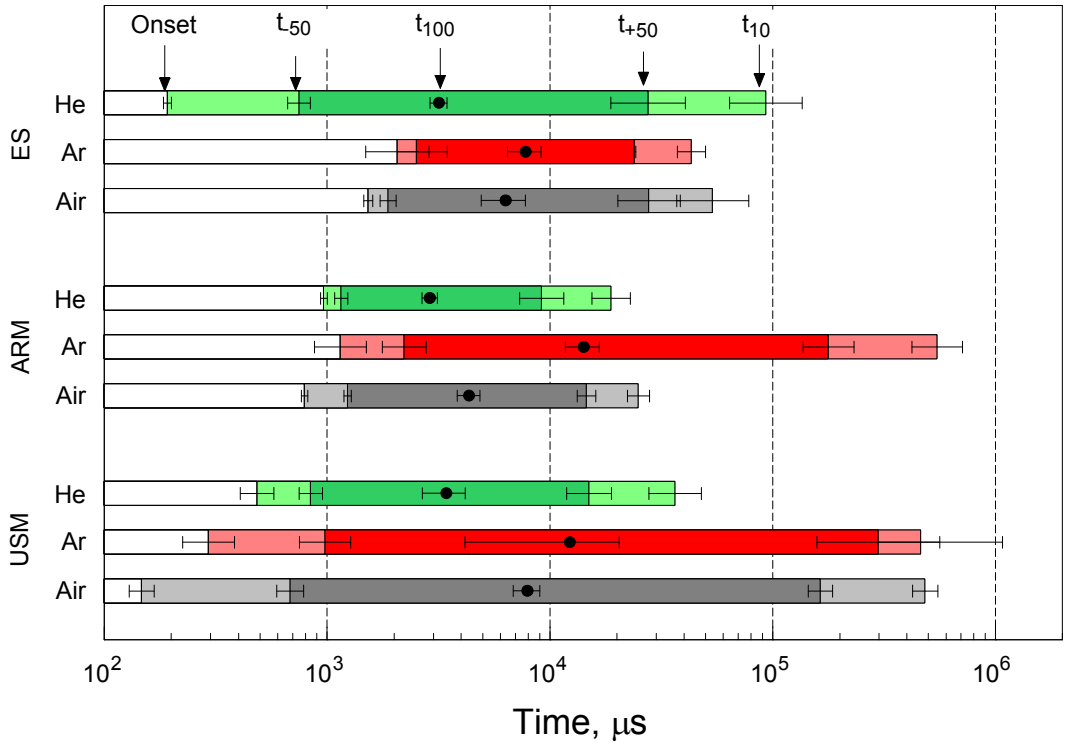

Figure 4.8 Temporal characteristics for pressure traces for all powders in different environments.

Pressure peak values normalized per unit mass of the ignited material are compared for different powders in Figure 4.9. The effect of gas environment is different for different powders. For USM powders, the highest pressure is observed in air. Ignition becomes difficult for this sample in Ar; very low pressures were observed in some tests, causing a very large error bar. Conversely, in He, USM powder ignited readily and generated pressure that was nearly as high as in air. For the ARM powder, the pressure in air is lower than in both Ar and He. In both inert gases, the pressures for ARM powder are close to each other. This trend correlates well with that observed for the temperatures for this powder in Figure 4.6, which are also higher in inert gases. The ES powders generated the highest pressures in both air and Ar; however, they did not ignite in He when the same ESD energy was used. When an increased ESD voltage was applied, ignition occurred and the pressure was substantially higher than for other materials.

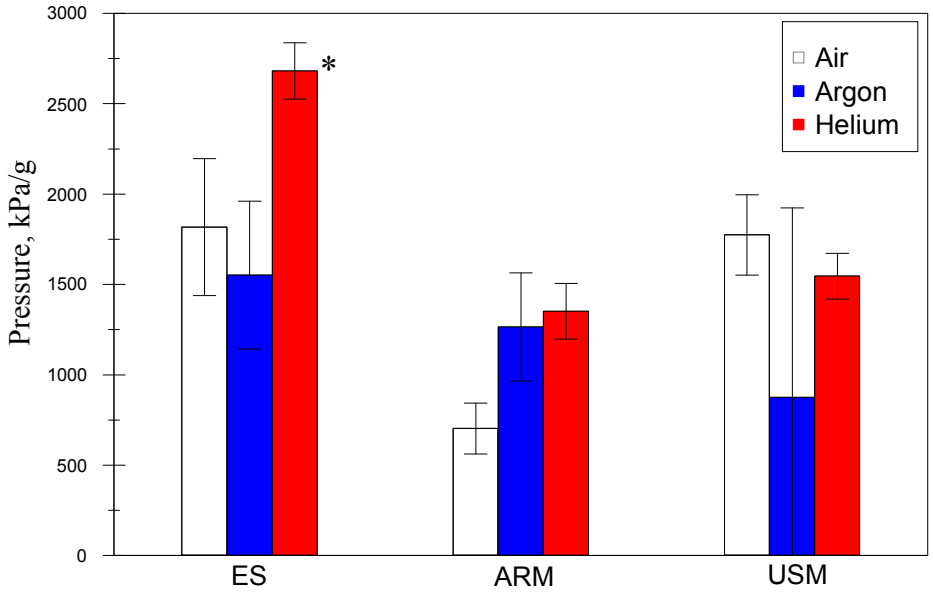

Figure 4.9 Maximum pressures obtained from the ESD ignition of various Al-CuO powders under different environments.

4.5.4 Combustion Product Morphology

Particles ignited in air were collected and examined under SEM. Characteristic images for ES-prepared, USM, and ARM particles are shown in Figure 4.10. In addition to relatively coarse particles as shown in Figure 4.10, much finer spheres, representing typical smoke particles, were observed for all materials; few such particles can be seen in Figure 4.10A.

In Figure 4.10, a particle most representative of the combustion products was selected among many acquired SEM images for each material. For all combustion product particles, phases containing primarily Al_2O_3 (darker gray in SEM images) and Cu (bright) can be readily distinguished. In many cases, Cu-rich phase forms a characteristic "cap", somewhat similar to an oxide cap observed on quenched aluminum particles [124, 125]. Prevalent particle sizes are different for products of different materials. The finest particles were observed for the ES powders; the particle size varied in the range of 1 – 2 μm [23]. For both ARM and USM powders, particles were mostly coarser, with a characteristic dimension in the order of 10 μm. It appears that the morphology of the original composite material is completely lost for both ARM and ES powders. The particle shapes, scale of mixing among products, and surface morphology are likely representative of cooling fairly well homogenized mixed molten products. However, in Figure 4.10B, an agglomerate of original aluminum nano-particles can be distinguished for the USM powder. The agglomerated particles appear to be "bonded" together with a brighter, Cu-rich melt, apparently percolating through the pores in the initially agglomerated particles.

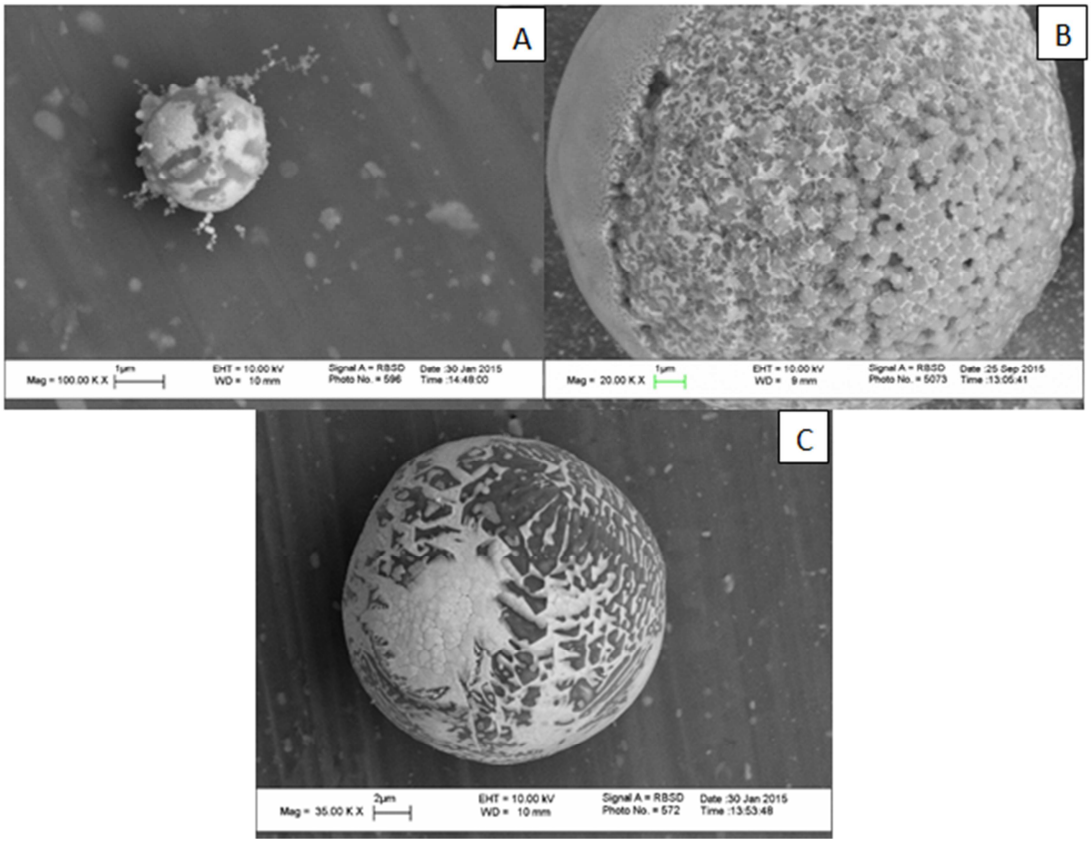

Figure 4.10 SEM images of combustion products of different 2Al-3CuO powders ignited in air. A: ES; B: USM; C: ARM.

4.6 Discussion

It is of interest to consider similarities and differences in the ignition and combustion behaviors among 2Al—3CuO powders prepared by different methods and ignited by ESD. Further, the present results can be compared to earlier measurements, employing the same technique for igniting nanothermite powders [121] as well as to reports describing combustion of Al-CuO nanocomposite ignited in different experimental configurations [54, 123]. To set the framework for the discussion, consider the following events induced by the ESD discharge striking a powder sample. First, the spark produces a shockwave and heated plasma that aerosolizes some of the powder. The size of the

aerosol cloud is between 2 and 3 cm, depending on the ESD energy and the density of the powder. Most of the lifted powder is cold, although a fraction of particles that was hit by the spark directly is heated and ignited nearly instantaneously. These directly heated particles begin reacting within single microseconds following the spark discharge. These times are typically shorter than necessary for the temperature to equilibrate across particles or agglomerates with dimensions of tens of μm. Thus, the nano-structure of such particles or agglomerates is preserved during their ignition. The heat from the ignited and burning particles ignites the rest of the aerosol, which occurs with a delay caused by the time necessary for the heat to propagate through the powder cloud. This delay is typically of the order of tens of ms; thus aluminum in the composite material melts causing sintering for USM powder or loss of nano-structure for the ARM-prepared material. Therefore, once ignited, many such particles will have lost their nanostructure. Presence of nitrocellulose in the ES powder may prevent or delay the particle sintering. The ignited powder cloud generates additional convective flow, which lifts more powder. The newly lifted powder ignites once it is being mixed with the burning powder. Once again, the ignition delays are long enough for the nanostructure to be lost upon ignition.

Temporal characteristics of the optical emission traces summarized in Figure 4.4 for different materials can be correlated with events occurring in respective combustion experiments. The initial ignition delay, reflecting ignition of particles heated directly by ESD is best represented by the initial emission onset time, shown for all materials in Figure 4.4. Aside from the experiment with ES powder in He, when a higher ESD power was used, the delays are longer for ES powder, indicating most likely a slower initial low-temperature solid-solid reaction between Al and CuO, which may be separated in

this material by binder. Heating of the ES powder by the spark current could also have been less effective because of its greater electrical resistance. When the ESD energy is increased, for the ES powder ignited in He, the emission onset time is markedly reduced, suggesting that the particles were preheated to a much higher temperature during the ESD pulse.

When multiple aerosolized particles are ignited, combustion products may remain incandescent for an extended period of time, because they form a relatively large cloud. Thus, the total emission time is representative of the time scale describing heat and mass transfer from the burning powder cloud.

The peak of the optical emission signal may represent both growth of the cloud size and/or density and increased rate of reaction for the burning particles. Setting aside the case of ES powder in He, when a greater ESD energy was used, the peaks of emission occur at the shortest times for USM powders and at longest times for the ES powder, with the ARM powder being in the middle for all environments, mirroring the trend observed for the emission onset. Because the mass of ARM powder loaded in the sample holder was the greatest, it formed the densest clouds. This is consistent with the strongest emission signal observed for this powder (see Figure 4.3). Therefore, the densest cloud produced by the ARM powder generated its strongest emission signal earlier than that generated by the lowest density cloud produced by ES powder. This observation can be interpreted assuming that the cloud combustion rate is affected by the ignition rates of individual particles, which are lower for the ES powder, as mentioned above. For USM powder, the reaction slows down early, most likely because it is incomplete and because agglomerated particles, such as shown in Figure 4.10b, extinguish.

The end of incandescence is expected to indicate the cooling of the cloud and end of the reaction; however, interpreting this incandescence is difficult because it is also affected by both size and brightness of the cloud. Conversely, the measured pressure traces represent fairly accurately the heat released in the reaction; the effect of gas products is expected to be comparatively weak for the present thermite combustion experiments. The presence of nitrocellulose in the ES material is also not expected to affect pressure significantly. Based on the mass of powder and nitrocellulose percentage added (5%), only about 0.2 mg of nitrocellulose was included in an individual ES powder load. It roughly translates into 5–10·10–5 moles of gas if fully gasified. The chamber contained close to 2.5·10–2 moles of air, and thus an additional pressure caused by gasification of nitrocellulose would only change the total pressure by about 0.02–0.04%. The primary cause for pressure increase is the heat release; thus, the peak of the recorded pressure signal represents the end of the exothermic reaction rather accurately. Indeed, the peak pressure roughly coincides with the end of the optical emission trace for all powders (Figure 4.7).

It is interesting that the peak pressures occur at approximately the same times for all powders ignited in He. The trend in Figure 4.8, showing the peak position as a function of the gas environment is also the same for all powders. The times are shortest in He (~ 2 ms) and longest in Ar (7 – 15 ms). It may suggest that the duration of a combustion event is correlated with the time of heat and mass transfer over the volume occupied by the ejected powder cloud, which is roughly the same for all powders. The durations of the combustion events for all samples are similar to those measured for individual ARM-prepared Al-CuO particles in Ref. [54]. This observation suggests that

for ARM-prepared powders, the burn times of individual particles may be close to the characteristic transport time in the cloud of the ESD-ejected powder. However, the present burn times are much longer than reported for ES and USM materials, ignited in a miniature combustion cell [23].

The temperatures inferred from the emission traces for all materials are close to those reported earlier for similar nanothermites [54, 123] ignited in different experimental configurations. The difference in the temperatures observed for different powders in various environments may be caused by both pressure wave affecting ejection of unignited powder, the rate of heat loss from the burning particle cloud to the rest of the chamber, and also by the mass of the burning material. A difference in the initial density of differently prepared powder samples may affect their ejection, and thus affect the measured temperature. The low density of ES powder may therefore explain the slightly lower temperatures observed for this material in Ar and He, when much smaller amounts of this powder are being ejected and thus produce clouds, which cool faster despite the relatively low thermal diffusivity of Ar.

Finally, it is interesting to correlate differences in the observed combustion behavior and morphologies of the combustion products collected for different powders. Dimensions of agglomerates observed in the as prepared USM powder (Figure 4.1B) are roughly similar to the dimensions of agglomerated combustion products of the same material (Figure 4.10B). The porosity of the original agglomerates is reduced and pores are seen to be filled by molten Cu-rich material. CuO melts at about 1600 K, a temperature that is expected to be above the ignition point of nano-aluminum. A partially reduced oxide, Cu_2O melts at a lower temperature (ca. 1500 K); it may start forming even

before aluminum melts. Even more importantly, the eutectic in the mixed Al_2O_3 – CuO system occurs at around 1100 K [126], so that the produced liquid spinel phase (Al_2CuO_4) may block the surface of aluminum, reducing the rate of its further reaction at a much lower temperature. The melt apparently wets the aluminum surface, stabilizing the agglomerates for this material.

Presence of relatively large agglomerates may also explain an inconsistent ignition and large spread among measured pressure values observed for USM powder in Ar, as opposed to air and He. In air, the thermite reaction is assisted by aluminum oxidation with ambient oxygen. Thus, reaction rate may be high even for porous agglomerated particles, in which aluminum remains exposed to ambient oxygen. In He, the rate of heat transfer is very high, making it easy to ignite particles ejected in a cloud containing burning agglomerates. Conversely, in Ar, the rate of heat transfer is low, so that substantial ignition delays may occur for particles ejected from the sample holder. For larger agglomerates, ignition may or may not be achieved, depending on their size and specific direction in which they are ejected. As a result, substantial variation in the measured pressure may be observed.

For the ARM-prepared powder (Figure 4.10c), the size of the particles found in combustion products is roughly similar to the sizes of the initial fully dense particles (Figure 4.1c). Low-magnification SEM overviews of the collected ARM powders (not shown for brevity) indicated that particles were burning in close proximity of one another; some agglomeration of the burning particles was also observed. The characteristic dimensions of Cu-rich and Al2O3 inclusions or clusters were greater than those of the CuO and Al domains in the initial nanocomposite material. This suggests

that, as explained earlier, the particles lose their nano-structure upon ignition. The pressure amplitudes for ARM powder are higher in Ar and He (Figure 4.9), unlike for ES and USM powders. This may be explained by relative independence of combustion of ARM particles on the presence of the external gas oxidizer. In fact, when ambient oxygen is available, it is likely that in presence of Al or Al2O3, partially reduced CuO forming Cu2O reoxidizes generating Al2CuO4 spinel, which slows down ensuing oxidation of aluminum. This is a kinetic effect, caused by the formation of stable protective layers of the oxidized phases separating Al and CuO. This reoxidation of copper is qualitatively supported by the color of the smoke created by the combustion event. A yellow/green smoke was observed in air, suggesting a mix of various copper oxidation products. However, in both inert environments the smoke was a brilliant red indicative of a pure metallic copper. In these environments, the lack of external oxidizer may be hypothesized to prevent formation of the spinel, making reaction of Al with CuO and Cu2O more favorable.

Finally, for the ES powder, the sizes of product particles are noticeably finer than for both USM and ARM materials (Figure 4.10a). Individual product particles were relatively far from one another, suggesting no or insignificant agglomeration between them. This is consistent with the ES particle structure, including a gasifying binder (nitrocellulose), which disperses initially agglomerated particles. It is further consistent with the relatively low total mass of the particle loads for this powder. The effect of gas environment on the burn time (time t100 for pressure, for example) is the weakest for this powder, suggesting that the gasifying nitrocellulose may actively affect the heat and mass transfer between dispersed Al and CuO particles.

The need for a higher ESD voltage required to ignite the ES powder in He may be explained by combination of small particle sizes, high rate of heat losses due to higher thermal diffusivity if helium, and low initial density of the powder in the sample holder. The particles ignited directly by ESD at 10 kV did not generate sufficient pressure to eject and ignite additional materials. When the ESD energy was increased (20 kV at 10,000 pF), more material was ignited directly by ESD, so that the energy produced by the initially ignited cloud was sufficient to lift and ignite more material.

4.7 Conclusion

Three powders with the same nominal composition 2Al-3CuO (numbers representing moles) but prepared by different methods, including USM, ES, and ARM, were prepared and ignited by ESD. For each powder, experiments were performed in air, argon, and helium. Both USM and ES powders comprised of porous micron-sized agglomerates of Al and CuO nanoparticles; ARM-prepared particles consisted of micron-sized fully dense particles in which Al and CuO were mixed on the scale of ~100 nm. Combustion temperatures measured for all materials optically were close to their estimated adiabatic flame temperatures and comparable to earlier reported similar materials burning in different configurations. For all materials, combustion times, ranging from 2 to 15 ms, were longer than expected for individual nanoparticles but in the range, anticipated for composite particles prepared by ARM or large agglomerates present in the USM powder. The shortest burn times were observed in He consistently for all powders. The ignition delays were longer for the ES powders in all environments, suggesting that the presence of binder delayed thermite reaction initially.

Pressure generated by combustion of powders prepared by ARM increased in the inert environments as compared to that in air; an opposite trend was observed for both USM- and ES-prepared powders. This is interpreted considering that the reaction with ambient oxidizer is less important for the fully-dense ARM-prepared particles compared to porous ES and USM materials, in which aluminum is always exposed to the ambient gas. While for ES and USM materials, ambient oxidizer accelerates oxidation of aluminum, for the ARM powder, in which CuO and Al are mixed in fully-dense composite structures, it causes formation of spinel, Al2CuO4. When produced, spinel is expected to impede further redox reaction, and thus slow down combustion of ARM prepared powder.

Powders prepared by USM formed large agglomerates; such agglomerates did not react completely and included multiple nano-Al particles bonded by Cu-rich oxidized phase. It appears that partially oxidized melt filled pores, blocking unreacted aluminum from further oxidation. Combustion products of the ARM-prepared powders had dimensions similar to those of the original material particles. The scale of mixing between Al2O3 and Cu-rich phase in the ARM powder combustion products was coarser than that between Al and CuO in the initial material. Combustion products of the ES powders consisted of the finest composite particles; their sizes appeared to be smaller than the sizes of the initial agglomerates observed in the ES powder. Unlike USM powders, the ES-prepared powders burned completely, with the reaction apparently supported by gasifying nitrocellulose binder, which could enhance heat and mass transfer between individual Al and CuO particles in inert environments.

CHAPTER 5

THE EFFECT OF HEATING RATE ON COMBUSTION OF FULLY DENSE NANOCOMPOSITE THERMITE PARTICLES

5.1 Abstract

The effect of heating rate on the combustion pathways of fully dense, micron-sized, nanocomposite thermite particles is examined. Stoichiometric nanocomposite thermites utilizing aluminum or zirconium as fuels were prepared by Arrested Reactive Milling (ARM) with several oxidizers (WoO_3, MoO_3, CuO, Fe_2O_3, and Bi_2O_3). The powders were ignited using both electrostatic discharge (ESD) and CO_2 laser beam. The particles ignited directly by ESD were heated at ca. 10^9 K/s while the particles ignited by laser were heated at ca. 10^6 K/s. Additional reference laser ignition experiments were performed with particles of pure Al and Zr. Optical emission of burning particles was recorded. For both Al and Zr-based thermites, burn times of particles ignited by the laser were slightly longer than for similarly sized particles of pure Al and Zr, respectively. This suggests that both Al and Zr-based thermite particles heated by laser lose their nanostructure immediately upon their ignition. Burn times and temperatures were compared for the particles of the same materials ignited using different heating rates. For Zr-based thermites, ESD generated burning particle clouds, with many particles ignited with a substantial delay and heated much slower than those ignited by ESD directly. Thus, direct comparisons were possible only for the Al-based thermites, for which both laser and ESD ignition yielded individual burning particles. It is observed that the ESD-ignited Al-based thermite particles burn much faster than the same particles ignited by

the laser. The difference in the burning regime of particles heated at different rates is interpreted observing that the rate of reaction in a particle heated up to the Al melting point is substantially higher in the ESD-heated particle compared to the same particle heated by the laser. After Al melts, the nanostructure of the composite particles may be lost; when this occurs the extent of thermite reaction in the ESD-heated particle is much greater than that in the particle heated by the laser.

5.2 Introduction

Thermites, reactive materials utilizing a metal fuel and a metal oxide as an oxidizer, have been successfully used in welding for over a century [1, 127-130]. However, traditional thermite reactions occur at low rates, have long ignition delays, and high ignition temperatures [17, 131-133]. In order to accelerate the thermite reactions and thus expand the range of their applications, various methods such as nano-powder mixing [113, 114], electrospraying [23, 29], magnetron sputtering [134], and high energy ball milling [13, 45, 80, 120] have been employed to mix the fuel and oxidizer on a finer scale. For rapidly reacting nanocomposite thermites, the range of possible applications extends to propellants (micro-thrusters) [135], lead free primers [75], explosives [95, 136], and sensors [137].

An increased area of the reactive interface is a distinct feature of various nanothermites, leading to qualitatively different ignition characteristics compared to conventional thermites. Their nano-structure leads to higher reaction rates and shorter ignition delays. However, this nanostructure is commonly expected to be lost during initial heating immediately after, or maybe even before ignition. Indeed, coalescence of

molten or just heated particles or domains of reactive components, called reactive sintering, was observed for many nanomaterials [68, 138, 139]. Once the nanostructure is lost, the material continues to burn as a regular micron-sized metal powder. However, different burn times were reported recently for nanocomposite thermite powders prepared by arrested reactive milling (ARM) [45] depending on heating source/heating rate. Particles that were ignited by CO_2 laser (heating rate on the order of 10^6 K/s) showed combustion rates consistent with typical metal particles (a few ms) [54] , while similar particles ignited by electrostatic discharge (ESD, heating rate on the order of 10^9 K/s) had burn times of only a few hundreds of μs [92]. An order of magnitude difference between the burn times of similar powder particles ignited by laser and ESD is unexpected, suggesting the possibility of a major shift in the respective combustion mechanisms. This shift could be caused by differences in the structures of burning particles. At the higher heating rates (10^9 K/s), the particle's structure may be preserved, making the condensed phase reaction between fuel and oxidizer nearly volumetric. By contrast, the particles heated less rapidly (10^6 K/s) lose their structure as the fuel melts and the components of the composite particles coalesce. A similar difference in the structure of burning thermite particles was recently proposed as responsible for two distinct ignition regimes observed for 0.5-mm thick layers of nanothermite powders ignited by ESD [140]. Prompt, nearly instantaneous ignition and high burn rates were recorded for particles directly struck by the discharge. A delayed ignition followed by much lower burn rates was observed for particles ignited as a result of self-heating in the powder layer, occurring well after the end of ESD.

This work is aimed at a direct characterization of the effect of heating rate on the burn rate of different nanocomposite thermite particles. Several thermite powders with different fuels and oxidizers are ignited using both laser and ESD. For each material, the experiments attempt to ignite individual particles rather than powder clouds. Burn rates identified from optical measurements are compared and results are interpreted considering possible changes in the structures of the nanocomposite thermite particles.

5.3 Materials

Ten nominally stoichiometric nanocomposite thermite powders with aluminum or zirconium as fuels and five different oxides as oxidizers ($2Al{\cdot}WO_3$, $2Al{\cdot}MoO_3$, $2Al{\cdot}3CuO$, $2Al{\cdot}Fe_2O_3$, $2Al{\cdot}Bi_2O_3$, $3Zr{\cdot}2WO_3$, $3Zr{\cdot}2MoO_3$, $Zr{\cdot}2CuO$, $3Zr{\cdot}2Fe_2O_3$, $3Zr{\cdot}2Bi_2O_3$) were prepared using ARM [45]. The powders were prepared using a customized Retsch PM400 planetary mill with 24 mL of hexane as the process control agent, and a milling medium of 9.525 mm (3/8") diameter hardened steel balls [90, 141]. To ensure the safety of both the operators and the equipment, custom-made hardened steel vials, capable of withstanding pressure of up to 20 atm were used (internal diameter 64 mm, wall thickness 18 mm, height 52 mm) [51]. The vials were loaded with 30 g of raw powders (Table 5.1) mixed stoichiometrically. The milling times were 60 and 180 min for the Al- and Zr-based thermites, respectively. The milling times were chosen based on preliminary experiments, in which powders prepared using different times were examined using a LEO 1530 Field Emission scanning electron microscope (SEM). The

milling time was selected as sufficient when formation of uniformly mixed composite particles was observed.

The milling protocol adopted here had previously been shown to result in fully-dense nanocomposites where generally the oxidizer is distributed as inclusions in the metal matrix [13, 51, 52, 55, 142, 143]. Previous systematic analysis of particle cross-sections showed inclusion sizes to be typically on the order of 100 nm or less [52].

Table 5.1 Raw Materials used to Prepare Nanocomposite Thermites

Material	Supplier	Notes
Al	Atlantic Equipment Engineers	-325 mesh, 99.5% purity
Zr	Alfa Aesar	2-3 μm
WO_3	Alfa Aesar	99.8% purity
MoO_3	Alfa Aesar	-325 mesh, 99.95% purity
CuO	Sigma Aldrich	25 μm, 99+% purity
Fe_2O_3	Alfa Aesar	-325 mesh, 99.5% purity
Bi_2O_3	Skylighter	325 mesh, 99% purity

Powders were sized in order to correlate the statistical distributions of the particle sizes and particle burn times measured in the laser ignition experiments. For the size measurements, particles were collected as they exited the powder feeder at the same location, where they would be ignited by the laser beam. Thus, possible particle agglomeration in the feeder was accounted for. SEM stubs with a conductive tape with double-sided adhesive coating were placed above the powder feeder, while the laser was turned off. The powder samples collected were examined using the SEM. Two different magnifications were used to ensure that both larger and smaller particles are adequately resolved and represented in the collected images. Particle size distributions were

obtained for each magnification and then merged following an earlier described methodology [144]. From the images, such as the ones shown in Figure 5.1, it was observed that most powders contained composite thermite particles and unattached oxidizer particles. The latter could be distinguished by characteristic crystallite shapes and, for Al-based thermites, by a brighter color caused by the higher atomic mass. The unattached oxide particles did not burn, and thus they were discounted for the purpose of constructing the particle size distributions. The presence of unattached oxide particles means that the prepared thermite particles were fuel rich, although the specific composition of such particles was not determined.

The resulting particle size distributions are shown in Figure 5.2. In all but the $2Al{\cdot}Fe_2O_3$ case, the aluminum-based composite particles are larger with average size between 1 and 2 μm compared to zirconium-based composites with average particle sizes in the range of 0.5-1μm.

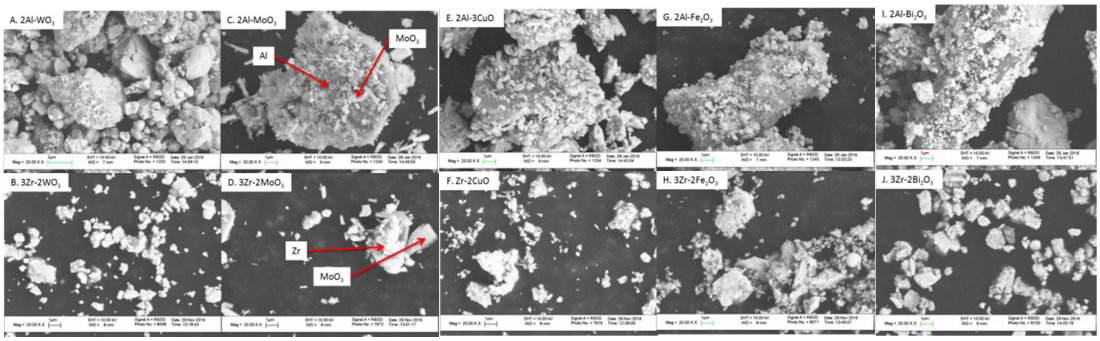

Figure 5.1 SEM images of the nanocomposite powders produced by ARM.

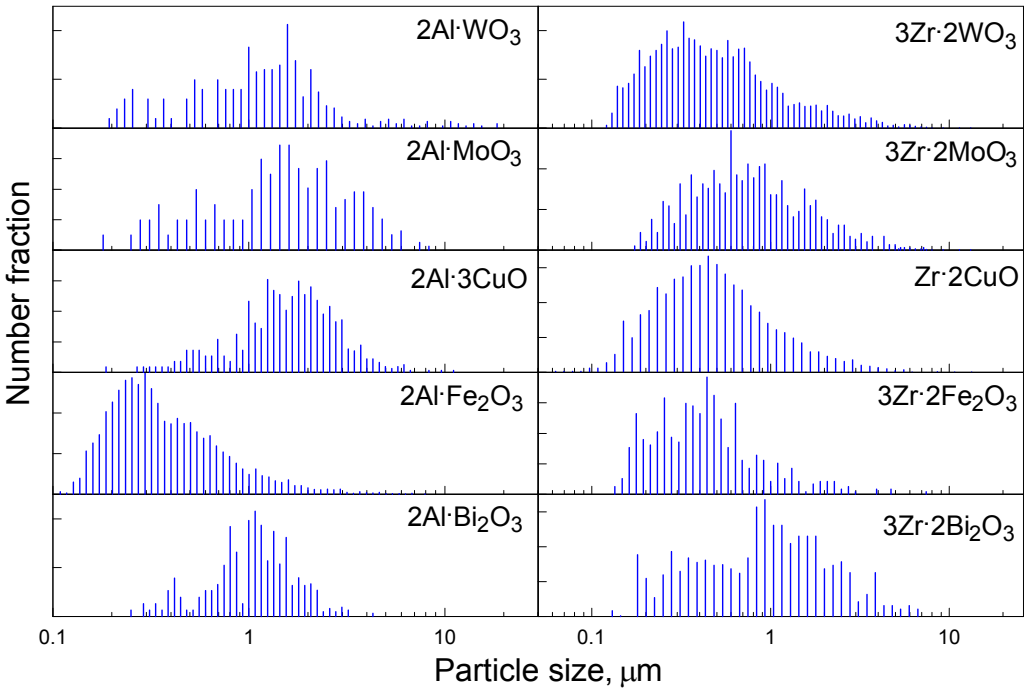

Figure 5.2 Size distributions for Al- and Zr-based nanocomposite thermites.

5.4 Experimental Details

A monolayer powder sample was ignited by an ESD generated using an Electro-Tech Systems 931 apparatus. The heating rate is estimated to be around 10^9 K/s based on the observed temperature rise of the ignited particles by at least 10^3 K during the ESD lasting for about 10^{-6} s. The powder monolayer was prepared using a thin slurry of the powder in hexane. The slurry was painted onto adhesive carbon tape, dried, and blasted with air to remove any loose particles. The tape was mounted on a brass sample holder. A 2000 pF capacitor was charged to 12 kV, and then discharged through a high-voltage pin-electrode, which was placed about 1 mm above the sample [50, 77]. A high-speed camera (MotionPro 500 from Redlake) was employed to capture images of the burning particles

in selected experiments. The images were taken every 2 ms, thus, only relatively long events could be observed.

For the laser ignition experiment, the same powders were loaded onto a custom-made screw feeder, described elsewhere [145-147]. The particles were carried by a laminar air flow through a 2.4-mm internal diameter tube with a brass nozzle with an aperture of 1.1 mm. The nozzle was placed 2 mm below a focused laser beam of a Synrad Evolution 125 sealed CO_2 laser. The thermite particles crossing the laser beam were heated and ignited. The heating rate in this experiment is estimated to be about ~10^6 K/s, which is based on the temperature rise of about 1000 K (observed for ignition of Al particles, [131]), the speed of the moving particles (ca. 0.5 m/s) and the laser beam diameter (about 300 μm). The 125 W laser was set to 30% power, enough to reliably ignite the thermite particles. This setup has been described in greater details earlier [148]. For reference, laser ignition experiments were also performed with pure Al and Zr powders.

Optical diagnostics employed two separate photo sensors. A single photomultiplier tube (PMT), model E849-34 by Hamamatsu fitted with a 568-nm interference filter was used in all experiments. For the ESD testing, the PMT was attached to a DS1054Z 4-channel 50MHz Oscilloscope. To ensure an accurate emission trace, separate blank emission traces of just the spark were taken and averaged. The average spark trace was then subtracted from the particle emission traces, eliminating background emissions. The second photo sensor was a 32-channel H11460-01 linear array multianode PMT assembly from Hamamatsu combined with an A10766-007-01 Hamamatsu spectrometer. The spectrometer's range was 373.4-641.0 nm. The

spectrometer's output was fed to four 8-channel BNC-2110 data acquisition boards by National Instruments enabling time resolution of 1 μs per channel. Planck's equation was used to fit the measured time-dependent emission spectra using temperature as an adjustable variable. More details about the calibration and temperature measurements can be found in previous work [141].

5.5 Results

5.5.1 Laser Ignition (Low Heating Rate)

Examples of emission traces of individual burning particles recorded using a 568-nm filtered PMT are shown in Figure 5.3. All traces for the aluminum-based thermites, except for the one with Bi_2O_3 as an oxidizer, begin with relatively sharp peaks with duration of ca. 10 μs. These peaks are likely produced while the particles are crossing the laser beam. Combustion proceeds with a relatively steady emission, although characteristic oscillatory patterns are observed for many particles. Such oscillatory patterns are typical in combustion of aluminum particles and are observed when burning particles spin while molten aluminum oxide caps are formed with emissivity different from that of the molten aluminum [149]. The burn times for the Al-based thermites were in the range of 0.2 – 10 ms.

The Zr-based thermite particles burned somewhat faster, with typical durations in the range of 0.2 – 2 ms. The pulses produced by the burning particles for all Zr-based thermites except for $3Zr{\cdot}2WO_3$ start with a relatively low-intensity, slow-rising signal followed by a stronger peak at longer burn times. No oscillatory emission was observed.

For some materials, e.g., $3Zr{\cdot}2Bi_2O_3$ and $3Zr{\cdot}2Fe_2O_3$ small peaks were observed by the end of the emission signal.

Multiple emission peaks were recorded for each material and the histograms showing distributions of the measured burn times were obtained (see details below). The histograms were correlated with those shown in Figure 5.2 for the particle sizes for each material.

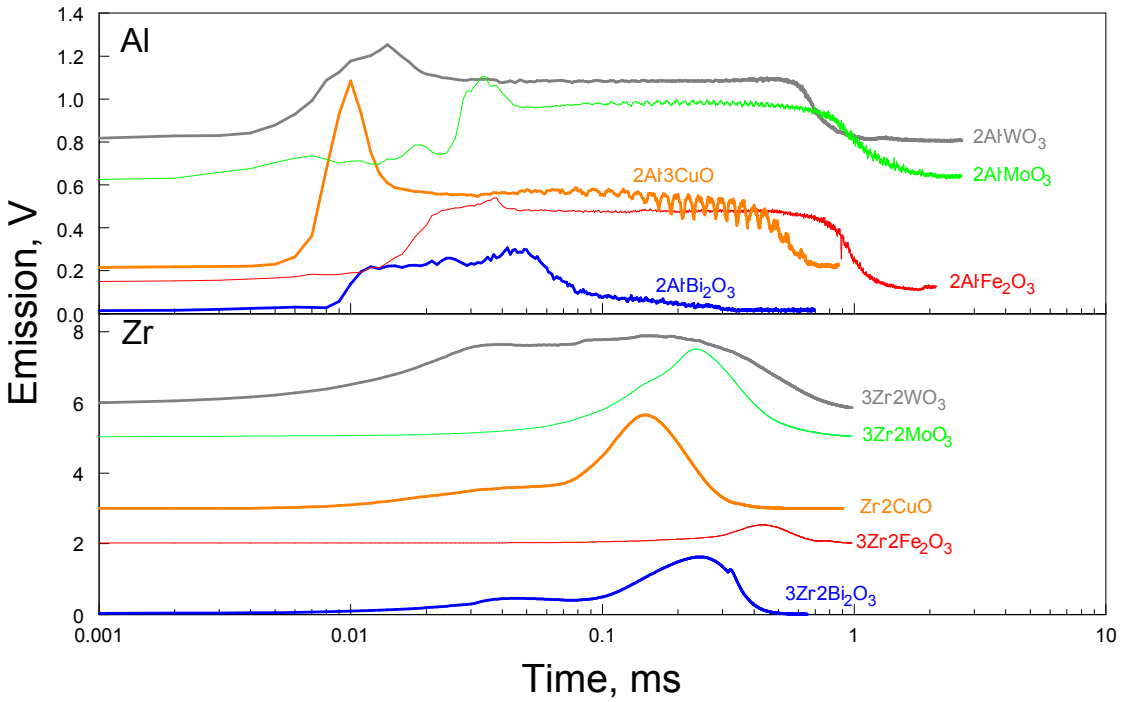

Figure 5.3 Examples of single particle emission traces captured by the 568 nm single PMT, ignited by laser.

From correlation between the distributions of burn times and particle sizes, trends for particle burn time vs. size were obtained as shown in Figure 5.4. In addition, such trends are also shown for pure Al and Zr powders. Similar experiments with Al and Zr were reported earlier [150, 151]; however, different data processing was used. Here, all

experiments were processed using the same approach, in which distributions of particle sizes are correlated with their respective distributions of burn times.

For all Al-based thermites, except $2Al{\cdot}Fe_2O_3$, the trends are very close. Particles of the thermite with iron oxide as oxidizer burn longer than all other thermite particles. The particle size distribution for $2Al{\cdot}Fe_2O_3$ shown in Figure 5.2 is most biased to small particle sizes, suggesting that smaller particles of this material burn as long as larger particles of other thermites. The material with the shortest burn times is $2Al{\cdot}3CuO$, although, as noted above, the difference between different Al-based thermites is relatively small. Table 5.2 shows parameters for the "*d*-power" law for estimating the burn times approximately based on the particle size for all materials. For all Al-based thermites, except for the $2Al{\cdot}Fe_2O_3$, the exponent *n* is greater than 1. For $2Al{\cdot}Fe_2O_3$, the exponent *n* is close to 0.9. For pure Al particles, the burn times are somewhat shorter than for the Al-based thermite particles of the same sizes; the exponent for the "*d*-power" law is close to 0.7.

For the Zr-based thermites, the material with iron oxide as oxidizer is also an outlier exhibiting the longest burn times. In this case, however, the particle size distribution for $3Zr{\cdot}2Fe_2O_3$ is in the same range as for other Zr-based composites. The trends shown in Figure 5.4 for all other thermites are grouped very closely with each other and with pure Zr. The "*d*-power" parameters shown in Table 5.2 show that the exponent *n* for all Zr-based thermites is close to 0.6 – 0.7, except for $3Zr{\cdot}2Fe_2O_3$, for which it is greater than 1.

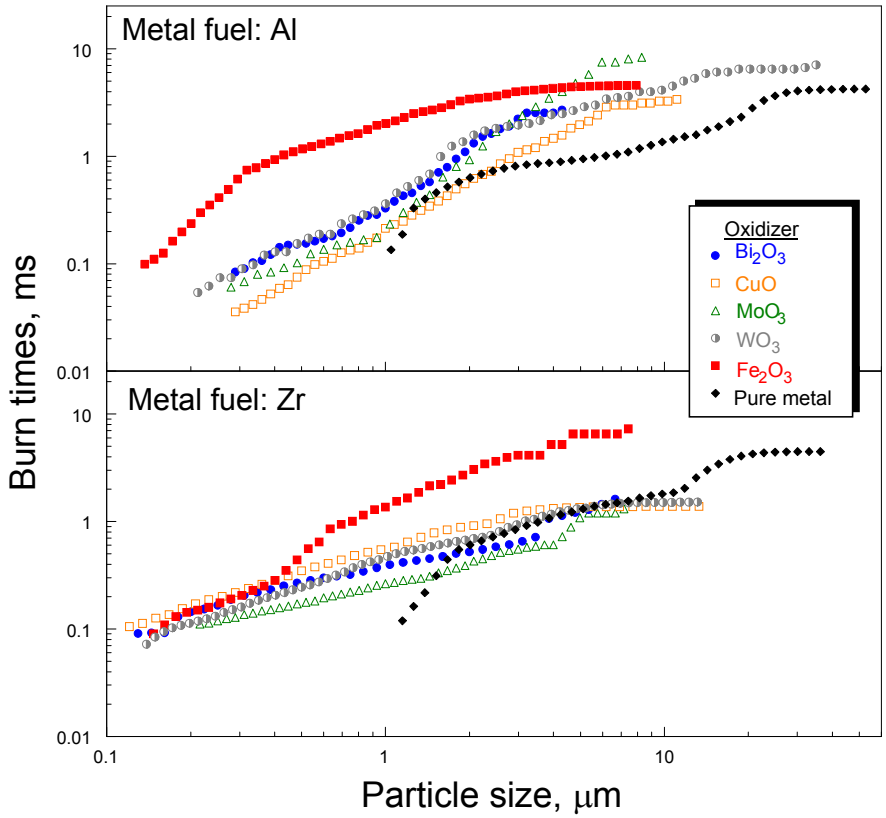

Figure 5.4 Correlations of burn times and particle sizes for laser-ignited powder particles.

Table 5.2 Coefficients *a* and *n* for the Burn Time, *t*, Expressed through Particle Size, *d* as $t=a \cdot d^n$

Fuel	Oxidizer	*a*, ms/μm^n	*n*
Al	-	0.30	0.72
	WO_3	0.40	1.13
	MoO_3	0.32	1.63
	CuO	0.21	1.35
	Fe_2O_3	1.46	0.87
	Bi_2O_3	0.40	1.41
Zr	-	0.25	0.90
	WO_3	0.39	0.69
	MoO_3	0.28	0.69
	CuO	0.49	0.59
	Fe_2O_3	1.06	1.18
	Bi_2O_3	0.39	0.65

5.5.2 ESD Ignition (High Heating Rate)

The experiments are illustrated in Figure 5.5, showing two subsequent frames of a high-speed video for ignition of a $3Zr{\cdot}2Bi_2O_3$ thermite powder. This frame sequence is typical for all ESD-ignited Zr-based thermites. The first frame, Figure 5.5A, is very similar to images observed for ignition of monolayers of all Al-based nanocomposite thermites [90]. Long particle streaks captured with an exposure time of 2 ms suggest that burning particles move rapidly from the sample holder. Such particles are accelerated by interaction with the shock wave produced by the ESD. However, the second frame, Figure 5.5B, shows a slightly larger cloud with much shorter particle streaks, suggesting substantially lower particle velocities. Such slowly moving burning particles can be formed when they are lifted from the sample holder and ignited by the convective flows generated by the flame initially triggered by ESD. Therefore, such slowly moving particles would be heated much slower than particles directly struck by the spark. The presence of a relatively slowly evolving powder cloud for all Zr-based thermites was further supported by examination of the sample holders. For all Al-based thermites, only a relatively small fraction of the powder directly struck by the spark was removed, as discussed in detail elsewhere [90]. However, for Zr-based thermites, the entire powder coating was removed from the surface of the carbon tape after each ESD ignition test.

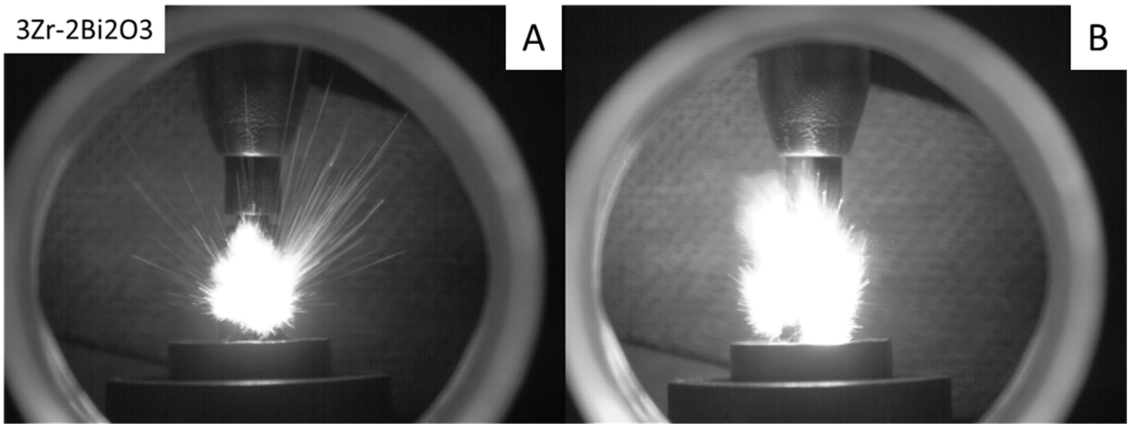

Figure 5.5 Subsequent high-speed video stills of the ESD-ignited $3Zr{\cdot}2Bi_2O_3$ powder. Time between frames A and B is 2 ms. For scale, the sample support is 25 mm in diameter.

Emission traces filtered at 568 nm for ESD-ignited Al- and Zr-based thermite powders are shown in Figures 5.6 and 5.7. For comparison, all the traces are overlaid with histograms showing distributions of burn times for respective powders ignited by laser. For all Al-based thermites (Figure 5.6), ESD-ignited powders produced single-peak traces. The durations and shapes of the single peaks were very close to each other for different Al-based thermites. The recorded emission signals are consistent with those reported earlier for the ESD-ignited monolayers of Al-based thermites [90]. Defining the burn time as the peak duration at 10% of its maximum height, one obtains the burn times of about 0.5 ms for all Al-based materials. The strongest emitters were the $2Al{\cdot}MoO_3$ and $2Al{\cdot}Fe_2O_3$, while $2Al{\cdot}Bi_2O_3$ was the weakest.

All emission peaks produced in the ESD-ignition experiments in Figure 5.6 are shifted to shorter times compared to the histograms showing the burn times for the same powders ignited by the laser. The ESD-ignition peaks are produced by multiple particles ignited simultaneously. Assuming that spark ignited particles of all sizes, it is expected

that the optical emission should last as long as the burn time for the largest particles. Therefore, the ESD peak durations that are much shorter than the longest burn times measured for individual particles ignited by the laser show that the burn rates for the same size powder particles were different in the two experiments.

Emission peaks produced by the ESD-ignited Zr-based thermite powders (Figure 5.7) have complex shapes. They all appear to include multiple overlapped peaks; the overall peak durations range between 0.8 and 2 ms. The longest peaks were consistently observed for $3Zr{\cdot}2MoO_3$ and $3Zr{\cdot}2Bi_2O_3$ powders. The complex shape, extended duration emission peaks are indicative of cloud combustion, in agreement with the images shown in Figure 5.5. Thus, burning clouds were produced by the Zr-based thermite powders even though the powders were prepared as monolayers, similarly to those of Al-based thermites. Because of the generated clouds, involving both particles ignited by ESD directly and particles ignited later and thus heated at lower rates, the comparison between the burn rates of the ESD and laser ignited particles for Zr-based thermites becomes indirect. Interestingly, the durations of the emission peak produced by the ESD ignited powders for Zr-based thermites are very close to the longest burn times of the respective laser ignited powder particles. This suggests that the particles igniting after the end of the spark and forming the observed clouds, burned as individual particles; i.e., there was negligible competition for external oxidizer in the burning particle clouds.

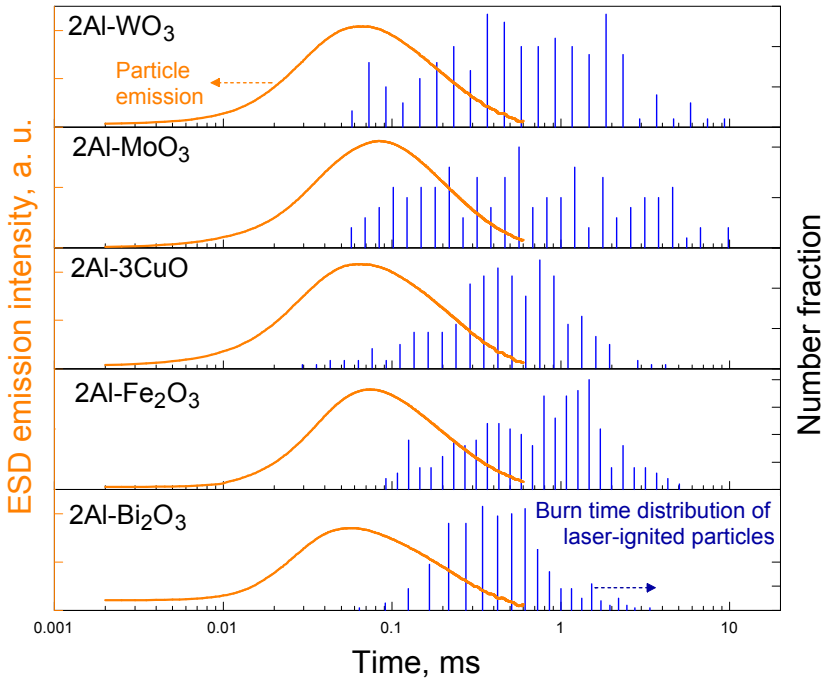

Figure 5.6 Burn time distributions for the laser-ignited powder particles overlaid with the 568-nm filtered optical emission traces produced by the respective ESD-ignited powders for Al-based thermites.

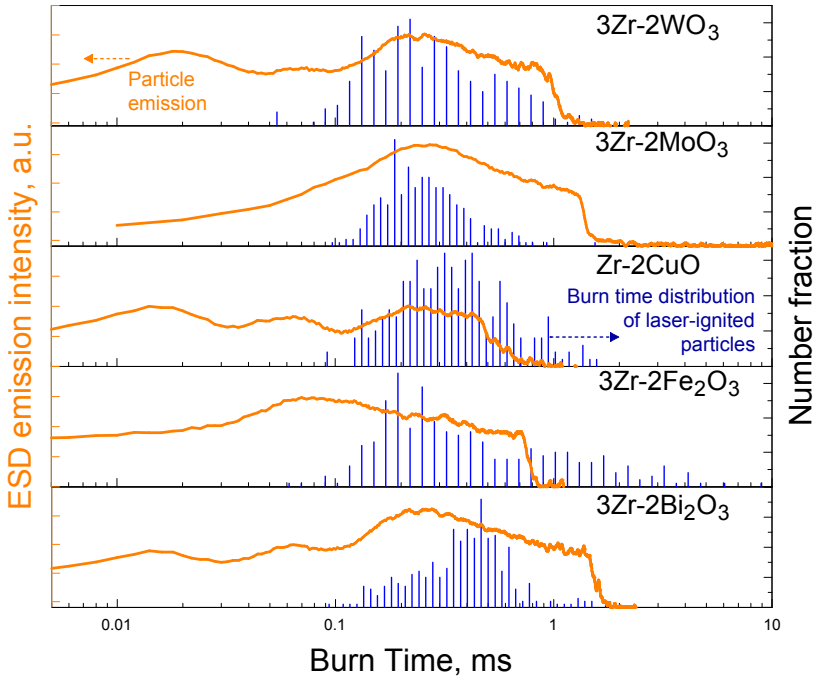

Figure 5.7 Burn time distributions for the laser-ignited powder particles overlaid with the 568-nm filtered optical emission traces produced by the respective ESD-ignited powders for Zr-based thermites.

5.5.3 Flame Temperatures

Because comparisons between ESD and laser-ignited particles are direct only for Al-based thermites, for which single particle combustion events occurred in both cases, the temperatures were measured and compared only for this set of materials. Characteristic single emission traces corresponding to the spectrometer output at 568 nm and respective temperatures, obtained by fitting each time-resolved spectrum with Planck's equation are shown in Figure 5.8 for the Al-based thermite with MoO_3 as an oxidizer. The results are shown for ESD and laser-ignited particles. Note that these emission traces are of self-heating particles that have already ignited, and are no longer being externally heated. The temperatures are shown for the portion of the signal, for which fitting of spectra to Planck's equation yields reasonable values with relatively small error, shown as the light red area representing a 95% confidence range for the temperature values.

The temperature traces are distinct for ESD and laser-ignited powders for each material; however, for all materials, the groups of traces for powders ignited by each individual trigger are qualitatively similar. All temperature traces for the particles ignited by the laser show some variation while the emission signal reaches its peak value; no clear temperature rise or temperature decay can be distinguished when the emission signals become weak. The temperatures shown in Figure 5.8 are based on using all 32 channels of the multichannel PMT covering the entire spectral range of 373.4-641.0 nm. Considering that characteristic AlO emission lines fall within this range, the temperatures were also measured considering only five or more channels corresponding to the longest wavelengths. The result was nearly independent on the selected spectral range, while the confidence interval of the temperature became larger when fewer channels were used.

For all ESD-ignited powders, the temperature traces started with very high values and consistently showed decay, as illustrated in Figure 5.8. The temperatures had decreased substantially by the time the emission reached its peak for all materials. From Figure 5.8, it appears that the flame temperatures are close to each other, in particular when the emission signals are strong for both ESD and laser-ignited powders. This characteristic temperature profile may suggest heating to higher initial temperatures by the ESD. However, the highest reaction rate near the emission maximum then occurs at a temperature comparable to what is observed in the laser ignition case.

Average temperatures were calculated for both ESD- and laser-ignited powders for all Al-based thermites considering all the temperatures measured while the emission signal was above 50% of its peak value. These temperatures are shown in Table 5.3. In addition, adiabatic flame temperatures are shown for each material; the values are taken from [5] and calculated using NASA CEA code [108]. Considering significant error bars, the average experimental combustion temperatures are close to each other for the powders ignited by ESD and laser for all Al-based thermites. It is interesting that all experimental temperatures, except for the average value for the ESD-ignited powder with MoO_3 as an oxidizer, exceed the calculated adiabatic flame temperature. Because the effect of wavelength on spectral emissivity was unknown and thus neglected, the experimental temperatures need to be treated with caution.

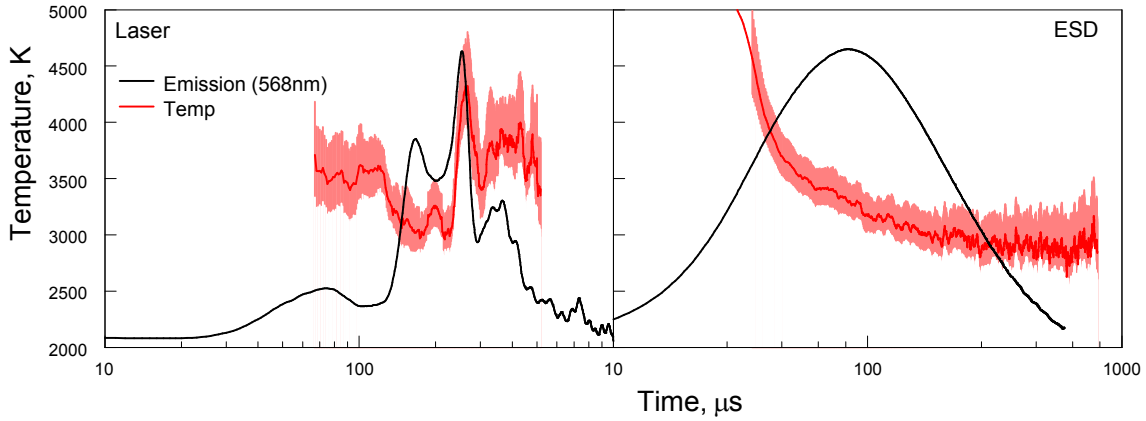

Figure 5.8 Individual emission traces (black) and corresponding time-dependent temperatures for $2Al{\cdot}MoO_3$ thermite particle ignited by the laser (left) and for the same thermite powder ignited by ESD (right).

Table 5.3 Flame Temperatures for Al-based Nanocomposite Thermites

Fuel	Oxidizer	Calculated adiabatic flame temperature (K)		Experimental flame temperature (K)	
		Using CEA code [108]	From [152]	ESD	Laser
Al	WO_3	3890	3253	4430 ± 730	3810 ± 730
	MoO_3	3809	3253	3300 ± 290	4010 ± 450
	CuO	2834	2843	3650 ± 160	3620 ± 460
	Fe_2O_3	3132	3135	3860 ± 140	4110 ± 250
	Bi_2O_3	-	3253	4870 ± 220	4040 ± 230

5.6 Discussion

Although the main objective of this experimental effort was comparison of burn rates for the same thermite particles ignited by different heat sources, it is first interesting to consider the results presented in Figure 5.4 and Table 5.2, which characterize the burn rates of individual thermite particles as a function of their sizes. These results are for the laser-ignited particles, which are expected to lose their nanostructure immediately

following their ignition due to melting of aluminum and zirconium. Therefore, the observed burn time correlations should be comparable to those measured for similarly sized particles of pure aluminum and zirconium, for each type of thermite, respectively. Indeed, it is observed that the burn times of pure Al and Zr particles vary in the same ranges as for their respective thermites. The oxide nano-inclusions, present in the thermite particles, are expected to coalesce into much coarser micron-sized domains. The effect of the condensed phase oxide would be two-fold: they would provide a source of oxygen for a limited remaining interface with molten Al or Zr, and they would effectively increase the particle size. To compare the burn times of the present thermite particles with the respective pure metals, the size of the thermite particles needs to be corrected to account for the presence of the condensed oxidizer. For different prepared thermites, the oxidizer volume fraction varied in the range of approximately 60 – 70 %; thus the effective particle diameters accounting for the metal only should be reduced by about 17 – 19%. With this in mind, data in Figure 5.4 show that the laser ignited thermite particles burn consistently longer than the pure metal particles. Qualitatively, this effect can be associated with the reduced specific surface of the reactive metal (Al, Zr) that is exposed to air because a fraction of the particle surface remains in contact with the condensed phase oxide. This suggests that the reaction with gaseous oxidizer, and not the thermite reaction, defines the burn rate of the laser-ignited thermite particles. This is not unexpected, considering that their fine structure is lost when the reactive metals melt.

Because for Zr-based thermites, combustion of particles directly ignited by ESD led to a delayed ignition of additional particles, it became impossible to quantify the burn times only for the particles that were rapidly heated by ESD directly. Therefore, direct

comparisons of burn rates of particles ignited by laser and ESD are only possible for the Al-based thermites. Results presented in Figure 5.6 show that the ESD-ignited particles of all Al-based thermites burn much faster than when they are ignited by laser. This supports the idea that the combustion mechanism of these materials can be altered by the way they are ignited. The differences in the combustion mechanisms can be understood considering characteristic times of particle heating to ignition by both laser and ESD. The characteristic times of heating are approximately 100 and 1 μs for laser and ESD, respectively. These times can be compared with characteristic times of heat propagation through the particle,τ_T and the time estimated for molten aluminum to form a droplet (Rayleigh time scale) τ_σ. These times can be estimated as

$$\tau_T = d^2/\kappa \tag{5.1}$$

$$\tau_\sigma = \sqrt{\frac{d^3\rho}{\sigma}} \tag{5.2}$$

where d is particle diameter, κ is aluminum thermal diffusivity, ρ is aluminum density, and σ is the surface tension of molten aluminum. Assuming a particle diameter of d=10 μm, and the aluminum thermal diffusivity, $3.5\cdot10^{-5}$ m^2/s $<\kappa<$ $6.9\cdot10^{-5}$ m^2/s, is taken respectively just above and below its melting point, one obtains 1.5 μs $< \tau_T <$ 2.9 μs [153]. The actual values of τ_T will be longer, accounting for a lower thermal diffusivity of oxide inclusions and Al_2O_3 layers forming as the thermite reaction starts. Taking

values of σ for molten Al varying in the range of 0.62 – 0.92 N/m [154], it is obtained that 1.7 μs $< \tau_\sigma <$ 2.0 μs. The actual values of τ_σ are even greater when viscous effects are accounted for. These estimates show that thermal gradients will be negligible in particles heated by laser; however, they are expected to be significant for particles heated by ESD. The time required to form a molten droplet is comparable to or longer than the time of ESD heating, suggesting that the composite particle retains its structure even when the melting has locally started. Conversely, in a laser-heated particle, the molten aluminum will coalesce into a droplet on a time scale much shorter than the particle heating time. Therefore, the reaction rate will be controlled by the initial composite structure in a laser-heated particle up to the instant when its temperature approaches the aluminum melting point. At this instant, the highest reaction rate defined by the particle structure will occur. The rates of reaction in composite particles heated by ESD and laser and approaching the melting point of aluminum can be estimated considering the reaction kinetics developed for an Al·Cu nanothermite [65]. This reaction is limited by diffusion of reactants through a growing Al_2O_3 layer; it accelerates with temperature but decreases when the Al_2O_3 layer grows thicker. Here, the reaction kinetics was applied to composites heated linearly at rates representing laser (10^6 K/s) and ESD (10^9 K/s) initiation. The results are shown in Figure 5.9. As the heated particles reach the Al melting point, the thickness of the oxide grown in the laser-heated particle has increased by more than 0.5 nm, while the oxide in the ESD-heated particle has only grown by about 0.12 nm.

This difference in the oxide thickness leads to a great difference in the predicted reaction rate at the aluminum melting point by near three orders of magnitude. Thus, the

ESD-heated particle, retaining its structure when heated to about the aluminum melting point, reacts nearly 1000 times faster than the same particle heated by the laser to the same temperature. Interestingly, a significant difference in the reaction rate remains even accounting for a temperature gradient in the ESD-heated particle, e.g., taking the aluminum-oxide interface at temperatures significantly lower than the Al melting point (by as much as 200 K, see Figure 5.9). Thus, a laser-heated particle reaching the Al melting point loses its structure, which leads to its further reaction being controlled by the surface of the formed bulk aluminum droplet. However, a much faster reaction in the ESD-heated particle sustains temperature gradients and leads to a significantly greater extent of reaction expected before the molten aluminum has time to coalesce into a coarser droplet.

Note that the higher burn rates observed for the ESD-ignited particles would be expected to also lead to greater flame temperatures, which are not observed here. At the same time, the measured temperatures in both cases are close to or even higher than the adiabatic flame temperature. Although, as noted above, the temperature measurements should be treated with caution, it is clear that heat losses, in particular, by radiation, are very high for such high temperature processes. Similar to temperature measurements, the radiative heat losses are affected by emissivity and by surface structure of the radiating particles, which could be quite different for the particles combusting following different mechanisms. For example, emissivity of a smooth molten metal surface may be lower than that of a solid with textured surface and defects, leading to lower radiative heat losses from molten particles. Further studies would be necessary to substantiate such hypotheses, however.

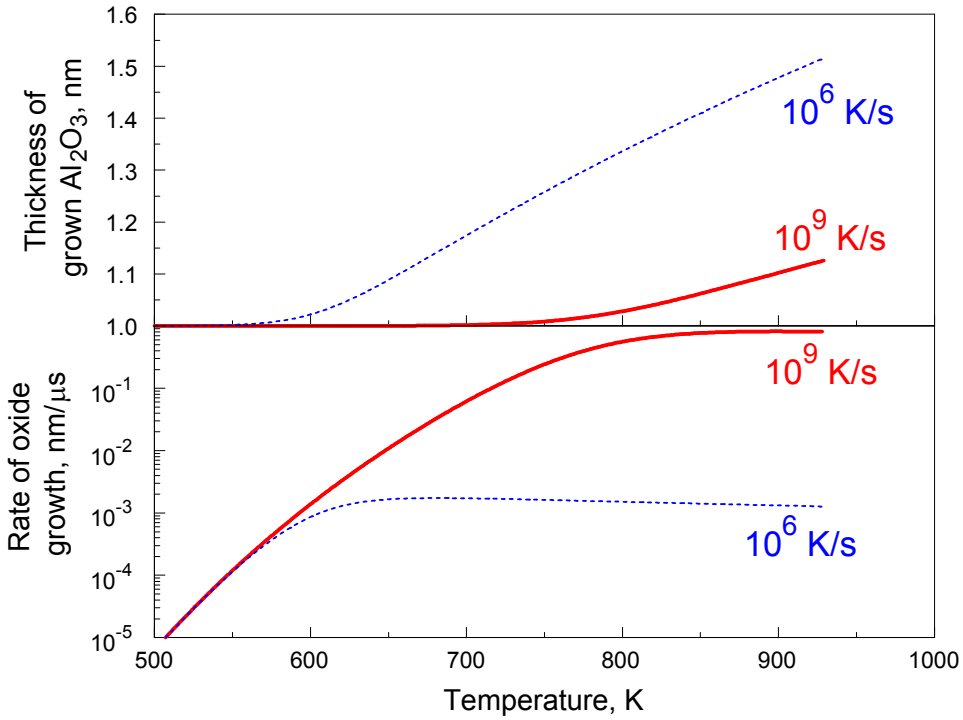

Figure 5.9 Thickness of the grown alumina layer and the rate of the alumina layer growth estimated as a function of temperature in a nanocomposite Al·Cu thermite particle heated at different rates accounting for the reaction kinetics reported elsewhere.
Source: [65].

5.7 Conclusions

Individual particles of Al-based thermites could be ignited by both laser and ESD so that the direct comparisons of their combustion characteristics became possible. For Zr-based thermites, ESD initiation generated burning particle clouds including both particles directly heated by ESD and particles ignited later and thus heated at distinctly lower rates. This prevented direct comparisons of the burn times for the laser and ESD-ignited Zr-based thermite particles.

For both, Al and Zr-based thermites, laser heated particles burned at rates slightly lower than those observed for particles of comparable sizes for pure Al and Zr,

respectively. Similar, relatively low burn rates were observed for the Zr-based thermite powders in the ESD experiments, in which the burn times were dominated by the powder clouds, ignited with a substantial delays and comprising particles heated much slower than those heated directly by ESD.

For Al-based thermites, burn times of particles heated by ESD were substantially shorter than those observed for the same, laser-heated particles; the effect was observed for all oxidizers used here. Thus, it is confirmed experimentally that the burn rates of nanocomposite thermites prepared by arrested reactive milling can be controlled by the way they are ignited. The differences in the combustion mechanisms of the particles heated by laser and ESD were interpreted considering characteristic times required for the heat propagation through the particle, formation of a molten droplet of aluminum, and the rates of reaction in nanocomposite thermites heated up to the aluminum melting point by laser and ESD. It was observed that the laser-heated particles do not have noticeable thermal gradients; conversely, strong temperature gradients are expected in the ESD-heated particles. The highest reaction rate unaffected by Al melting and thus by loss of the original reaction interface area, was estimated for an Al·CuO thermite heated up to the Al melting point at the heating rates representing both ESD and laser ignition experiments and taking into account a previously determined reaction kinetics. The estimate shows that near the Al melting point, the reaction rate in an ESD-heated particle is nearly 1000 times higher than in the same particle heated by laser. This effect is chiefly due to the difference in the thickness of the Al_2O_3 film grown between Al and oxidizer during heating at respectively different rates. Considering that coalescence of the molten Al into a droplet takes a few μs, which could be further delayed for the ESD-

heated particles by the temperature gradients, it is concluded that the redox reaction in the ESD-heated particles will proceed to a much greater extent than in the same particles heated by laser before the nanocomposite structure is lost due to Al melting. This explains a significant difference in the observed burn rates for the particles of the same nanocomposite thermites heated at different rates.

CHAPTER 6

COMBUSTION OF A RAPIDLY INITIATED FULLY DENSE NANOCOMPOSITE AL-CUO THERMITE POWDER

6.1 Abstract

Very short burn times of nanocomposite, fully dense, stoichiometric 2Al·3CuO thermite particles ignited by electro-static discharge (ESD) observed in earlier experiments are interpreted assuming that the reaction occurs heterogeneously at the Al-CuO interfaces while the initial nanostructure is preserved even after the melting points of various phases present in the particle are exceeded. The heating rate for the ESD ignited particles is very high, reaching 10^9 K/s. The reaction model assumes that the rate of reaction is limited by transport of the reacting species across the growing layer of Al_2O_3 separating Al and CuO. The model includes the redox reaction steps considered earlier to describe ignition of 2Al·3CuO nanocomposite thermites and adds steps expected at higher temperatures, when further polymorphic phase changes may occur in Al_2O_3. A realistic distribution of CuO inclusion sizes in the Al matrix is obtained from electron microscopy and used in the model. The model accounts for heat transfer of the nanocomposite particles with surrounding gas and radiative heat losses. It predicts reasonably well the burn times observed for such particles in experiments. It is also found that neglecting polymorphic phase changes in the growing Al_2O_3 layer and treating it as a single phase with the diffusion limited growth rate similar to that of transition aluminas (activation energy of ca. 250 kJ/mol) still leads to adequately predicted combustion temperatures and times for

the nanocomposite particles rapidly heated by ESD. The model highlights the importance of preparing powders with fine CuO inclusion sizes in the nanocomposite particles necessary to complete the redox reaction; it is also found that the particle combustion temperatures may vary widely depending on their dimensions. Higher combustion temperatures generally lead to greater reaction rates and, respectively, to the more complete combustion.

6.2 Nomenclature

C_p	J g^{-1} K^{-1}, specific heat of the particle
C_α	kg m^{-1} s^{-1}, pre-exponent for thermally activated diffusion term describing the oxidative growth of α-Al_2O_3
D	m, particle diameter
E_α	kJ mol^{-1}, activation energy for thermally activated diffusion term describing the oxidative growth of α-Al_2O_3
$E_{\gamma\to\alpha}$	kJ mol^{-1}, activation energy for the γ-Al_2O_3 to α-Al_2O_3 polymorphic phase transformation
$F_{\gamma\to\alpha}$	M s^{-1} K^{-1}, pre-exponent for the γ-Al_2O_3 to α-Al_2O_3 polymorphic phase transformation
f_x	progress function for growth of by α-Al_2O_3 diffusion
h_α	nm, thickness of α-Al_2O_3 layer
h_α^{min}	nm, minimum thickness of alpha layer in order to contribute to real diffusion resistance
h_γ	nm, thickness of γ-Al_2O_3 layer
h_γ^{min}	nm, minimum thickness of gamma layer in order to contribute to real diffusion resistance
k_B	J K^{-1}, Boltzmann constant
$K_{\gamma\to\alpha}$	J mol^{-1} m^{-1}, exponential coefficient used to describe the γ-Al_2O_3 to α-Al_2O_3 polymorphic phase transformation
m_{am}^{CM}	kg, mass of amorphous Al_2O_3 formed due to Cabrera-Mott reaction
m_{am}^{Diff}	kg, mass of amorphous Al_2O_3 formed due to oxidation by diffusion
m_{core}	kg, mass of the inclusion core
m_g	kg, mass of gas molecule (air)
m_p	kg, mass of the particle
m_α^{Diff}	kg, mass of α-Al_2O_3 formed due to oxidation by diffusion
$m_{\gamma\to\alpha}^{tr}$	kg, mass of α-Al_2O_3 formed due to polymorphic phase transformation

m_{γ}^{Diff}	kg, mass of γ-Al_2O_3 formed due to oxidation by diffusion
P_g	Ambient gas pressure
Q_{chem}	J, chemical heat term
Q_{conv}	J, convective heat term
Q_{ESD}	J, heat introduced to the particle from electrostatic discharge
Q_{rad}	J, radiative heat term
R	J mol^{-1} K^{-1}, universal gas constant
r_{core}	nm, radius of the core
r_{α}	nm, radius of γ-Al_2O_3 layer
r_{γ}	nm, radius of α-Al_2O_3 layer
T	K, temperature of the particle
T_s	K, temperature of the surroundings taken as 298 K
ΔT	K, temperature change during a computational time step
T_{δ}	K, temperature of the gas at the Langmuir layer
$v_{\gamma\rightarrow\alpha}$	m s^{-1}, γ-Al_2O_3 to α-Al_2O_3 transformation velocity
X_i	number of inclusions in a size bin *i*
x	global reaction progress, varied from 0 to 1
x_{α}	reaction progress for growth of α-Al_2O_3 by diffusion
x_{α}^{*}	reaction progress at the onset of α-Al_2O_3 growth
α_c	Accommodation coefficient
$\Delta H_{Al_2O_3}$	J g^{-1}, enthalpy of formation per mass of alumina
γ^{*}	adiabatic index of air (ambient gas)
ε	particle emissivity
σ_{SB}	W m^{-2} K^{-4}, Stefan-Boltzmann constant
ρ_{α}	kg m^{-3}, density of α-Al_2O_3

6.3 Introduction

Thermites comprising mixed powders of a metal fuel, such as aluminum and a metal oxide oxidizer, e.g., oxide of iron, copper, molybdenum, etc., have high reaction enthalpies, but the heat release occurs relatively slowly, limiting their applications to welding [128, 155, 156] and a rather narrow area of custom heat sources [136]. Efforts have been made to increase their reaction rates by increasing their reactive interface area, mostly by using nano-sized mixed metal fuel and oxidizer particles and by preparing fully-dense nanocomposite structures [17, 19, 132, 157]. The rates of combustion for

such nanocomposite thermites increased substantially extending their potential applications to explosives [95], pyrotechnics [158], and propellants [135]. The reaction is accelerated mostly due to reduced ignition delays and/or lower temperatures at which the thermal runaway leading to high-temperature combustion occurs. It was reported, however, that the nano-particle based materials rapidly sinter upon heating, losing their original nanostructure [68, 139]. The sintering creates larger particles forming upon ignition of a nanothermite, in which fuel and oxidizer are no longer mixed on the nanoscale, resulting in respectively long particle burn times [159]. Similarly, burn times measured for a number of fully-dense nanocomposite aluminum-based reactive material powders with micron-sized particles ignited by passing through a CO_2 laser beam were found to be comparatively longer than for the pure aluminum particles with the same dimensions [160]. The latter result was also explained by the loss of particle nanostructure immediately after ignition, when the metal fuel melts.

More recently, it was observed, somewhat unexpectedly, that the same fully-dense nanocomposite thermites burned faster when ignited by heating at very high rates (10^9K/s) [90, 140]. Such high heating rates were achieved by igniting small batches of nanocomposite thermite powders by electrostatic discharge (ESD). When the same thermites were ignited by passing through a CO_2 laser beam, the heating rate was estimated to be close to 10^6 K/s [160, 161]. The burn times of ESD-ignited micron-sized particles with fuel and oxidizer mixed on the nanoscale were almost an order of magnitude shorter than for the same particles ignited by the laser beam. This trend was observed for a number of aluminum-based thermites. It was hypothesized that the nano-structure in such rapidly heated particles can be preserved while their temperatures grow

above the melting point of metal fuel [157, 161]. This can occur if the time of heating is shorter or comparable to the time required for the melt to form. If the nanostructure is preserved, the reaction at high temperatures will continue heterogeneously at the interfaces between the fuel and oxidizer. The rate of this reaction is expected to be very high because of the remaining high interface area, high temperatures, and thin product layer forming between finely mixed fuel and oxidizer. The objective of this work is to determine whether a heterogeneous reaction model can, indeed, reasonably describe the very high burn rates of the fully-dense nanocomposite thermite particles heated by ESD. The model is formulated and its sensitivity to various material characteristics is explored. Simplifying assumptions had to be made in order to enable a description based on kinetics determined for low-temperature solid-state reactions to be used for elevated temperatures, when components might be expected to melt or even boil. The model is applied to the composite particles with realistic dimensions and oxide inclusions with experimental size distributions. The results in terms of reaction times and extent of reaction are presented and compared to relevant experimental data.

6.4 Technical Approach

The model proposed here describes combustion through heterogeneous, condensed phase reactions at the metal-oxidizer interfaces in nanocomposite particles. It builds on an earlier developed ignition model for the fully-dense nanocomposite thermite particles prepared by Arrested Reactive Milling [52, 162]. The analysis is performed for a stoichiometric $2Al \cdot 3CuO$ thermite. A particle is assumed to have an aluminum matrix

with fine copper oxide inclusions. The dimensions of the inclusions are described using a distribution function recovered from analyses of the cross-sections of the particles prepared in respective experimental studies; details follow. Both particle and inclusions are assumed spherical. The ignition model for such particles reported earlier considered a solid state redox reaction occurring at the interfaces between Al and CuO and forming a thin Al_2O_3 film [52, 162]. The reaction rate was assumed to be controlled by transport of reactants through this growing Al_2O_3 film. The transport was affected by the film thickness and structure. For very thin films, the transport was described by the Cabrera-Mott formalism [163, 164]. As the film grew thicker, conventional diffusion equations were used instead. Polymorphic phase changes in the growing Al_2O_3 film were accounted for by altering the film thickness as a function of density for specific alumina polymorphs and by using appropriate diffusivities. The heat release from the redox reaction was combined with the heat provided by an external heating source (a laser beam or an electrically heated wire) and balanced by the convective and/or conductive heat losses from the igniting particle. The model was useful until the particle temperature reached the experimental ignition temperature when it predicted a rapid temperature increase indicative of the ignition. The growing alumina layers were assumed to be amorphous initially; they transformed into γ-Al_2O_3 at higher temperatures. Considering this reaction scenario further, at higher temperatures, resulted in formation of rather thick γ-Al_2O_3 layers, suppressing the reaction rate. Instead of further analysis of heterogeneous reactions between Al and CuO, it was assumed that the particles lost their nanostructure and continued burning as aluminum droplets exposed to an oxidizing environment, while the remaining unreduced copper oxide inclusions coalesced.

Here, the approach outlined above is extended to even higher temperatures, when γ-Al_2O_3 layers transform into α-Al_2O_3. The nanostructure of the composite particle was assumed to be preserved even after melting points of some or all components contained in the particle were exceeded. Because of the very high heating rate, all polymorphic transformations in alumina occur before its thickness increases significantly. Because α-Al_2O_3 density is substantially higher than that of γ-Al_2O_3, the second polymorphic phase change (γ-$Al_2O_3 \rightarrow \alpha$-$Al_2O_3$) may result in a loss of continuity of the alumina layer, leading to the accelerated redox reaction. Qualitatively, this accelerated oxidation is similar to that occurring when amorphous alumina transforms to γ-Al_2O_3, leading to ignition of aluminum particles in gas oxidizers [131, 165] and to thermal runaway in nanocomposite thermites heated at lower rates [162, 166]. In the present analysis, the temperature can increase substantially and exceed the melting point of alumina, while heterogeneous reaction limited by transport of reactant through the alumina layer remains the primary combustion mechanism. It is unclear how to treat the transport properties of molten alumina, especially when it is present as very thin, single nanometer layers. It is likely that thinning or a loss of continuity of the oxide layer, qualitatively similar to that expected for a γ-$Al_2O_3 \rightarrow \alpha$-$Al_2O_3$ transition would occur, however, there is presently no approach enabling one to describe it. Therefore, as an approximation, the effect of melting of alumina on its transport properties is presently ignored. Instead, the properties of crystalline alumina polymorphs are used to describe the reaction rates at all temperatures. This description is not expected to be precise; however, it should be useful in showing whether a heterogeneous reaction with a realistic rate can describe the characteristic combustion times observed experimentally for very rapidly heated

nanocomposite thermite particles. Three additional calculations were performed neglecting any phase changes in the growing Al_2O_3 layer, and describing its properties as each one of the three known solid alumina polymorphs. These calculations were meant to establish the significance of the energetically neutral phase changes in alumina on combustion of rapidly heated nanocomposite thermite particles.

6.5 Model

The particle temperature is determined as a function of time, when it is heated by ESD, cooled by convection and radiation, and undergoes the redox reaction between Al and CuO. The redox reaction yields an Al_2O_3 layer on top of each CuO inclusion inside composite particles. The inclusions are transformed directly to Cu, with their dimensions reduced as the reaction progresses to accommodate the difference in densities between CuO and Cu. The calculations were performed numerically, and all terms discussed below were calculated for each time step, Δt. The change in particle temperature was calculated as (see nomenclature for definition and dimensions of all terms):

$$\Delta T = \left(\frac{1}{C_p m_p}\right)(Q_{ESD} + Q_{chem} - Q_{conv} - Q_{rad}) \tag{6.1}$$

The terms on the right hand side of Eq. (1) represent, respectively, heat introduced into the particle from the ESD, heat release due to redox reaction, heat transfer of the

particle with the surrounding gas, and radiative heat losses from the particle. Each heat term is discussed separately below.

Melting of different components present in the reacting particle, including aluminum, copper, copper oxide, and aluminum oxide is accounted for by maintaining the particle temperature constant until the latent heat of melting at each characteristic temperature is absorbed by the particle. Similarly, evaporation of aluminum, copper, copper oxide, and aluminum oxide are accounted for in the thermal balance; however, the evaporated species are not removed from the particle volume and continue being available for the reaction. The latter simplification is made because no guidance exists for readjusting the particle structure when some of the material is removed to the vapor phase. Physically, continuing reaction between evaporated CuO and Al can be justified assuming that most of such vapors are trapped in the defects, at the phase boundaries, and in the bubbles forming inside burning particles. Thus, vaporized CuO and Al can still diffuse through the forming Al_2O_3 layer and react with each other. Scanning electron microscopy of the combustion products collected in experiments [167] suggests that most particles have dimensions similar to those of the starting nanocomposite powder particles, supporting the above approach, which effectively neglects removal of material from the burning particles.

6.5.1 Heat Introduced to the Particle from ESD

This term was obtained using previous experiments involving the ESD apparatus exploited for ignition studies [90]. The ESD energy was obtained from the measured current traces for a range of ESD voltages. The current traces gave both the duration and energy density of the ESD pulse. The imprints left by the ESD on the substrate with a

powder monolayer were imaged using scanning electron microscopy (SEM). The area of this imprint was also found as a function of the ESD voltage. For each voltage, the total energy from ESD was uniformly spread across the imprint area; then the energy absorbed by each particle located within the ESD imprint area was calculated as proportional to the particle's surface area. Thus, data illustrated for two selected voltages in Figure 6.1 were obtained. The data from Figure 6.1 were used in the following calculations for Q_{ESD} for particles of different sizes.

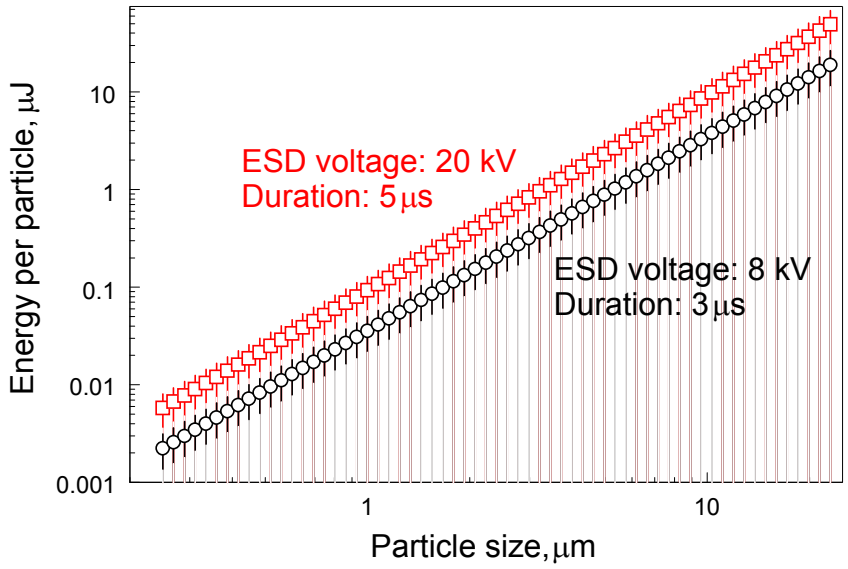

Figure 6.1 ESD heat absorbed by particles of different dimensions for discharges at 8 and 20 kV used in experiments.
Source: [90].

6.5.2 Heat Generated by Redox Reaction

This term was calculated accounting for the formation of different alumina polymorphs in the redox reaction between Al and CuO yielding Al_2O_3 and Cu. The reaction was considered for CuO inclusions of different sizes present inside each, fully dense composite particle. For each particle, the term Q_{chem} was obtained as:

$$Q_{chem} = \Delta H_{Al_2O_3} \sum_{i=1}^{n} X_i \left(\frac{dm_{am}}{dt} + \frac{dm_{\gamma}}{dt} + \frac{dm_{\alpha}}{dt} \right)_i dt \quad (6.1)$$

where $\Delta H_{Al_2O_3}$ is the specific heat of redox reaction yielding Al_2O_3, n stands for the number of size bins for the inclusion distribution and the X_i stands for the number of inclusions of that specific size i (this distribution was obtained experimentally as clarified below). The reaction is quantified through three individual rates for growth of three polymorphs of alumina. As in the ignition model [52, 162], each polymorph can grow either via direct oxidation or via a phase transformation from another polymorph. Thus, each individual *dm/dt* term can be either positive (redox reaction or formation of a new phase) or negative (when a previously grown alumina polymorph transforms into a new structure). Two main changes compared to the previous ignition model [162] are made. First, as noted above, formation of α-Al_2O_3 is included in addition to the formation of γ-Al_2O_3. Second, the size distribution of CuO inclusions are accounted for quantitatively; previously, the analysis was performed for only one selected inclusion size.

The details describing formation of amorphous and gamma alumina can be found in the ignition model [162]. However, in addition to formation of γ-Al_2O_3 by direct oxidation and by transformation from amorphous alumina, its destruction due to formation of α-Al_2O_3 was also accounted for:

$$\frac{dm_{\gamma}}{dt} = \frac{dm_{\mathrm{am}\rightarrow\gamma}^{tr}}{dt} + \frac{dm_{\gamma}^{Diff}}{dt} - \frac{dm_{\gamma\rightarrow\alpha}^{tr}}{dt} \tag{6.2}$$

The formalism describing formation of α-Al_2O_3 is similar to that used in Ref. [162] for the growth of γ-Al_2O_3:

$$\frac{dm_{\alpha}}{dt} = \frac{dm_{\alpha}^{Diff}}{dt} + \frac{dm_{\gamma\rightarrow\alpha}}{dt} \tag{6.3}$$

$$\frac{dm_{\alpha}^{Diff}}{dt} = f_{\mathrm{x}} C_{\alpha} exp\left(-\frac{E_{\alpha}}{RT}\right)\left(\frac{1}{r_{core} + h_{\gamma}} - \frac{1}{r_{\alpha}}\right)^{-1} \tag{6.4}$$

$$\frac{dm_{\gamma\rightarrow\alpha}}{dt} = 4\pi\rho_{\alpha} r_{\alpha}^2 v_{\gamma\rightarrow\alpha} \tag{6.5}$$

The velocity, $v_{\gamma\rightarrow\alpha}$, with which the transformation front radially propagates through the alumina layer is dependent on both temperature and the thickness of the γ-Al_2O_3 layer and, following previous work [162, 165] is given as:

$$v_{\gamma\to\alpha} = F_{\gamma\to\alpha}T\left[1 - exp\left(-\frac{K_{\gamma\to\alpha}h_{\gamma}}{RT}\right)\right]exp\left(-\frac{E_{\gamma\to\alpha}h_{\gamma}}{RT}\right) \quad (6.6)$$

The global reaction progress is x, and progress function f_x is:

$$f_{\mathrm{x}} = 1 - x - x_{\alpha}^{*} \quad (6.7)$$

where x^* is the reaction progress before the onset of the phase change.

As in the earlier ignition model, for each specific time step, diffusivity for only one alumina polymorph is accounted for; it is taken for the polymorph with the lowest diffusivity. The growth or destruction of each alumina polymorph is accounted for while its thickness is greater than a minimum thickness, h_{min} defined for each polymorph separately. In the previous work, this minimum thickness was evaluated based on oxidation experiments of pure aluminum particles in gaseous oxidizers [162]. Here, it was re-evaluated for the heterogeneous reactions of aluminum with copper oxide as presented in Table 6.1 along with other model parameters.

As in the ignition model, the total mass change of each CuO inclusion (being reduced to Cu) is calculated accounting for the reaction stoichiometry and formation of all three alumina polymorphs by direct oxidation, where the growth of the amorphous oxide can be limited by the rate of either Cabrera-Mott or conventional diffusion:

$$\frac{dm_{\text{core}}}{dt} = -z\left(\frac{dm_{\text{am}}^{CM}}{dt} + \frac{dm_{\text{am}}^{Diff}}{dt} + \frac{dm_{\gamma}^{Diff}}{dt} + \frac{dm_{\alpha}^{Diff}}{dt}\right) \tag{6.8}$$

The mass equations for aluminum, amorphous and γ-alumina phases remain the same as the ignition model [162], [168] while an additional mass balance for α-alumina layer is included:

$$\frac{4}{3}\pi\left(r_{\alpha}^{3} - r_{\gamma}^{3}\right)\rho_{\alpha} = m_{\alpha} \tag{6.9}$$

Table 6.1 Model Parameters (Continued)

Parameter	Description	Value
b	Coefficient used in linear function of E_2	5.52 x 10^{-22} J-nm K^{-1}
c_{am}	Coefficient for reaction progress for growth of amorphous Al2O3	5
c_{α}	Coefficient for reaction progress for growth of α-Al2O3	1
c_{γ}	Coefficient for reaction progress for growth of γ-Al2O3	8
C_{am}	Pre-exponent of amorphous oxidation by diffusion	5.098 x 10^{-8} kg m^{-1} s^{-1}
C_{α}	Pre-exponent of alpha oxidation by diffusion	2.3791 x 10^{-2} kg m^{-1} s^{-1}
C_{γ}	Pre-exponent of gamma oxidation by diffusion	4.0784 x 10^{-3} kg m^{-1} s^{-1}
E_1	Activation energy used in Cabrera-Mott equation	44.5 kJ mol-^{1}
E_{am}	Activation energy for diffusion-limited growth of amorphous oxide	105 kJ mol^{-1}
Eα	Activation energy for diffusion-limited growth of alpha oxide	252 kJ mol^{-1}
E_{γ}	Activation energy for diffusion-limited growth of gamma oxide	210 kJ mol^{-1}
$E_{am\rightarrow\gamma}$	Activation energy for amorphous to gamma transformation	458 kJ mol^{-1}
$E_{\gamma\rightarrow\alpha}$	Activation energy for gamma to alpha transformation	409 kJ mol^{-1}
$F_{am\rightarrow\gamma}$	Pre-exponent for gamma transformation equation	2 x 10^{15} m s^{-1} K^{-1}
$F_{\gamma\rightarrow\alpha}$	Pre-exponent for alpha transformation equation	5 x 10^{6} m s^{-1} K^{-1}
h_0	Initial thickness of amorphous layer	0.8 nm

Table 6.1 (Continued) Model Parameters

Parameter	Description	Value
h_{α}^{min}	Minimum thickness of alpha layer in order to contribute to real diffusion resistance	1.5 nm
h_{γ}^{min}	Minimum thickness of gamma layer in order to contribute to real diffusion resistance	1 nm
k	Thermal conductivity of air at 298K	0.0255 J s^{-1} m^{-1} K^{-1}
kb	Boltzmann constant	1.3806488 x 10^{-23} J K^{-1}
$K_{am\rightarrow\gamma}$	Exponential coefficient in gamma transformation equation	1 x 10^{12} J mol^{-1} m^{-1}
$K_{\gamma\rightarrow\alpha}$	Exponential coefficient in alpha transformation equation	1 x 10^{8} J mol^{-1} m^{-1}
mAl	Percent mass of Aluminum	0.1844
mCuO	Percent mass of Copper Oxide	0.8156
Partvel	Particle velocity	100 m s-1
Pg	Ambient gas pressure	101325 Pa
Pr	Prandtl number for air at 298K	0.7296
Ts	Surrounding Temperature	298K
αc	Accommodation Coefficient	0.92
$\Delta H_{fusion}Al$	Latent Heat of fusion for pure aluminum	398000 J kg^{-1}
$\Delta H_{fusion}Al2O3$	Latent Heat of fusion for pure alumina	990000 J kg^{-1}
$\Delta H_{fusion}Cu$	Latent Heat of fusion for pure copper	205000 J kg^{-1}
$\Delta H_{fusion}CuO$	Latent Heat of fusion for pure copper oxide	148000 J kg^{-1}
$\Delta H_{vap}Al$	Latent Heat of Vaporization of aluminum	11400000 J kg^{-1}
$\Delta H_{vap}Al2O3$	Latent Heat of Vaporization of 99.9% alumina	19380000 J kg^{-1}
$\Delta H_{vap}Cu$	Latent Heat of Vaporization of Copper	5069000 J kg^{-1}
$\Delta H_{vap}CuO$	Latent Heat of Vpaorization of Copper Oxide	880000 J kg^{-1}
ε	Particle emissivity	1
μ_s	Surface viscosity	1.98 x 10-5 kg m^{-1} s^{-1}
μ_∞	Fluid viscosity of air	1.82 x 10-5 kg m^{-1} s^{-1}
ρ_α	Density of alpha alumina solid	3970 kg m^{-3}
$\rho_{\alpha l}$	Density of alpha alumina liquid	2930 kg m^{-3}
ρ_γ	Density of gamma alumina solid	3650 kg m^{-3}
ρ_{amorph}	Density of amorphous alumina solid	3050 kg m^{-3}
$\rho_{Cu(s)}$	Density of Copper solid	8920 kg m^{-3}
$\rho_{Cu(l)}$	Density of Copper liquid	8020 kg m^{-3}
$\rho_{Al(s)}$	Density of Aluminum solid	2700 kg m^{-3}
$\rho_{Al(l)}$	Density of Aluminum liquid	2375 kg m^{-3}
$\rho_{CuO(s)}$	Density of Copper Oxide solid	6310 kg m^{-3}
σ_{SB}	Stefan-Boltzmann constant	5.67773 x 10^{-8} W m^{-2} K^{-4}

Source: [165, 169, 170].

6.5.3 Convective Heat

Heat exchange with the surrounding gas in the transition regime was calculated considering that the particle size may be comparable to the mean free path of the gas molecule. Following the previous work [168], Langmuir layer around the particle was introduced. The temperature and radius of this layer are T_δ and r_δ, respectively. The heat was removed from outside of the Langmuir layer by forced convection.

$$Q_{conv} = h(4\pi r_\delta^2)(T_\delta - T_s) \tag{6.10}$$

where the convective heat transfer coefficient for the forced convection for a burning particle ejected by the spark was described as:

$$h = \left(\frac{k}{D}\right)\left(2 + \left[0.4Re^{\frac{1}{2}} + 0.06Re^{\frac{2}{3}}\right]Pr^{0.4}\left(\frac{\mu_\infty}{\mu_s}\right)^{\frac{1}{4}}\right) \tag{6.11}$$

The Reynolds number, *Re*, was calculated considering that the velocity of the particles ejected by the spark is 100 m/s [90]. The heat exchange within the Langmuir layer was calculated in the free molecular regime as:

$$Q_{conv} = \alpha_c \pi D^2 P_g \sqrt{\frac{k_B T_\delta}{8\pi m_g}} \frac{\gamma^* + 1}{\gamma^* - 1} \left(\frac{T_p}{T_\delta} - 1 \right) \tag{6.12}$$

Solving Equations (6.10) and (6.12) along with respective boundary conditions enables us to determine T_δ , r_δ, and also Q_{conv}. Further details can be found in the literature [168, 171, 172].

6.5.4 Radiation Heat

The radiation term was estimated as:

$$Q_{rad} = \varepsilon \sigma_{SB} (\pi D^2)(T^4 - T_s^4) \tag{6.13}$$

where D is the composite particle diameter and the emissivity, ε, was assumed to be equal to 1.

6.5.5 Size Distributions for Composite Particles and for Oxidizer Inclusions

The inclusion sizes within composite particles were determined using SEM images of cross-sectioned particles taken using backscattered electrons. An example of a representative image is shown in Figure 6.2. Brighter areas represent CuO inclusions and darker area represent Al. Automated particle recognition algorithm were difficult to use because of varied overall brightness level across the image. An alternative method was therefore used. Imaging software (ImageJ) was employed. For each image, a grid of horizontal and vertical lines was randomly placed within a particle. One such line is

shown in Figure 6.2. The brightness level along each line was quantified, as also illustrated in Figure 6.2. Each peak in the brightness was interpreted as an inclusion as long as it passed a prominence filter. The prominence filter takes the largest peak and assigns it a maximum value. It further compares all other peaks to it, removing those, which are below a selected threshold value. The threshold was selected to avoid small brightness changes, which could not be unambiguously assigned to a particle while inspecting the image visually. The size of inclusion was taken as the distance between the maximum and minimum brightness gradients for each peak. In Figure 6.2, location of these maxima and minima is represented by filled and open symbols, respectively. Because the cross-section can be at a random plane for each inclusion, the measured average inclusion dimensions do not represent the inclusion diameters. An average length of a randomly taken cross-section for a sphere is $\frac{\pi}{4}D$, where D is the sphere diameter. Respectively, the measured average inclusion dimensions were multiplied by $\frac{4}{\pi}$.

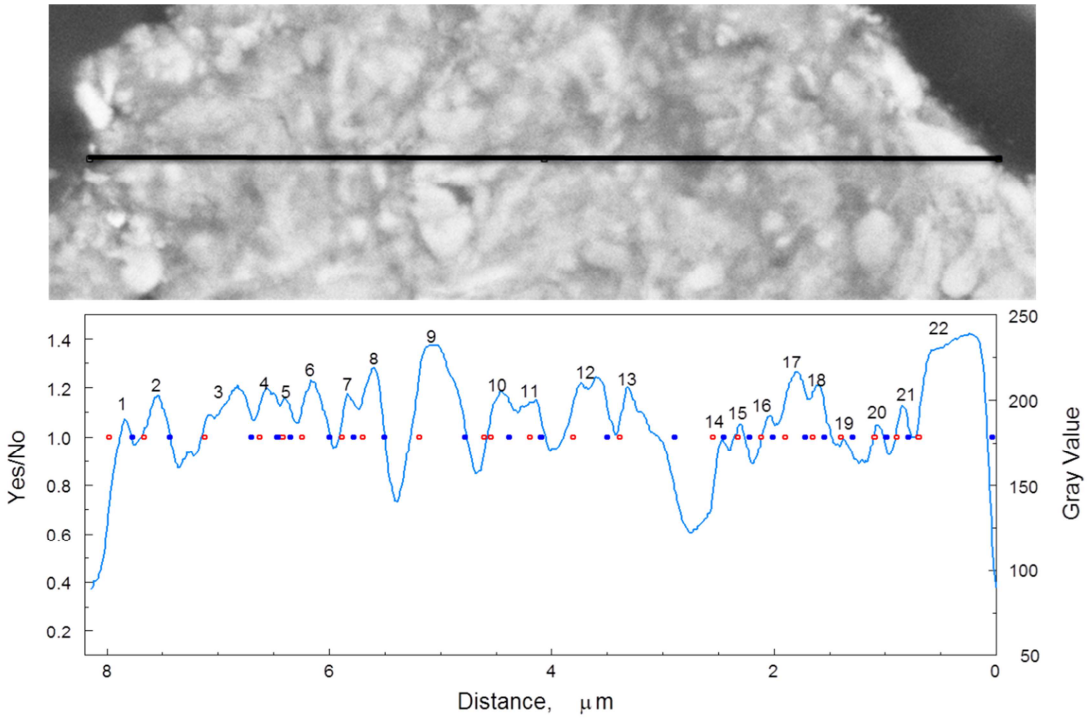

Figure 6.2 An example of an SEM image of a composite particle cross-section and a grid line (top), along which the brightness values are obtained (bottom) to determine inclusion dimensions. Filled circles show maxima and open circles show minima for the brightness vs. distance plot.

This method of inclusion sizing was applied across the entire size distribution of particle sizes, to ensure no size biasing was applied to the inclusion distribution. The sizing results led to the inclusion distribution seen in Figure 6.3. The average inclusion size obtained from the distribution is 0.23 μm or 230 nm.

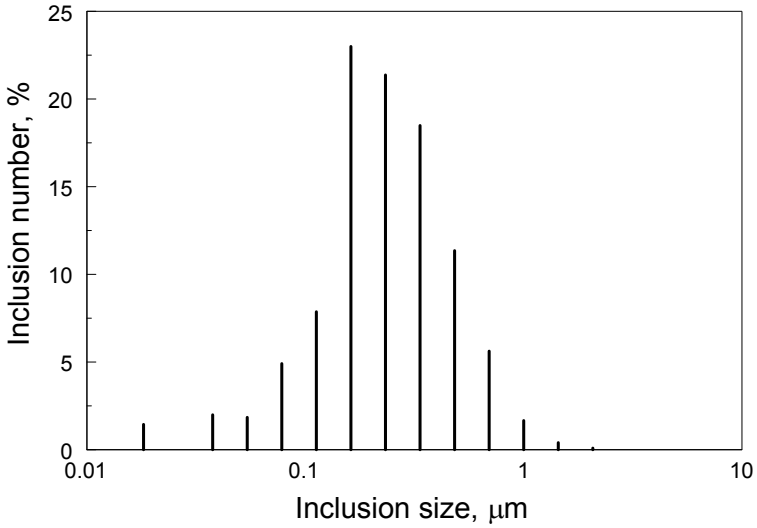

Figure 6.3 Size distribution of CuO inclusions in the prepared composite particles.

Particle sizes in the experimental study [161] were determined using SEM imaging and a particle distribution shown in Figure 6.4 was obtained using those images. For calculations, the distribution was approximated by a lognormal function, also shown in Figure 6.4, with the average particle size of ~ 2 μm. The smooth function was represented as a set of nine individual size bins with particle sizes from 1 to 15 μm, as further discussed when the results are presented.

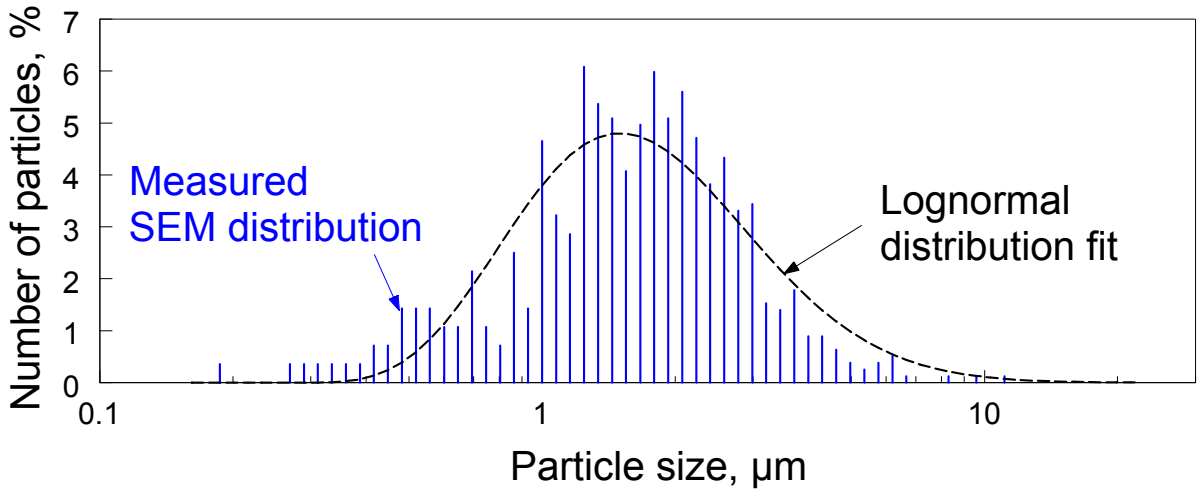

Figure 6.4 Particle size distribution of the prepared nanocomposite powder obtained by processing SEM images and the corresponding lognormal function.
Source: [161].

6.6 Results and Discussion

6.6.1 Activation Energy for Diffusion through Growing Alumina Layer

Preliminary calculations used the same activation energies and pre-exponents characterizing diffusion through different alumina polymorphs as determined in earlier work [162, 165, 169], aimed to describe ignition of pure aluminum or aluminum-based composite particles. In these calculations, it was observed that particles quenched (their temperatures decreased) immediately after the end of the ESD pulse. In a second set of calculations, the activation energy for diffusion through α-Al_2O_3 was adjusted. Thus, the reactions involving amorphous and γ-Al_2O_3 leading to ignition and used in the previously developed ignition model remain unaffected. The change in the activation energy for diffusion-limited growth of α-Al_2O_3 only affects later stages of reaction, which were not important for previous analyses. In earlier experiments, the activation energy for diffusion-limited growth of α-Al_2O_3 was found to be 252 kJ/mol for particles of 3-5 μm

diameter and 306 kJ/mol for coarser, 10-14 μm particles [165]. The latter value was used previously and in the first set of preliminary calculations. For the second set of calculations, the activation energy of 252 kJ/mol was used instead; in this case, particles were observed to continue self-heating after the spark pulse was completed. This reduced activation energy was used in the rest of the calculations. Along with other model parameters, it is included in Table 6.1.

6.6.2 Reaction Governed by Growth of a Single Alumina Phase

In the following calculation, the complete model was compared to an abridged version where no alumina polymorphic phase changes were included. Instead, alumina was described as a single phase throughout the entire temperature range. These calculations were aimed to test whether it is critical to account for the polymorphic phase changes in the growing Al_2O_3 layer for the reactions occurring after ignition and proceeding at relatively high temperatures. This is particularly relevant considering that the temperatures can often exceed the melting point of Al_2O_3. In the latter case, the molten alumina will still serve to separate reacting phases. Its properties are expected to be somewhat different from those of any crystalline polymorphs; however, the diffusion rates through molten Al_2O_3 should be comparable to those for crystalline film. Properties of all three polymorphs were used in three different calculations. The results are shown in Figure 6.5. A shaded region of the plot represents the time while the ESD pulse was applied to the particle. The temperature traces corresponding to amorphous and α-Al_2O_3 polymorphs growing based on their previously reported diffusion coefficients [165, 169] effectively coincide with one another, and are fully dominated by the heat from ESD pulse. Once the pulse ends, the temperature almost immediately begins to decrease,

suggesting that self-sustained combustion was not achieved in either case. Respectively, oxide thickness increases only slightly in either of the above cases. However, an extended temperature plateau limited by the boiling point of Al is observed if alumina is treated as γ-Al_2O_3 throughout the temperature range. This temperature trace, extending the active redox reaction up to about 100 μs, or well after the ESD pulse ends, represents combustion. Similarly, combustion is predicted when a reduced activation energy of 252 kJ/mol is used for α-Al_2O_3. The temperature traces essentially coincide for the latter two cases. In both cases, the accelerated reaction causes the temperature increasing up to the aluminum boiling point even before the ESD pulse ends. While this temperature is maintained, a substantial growth of alumina is predicted to occur. For comparison, a calculation for the same particle considering the full reaction model, with all alumina polymorphs accounted for is also shown. It is apparent that a reduced reaction rate at lower temperatures, when alumina layer begins to grow, leads to a slightly lower overall reaction progress and to a somewhat shorter reaction time. Figure 6.5 shows that accounting for only one alumina phase with diffusion-limited growth (either γ-Al_2O_3 or α-Al_2O_3 with the activation energy of 252 kJ/mol) enables one to predict the same salient features of heterogeneous combustion as the complete model, although the reaction temperature and completeness of the redox reaction could be somewhat over predicted.

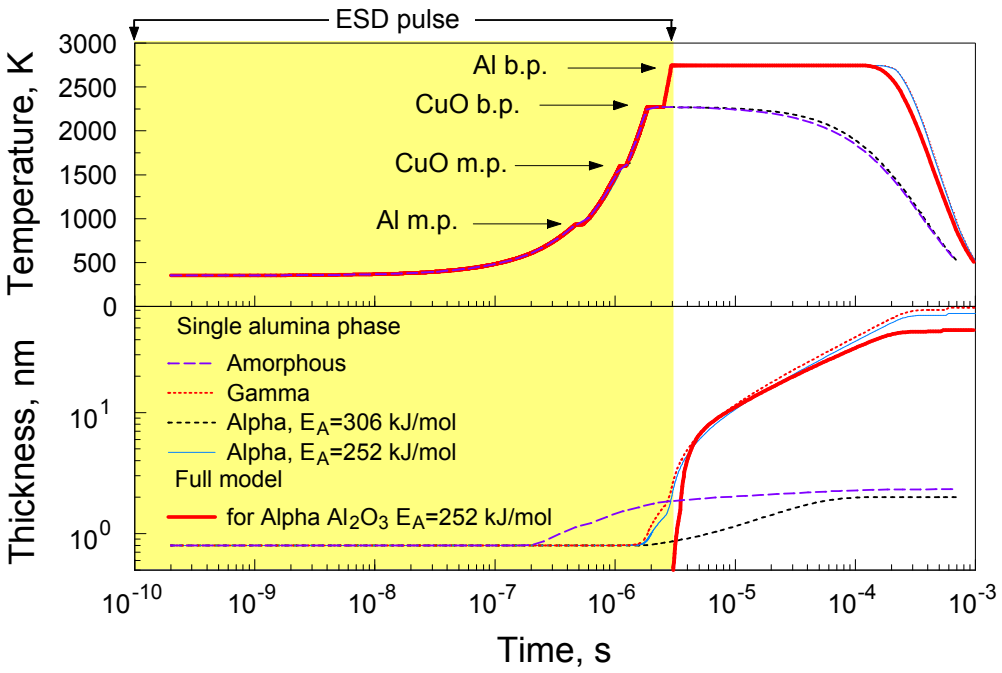

Figure 6.5 Temperature and oxide layer thickness as a function of time for the abridged reaction model accounting for the formation of a single alumina phase in the entire temperature range. The calculations are shown accounting for characteristics of all three alumina polymorphs. For comparison, temperature and α-Al_2O_3 thickness obtained considering the complete model is also shown.

6.6.3 Particle Temperature and Alumina Thickness as a Function of Time

An example of calculated temperature history for a single composite particle with inclusions described by the size distribution given in Figure 6.3 is shown in Figure 6.6. A complete model with various phase changes in the growing alumina layer was used. The shaded portion of the plot represents the time the ESD pulse was applied to the particle. The temperature increases rapidly, passing through a sequence of phase changes, as marked in Figure 6.4 and reaching, for this particle size, the boiling point of alumina before the spark pulse is over. As discussed above, the analysis of the diffusion-limited growth of alumina does not take its melting into account treating it instead as a sequence of solid polymorphs. Calculated thickness of different alumina polymorphs is shown as a function of time in Figure 6.6 for a selected inclusion size, 694 nm diameter. During the

spark pulse, the calculations predict growth of amorphous alumina to slightly more than 1 nm, its transformation to γ-Al_2O_3, which increases to about 2.5 nm before transforming to α-Al_2O_3. Note that alumina melting point is reached at about the same time the model predicts its transformation to α-Al_2O_3. Growth of α-Al_2O_3 continues after the spark pulse is over. This causes further increase in the calculated temperature up to the boiling point of copper. The thickness of the alumina layer reaches nearly 30 nm until its growth rate decreases substantially. The temperature is predicted to begin decreasing after about 20 μs, it decays below 2000 K after about 50 μs. This time is comparable to that of the optical emission pulse measured in the ESD ignition experiments with monolayers of nanocomposite 2Al·3CuO thermite [161, 167].

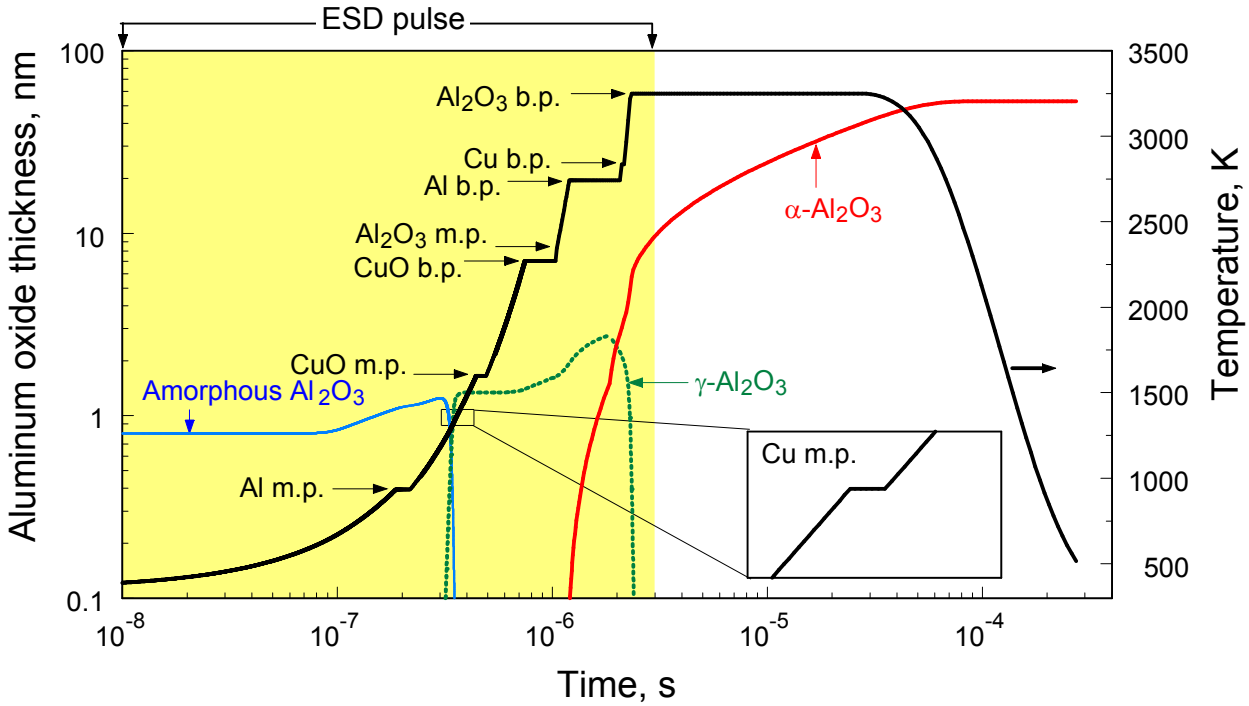

Figure 6.6 Temperature and alumina thickness as a function of time for a 2-μm sized composite particle subjected to a 3 μs duration 8 kV ESD pulse. The alumina polymorph thickness represent evolution of CuO inclusions with the initial diameter of 694 nm.

Similar calculations for a set of particles of different sizes subjected to an 8-kV ESD pulse are shown in Figure 6.7. Different particle sizes are predicted to reach different temperatures and have substantially different burn times. A temperature plateau supported by redox reaction is observed after the ESD pulse for all particle sizes. A substantial heat release leading to either an extended temperature plateau or increase after the ESD pulse is completed is predicted for all but 15-µm particles. In the latter case, the temperature begins decreasing after the ESD pulse ends. It was observed, however, that a slight increase in the initial ESD energy, within the error bar shown in Figure 6.1, could lead to ignition of 15-µm particles as well.

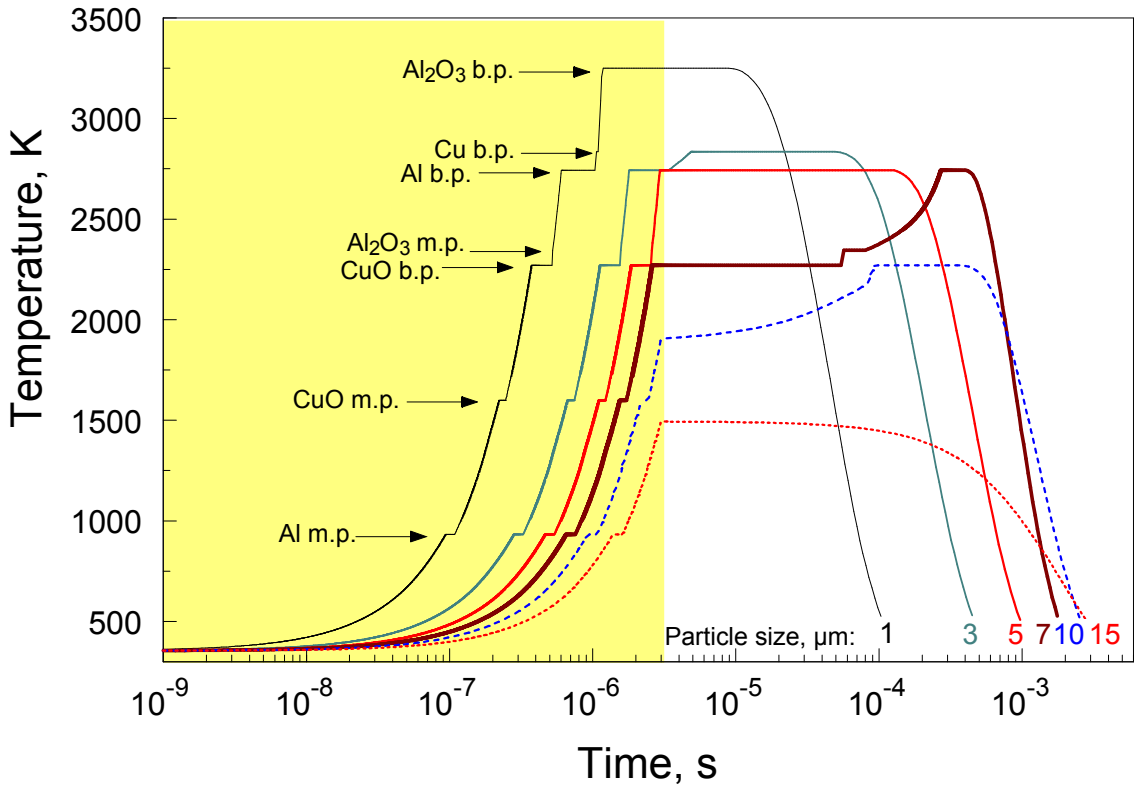

Figure 6.7 Temperature histories for nanocomposite 2Al·3CuO particles of different sizes heated by a 3-µs ESD pulse at 8 kV.

6.6.4 Effect of CuO Inclusion Size, Particle Size, and ESD Energy on Combustion of Nanocomposite Thermite Particles

To clarify the effect of inclusion size, particle size, and ESD energy on ignition and combustion of nanocomposite thermite particles, simplified model particles were considered with a fixed size of CuO inclusions. As specified in Table 6.2, two values for each variable parameter were considered, while the other two parameters were fixed.

Table 6.2 Particle Size, Inclusion Size, and ESD Energy Considered in Calculations for Simplified Model Particles with Monosized CuO Inclusions.

Parameter	Varied values	Fixed value
Particle size, μm	5, 10	5
Inclusion size, μm	100, 1000	100
Ignition energy, μJ	0.15, 0.50	0.50

The effect of inclusion size on predicted temperature histories and oxide film evolution is illustrated in Figure 6.8. The particle with small inclusions (100 nm) was heated up to CuO boiling point during the ESD pulse. After the pulse, the temperature is predicted to increase significantly, exceeding the melting point of Al_2O_3, then boiling point of Al, and reaching the boiling of Cu. The reaction is nearly complete when the temperature begins to decrease. In comparison, the same size particle with larger, 1000 nm inclusions was heated to a slightly lower temperature during the ESD pulse, not reaching the CuO boiling. After the pulse, only a very slight increase in the temperature was predicted, while the oxidation continued at a relatively low rate, resulting in the oxide thickness increasing up to almost 10 nm. The high temperature was predicted to begin decaying after about one half of the time the temperature decrease begun for the particle with fine inclusions.

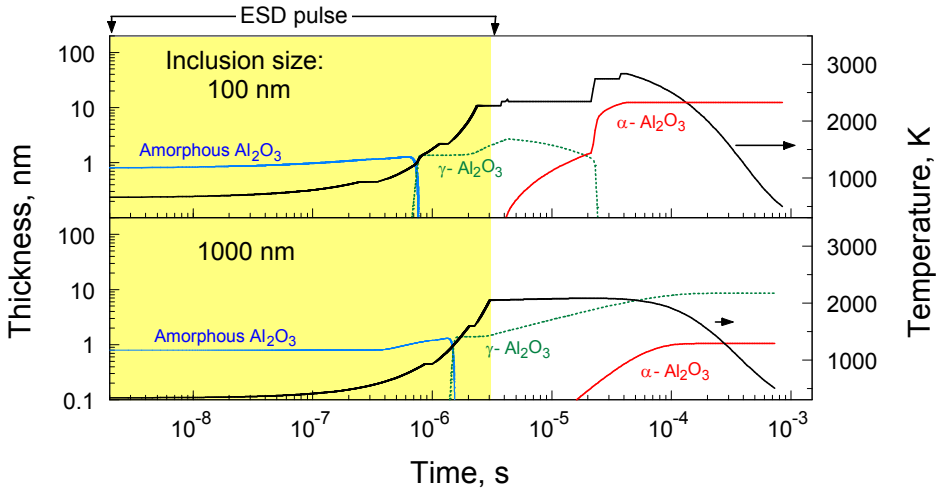

Figure 6.8 Effect of the oxide inclusion size on the predicted combustion temperatures and alumina thickness. Particle size: 5 μm, ESD energy: 0.5 μJ.

The effect of particle size is illustrated in Figure 6.9. The top plot is the same as in Figure 6.8. However, the bottom plot shows a particle with a doubled diameter. The ESD energy only heats this particle to just above the Al melting point. Although oxidation continues after the ESD pulse and a slight temperature increase is predicted, this case can be interpreted as non-ignition. The temperature starts decreasing when only a very thin, less than 2-nm layer of Al_2O_3 has grown.

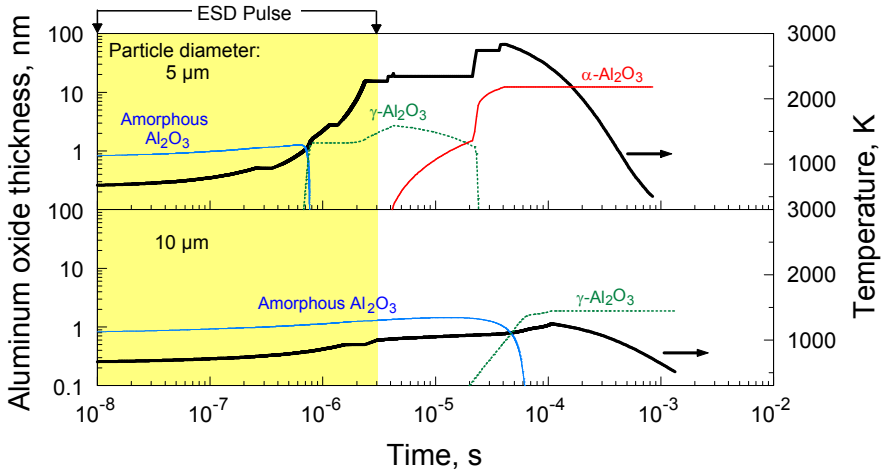

Figure 6.9 Effect of particle size on the predicted combustion temperatures and alumina thickness. CuO inclusions size: 100 nm, ESD energy: 0.5 μJ.

The effect of ESD energy is illustrated in Figure 6.10. Again, the top plot is the same as the top plot in Figures 6.8 and 6.9. The bottom plot shows the effect of a reduced ESD energy for the same particle. During the ESD pulse with reduced energy, the particle passes above aluminum melting but does now reach the CuO melting point. The temperature is observed to decay immediately following the ESD pulse, indicating that the particle did not ignite.

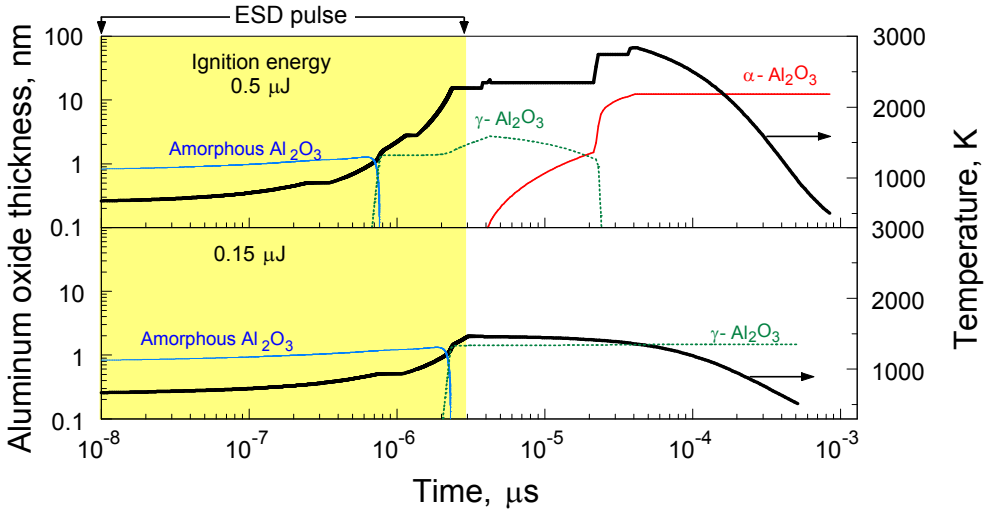

Figure 6.10 Effect of ESD pulse energy on the predicted combustion temperatures and alumina thickness. Particle size: 5 μm; CuO inclusion size: 100 nm.

The results in Figures 6.8 – 6.10 clearly show that the CuO inclusion size, particle size, and the ESD energy all affect the combustion of the ESD-ignited nanocomposite thermite particles. Not surprisingly, finer particles containing finer size inclusions are more likely to be ignited and fully burned. The range of ESD energies considered here only slightly exceeds the threshold minimum ignition energy; although this threshold will be a function of both particle and CuO inclusion dimensions.

6.6.5 Combustion Time

Short burn times were the most distinct feature of the experiments with nanocomposite thermite particles ignited by ESD [90, 161, 167], when very high heating rates were achieved. These times varied in the range of several tens to hundreds of μs. In the present calculations, different reference points in the predicted particle temperature histories can be treated as representing experimental burn times. These reference points are shown in Figure 6.11 for particles of different sizes ignited by an 8-kV ESD pulse. The longest shown times are for the temperatures decreasing below 2000 K. This temperature is selected as still representing strongly optically emitting particles, which are expected to be contributing to the optical emission measured in experiments. These times, varied from ca. 40 to 700 μs are well comparable to the experimental burn times. A somewhat shorter time range, still well comparable to the experimental data is implied considering the times when the temperature just starts decreasing. For larger particles, the latter time effectively coincides with that describing the complete evaporation of Al. One can consider this as a benchmark for the end of heterogeneous reaction. For smaller particles, the complete evaporation of Al is predicted much earlier, by the end of the ESD pulse. As discussed below, in such cases the reaction is heavily overdriven by the ESD energy. Note that the largest particle size shown in Figure 6.11 is 6.10 μm. The calculations do not predict reliable ignition for larger particles unless the ESD energy is increased. Ignition of even a fraction of larger particles in experiments (in which the ESD energy density may vary around its average value assumed in the present calculations) is expected to lead to somewhat longer characteristic reaction times, as generally implied by Figure 6.11.

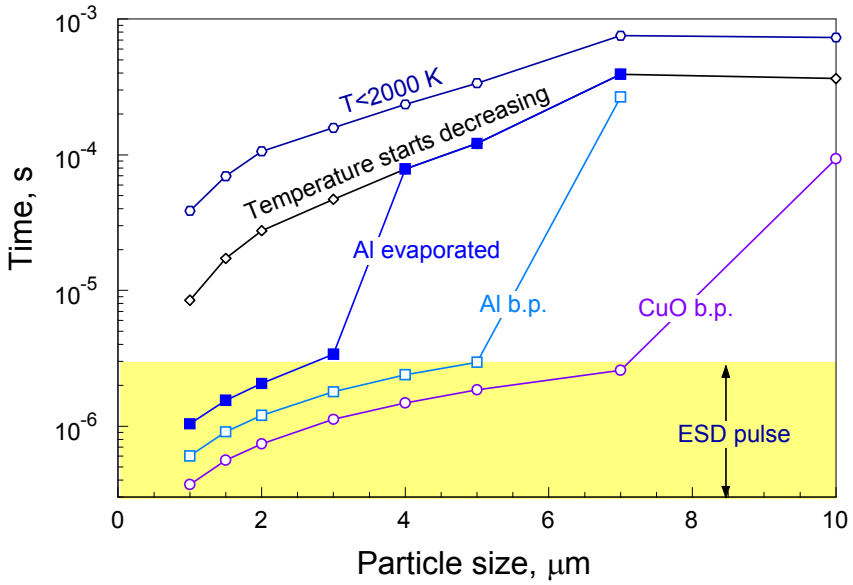

Figure 6.11 Times when predicted specific characteristic temperatures are attained for nanocomposite thermite particles of different sizes heated by an 8-kV ESD pulse.

A somewhat more direct comparison of the calculations and experimental data is shown in Figure 6.12. An experimental emission trace from Ref. [90] for the powder is plotted along with a simulated one. In the simulation, the calculated temperatures (as shown in Figure 6.7) for particles of different sizes, corresponding to the bins of the size distribution shown in Figure 6.4 were considered. For each temperature trace, corresponding to the particle size distribution bin, i, a trace proportional to the optical emission intensity was calculated as $\sim \frac{n_i}{N} D_i^2 T^4$ where $\frac{n_i}{N}$ is fraction of the particles in the number-based distribution shown in Figure 4 and D_i is the respective particle diameter. All reconstructed optical traces for individual size bins were added and normalized. Comparing the traces shown in Figure 6.12, it is apparent that both beginning and the end of the emission signal are very well captured by the model. The peak emission of the simulated trace occurs somewhat sooner than for the measured one; however, this discrepancy is acceptable considering scatter in the experimental data. In particular, an

emission delayed in time would occur if some of the particles ejected by the spark agglomerated and burned as larger particles. Another source of bias occurs in the calculations; all particles were assumed to move with the same speed of 100 m/s. This assumption affects their heat exchange with the surrounding air. In experiments, it is expected that finer particles moved faster, and thus cooled more effectively than larger particles. This would also shift the experimental emission trace to longer times.

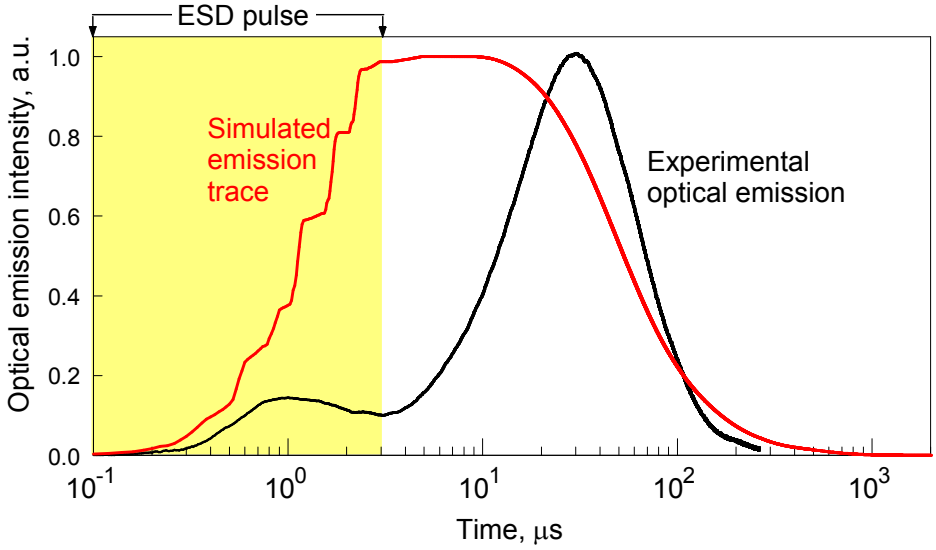

Figure 6.12 Experimental and simulated optical emission traces for the stoichiometric 2Al·3CuO nanocomposite thermite powder ignited by an 8-kV ESD pulse.
Source: [90].

6.6.6 Completeness of the Redox Reaction

The present model describes reaction as occurring simultaneously across all Al_2O_3 interfacial layers separating Al and CuO. However, the thickness of the growing Al_2O_3 layer depends on both diameter of the CuO inclusion within the particle and on the diameter of the particle itself. These effects are illustrated in Figure 6.13. Shown is the reaction conversion factor defined as the ratio of the released heat to the theoretical heat release for the complete reaction. It is defined for each inclusion size separately; it is also

defined for the entire particle. The top set of curves shows conversion factors for individual CuO inclusions of different sizes within particles of two different diameters. For the smallest considered inclusion sizes, 162 and 232 nm, the reaction is completed. For both cases, the reaction is completed first for a smaller, 3-µm particle. This is expected because the smaller particle is heated to a higher temperature in ESD pulse. For larger inclusions, the conversion factor is decreasing with the increased inclusion size; it does not exceed 0.2 for the largest, 2074-nm inclusions. Although the conversion occurs initially faster for all inclusion sizes for the smaller particle, at longer times, the conversion for larger particle becomes greater. This is because the larger particle continues reacting longer (see Figure 6.7), maintaining the high temperature supporting a rapid redox reaction. As a result, the overall conversion factor for the 5-µm particle shown in Figure 6.13 is greater than for 3-µm particle.

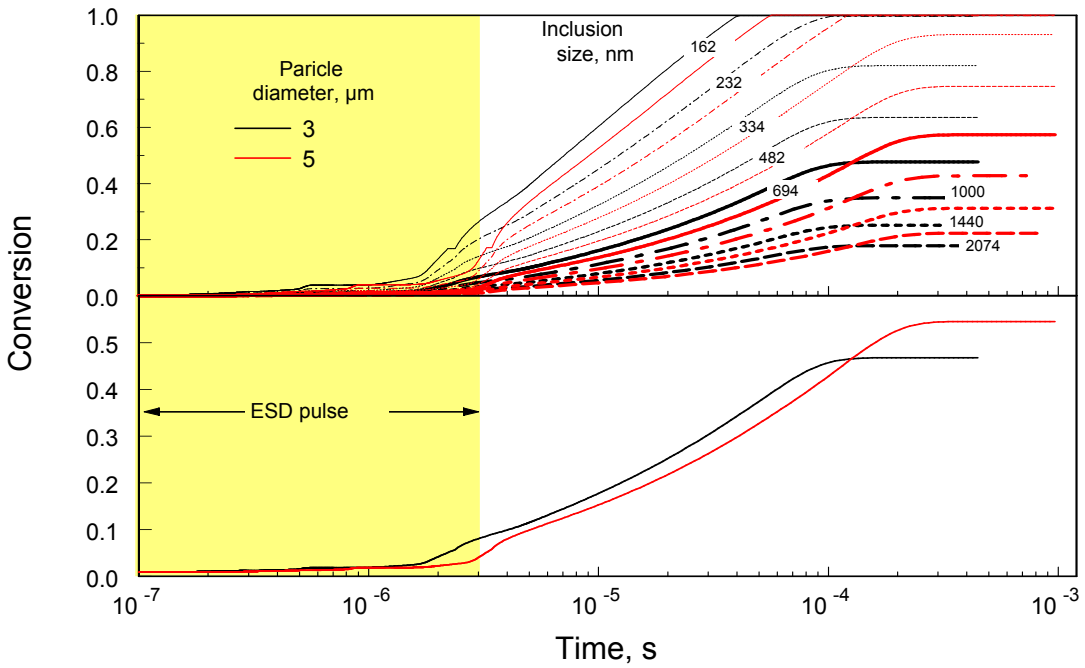

Figure 6.13 Conversion factors for individual inclusion sizes (top) and overall particle conversion (bottom) of a 3- and 5-µm composite thermite particle.

The overall conversion is also affected by the predicted maximum temperature a burning particle attains. As shown in Figure 6.7, this temperature becomes smaller for larger particles, which is expected to lower their conversion. At the same time, the trend of longer burn times expected for larger particles is expected to increase their conversion factor. A summary of overall conversion factors for particles of different sizes is shown in Figure 6.14. The conversion factors are estimated for two characteristic instants predicted in the model: the time all Al is predicted to evaporate, and the time the temperature is predicted to fall below 2000 K. The former conversion increases with the particle size, mostly because of the longer time necessary to evaporate Al, and thus longer time available for the redox reaction to occur. The conversion is estimated neglecting the loss of Al, so that the reaction nominally continues until the temperature drops below 2000 K and is affected by multiple factors. For the very small particles, for which the heat supplied to the particle is significantly dominated by that from ESD pulse the conversion is quite high. It becomes lower for larger particles, for which the redox reaction occurring after the ESD pulse is significant, but which do not reach temperatures as high as overdriven fine particles. An increase in conversion is observed while particle sizes continue increasing, leading to longer reaction times; the decrease in the conversion occurs when the maximum temperatures achieved in combustion become decreasing for still larger particle sizes, bordering the size corresponding the ignition threshold.

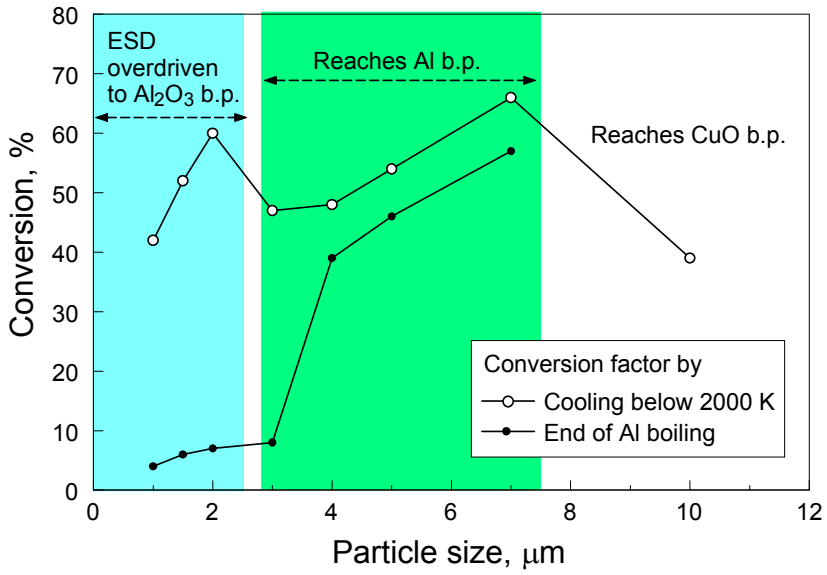

Figure 6.14 Overall reaction conversion factor for composite thermite particles of different sizes.

6.6.7 ESD Energy vs. Redox Reaction Energy

Consider finally the ratio of energies supplied to the particle by ESD discharge and that released by the redox reaction. For simplicity, the calculated energy of the redox reaction is taken for all particle sizes at the instant the particle temperature becomes lower than 2000 K. The ratio is shown in Figure 6.15. It is apparent that particles with sizes less than 4 μm are strongly overdriven by the ESD energy. For larger particles, the ESD and redox reaction energies become comparable. The most significant effect of redox reaction on the energy release is predicted for 7-μm particles. For this size, the ignition is effective and the reaction is predicted to lead to high temperatures enabling significant conversion, as seen in Figure 6.14. For larger particles, the maximum temperatures and conversion factors become lower, and thus the effect of ESD heating becomes greater.

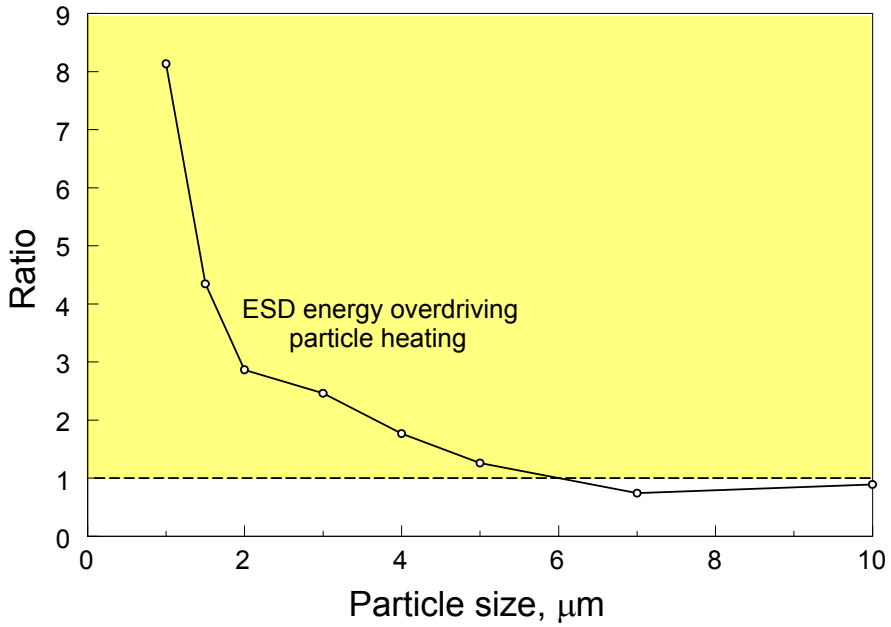

Figure 6.15 Ratio of the energies supplied to a composite particle from ESD pulse to that released by the redox reaction as a function of the particle size.

6.7 Conclusions

It is shown that a model considering heterogeneous reactions occurring at the interfaces between CuO and Al in the stoichiometric nanocomposite 2Al·3CuO thermite describes satisfactorily the experimentally observed short burn times and high temperatures for the particles subjected to very rapid heating by ESD pulse. In the model, the reaction kinetics limited by transport of the reacting species across the growing Al_2O_3 product layer and determined previously in the low-temperature low-heating rate experiments, is extended to much higher temperatures achieved in the present simulations, while the thickness of the growing Al_2O_3 layers remains relatively small because of the very short times considered. The description works when the Al_2O_3 layer is treated as a single phase, discounting the polymorphic phase changes if the activation energy of its diffusion-

controlled growth is around 250 kJ/mol or lower, which corresponds to the kinetics of growth of γ- or α-Al_2O_3. When the polymorphic phase changes are accounted for, the reaction is slightly delayed at short times; however, the high temperature reactions are still described reasonably well. The calculations show the importance of preparing particles with sufficiently small CuO inclusions; larger inclusions remain under-reacted and serve as heat sinks preventing the particle temperature increase. The model also highlights the effect of particle size, affecting the heat exchange with the surrounding gas and also absorption of the ESD pulse energy. It is observed that particles with dimensions around 7 μm containing the CuO inclusions with sizes varied from ca. 160 to 2070 nm burn most completely releasing most energy of the redox reaction, while smaller particles are overdriven by the ESD pulse, and larger particles quench before fully combusting.

CHAPTER 7

CONCLUSION

The overarching goal of this work was to determine the combustion mechanism for micron-sized, nanocomposite thermite particles and find a way to model their combustion behavior. Smaller incremental steps were taken experimentally, culminating in an overall picture of nanocomposite thermite combustion. The first of these steps was exploring ESD ignition of nanocomposite thermite powders, in order to determine the effects of particle sizes, morphology of the mixed components, surrounding environment, and different material compositions. It was found that the reaction rates of the ESD-initiated powders are defined primarily by the scale of mixing of and reactive interface area between fuel and oxidizer in the composite materials, rather than by the external particle surface or particle dimensions. Additionally, Joule energy transferred from ESD to powder depends on both the gas environment and the particle compositions; in turn, the Joule energy affects the number of the ignited particles, their initial velocities, and respective temporal characteristics of the produced emission pulses.

From there it was desired to expand the range of available experimental data describing ignition of reactive nanocomposite thermite powders by ESD. This data was useful for better understanding of the ESD ignition mechanisms. In particular, it was of interest whether a recently developed model of ESD ignition of metal powders [79] was applicable for describing ignition of nanothermites. Second, it was of interest to understand why the same nanocomposite thermites can burn differently depending on the

mode of their initiation. It was discovered that two modes of ignition occurred, prompt and delayed. Promptly ignited powders began burning immediately during the ESD pulse. Their prompt ignition indicated that a threshold ignition temperature was achieved as a result of Joule heating of selected particles even in the relatively weak, low-voltage ESD. Delayed ignition represented combustion of clouds of interacting powder particles, resulting from the homogeneous self-heating among powder particles pre-heated and ejected by ESD. Their products contained phases mixed on a substantially coarser scale compared to that in the starting powders, suggesting that the nano-scale fuel-oxidizer structure of the prepared materials was destroyed upon their ignition, unlike the promptly ignited particles preserving their original nanostructure.

The next step was determining the effect of the material structure and morphology on ignition and combustion of composite thermites, specifically characterization of the similarities and differences between combustion behaviors of reactive materials comprising of stoichiometric Al-CuO (2:3 per mole basis), prepared by traditional ultrasonic mixing (USM) of nano-powders, electrospraying (ES), and ARM. It was found that the reaction with ambient oxidizer is less important for the fully-dense ARM-prepared particles compared to porous ES and USM materials, in which aluminum is always exposed to the ambient gas. While for ES and USM materials, ambient oxidizer accelerates oxidation of aluminum, for the ARM powder, in which CuO and Al are mixed in fully-dense composite structures, it causes formation of spinel, Al2CuO4. When produced, spinel is expected to impede further redox reaction, and thus slow down combustion of ARM prepared powder.

After material structure and morphology were examined, the next step aimed at a direct characterization of the effect of heating rate on the burn rate of different ARM nanocomposite thermite particles. For Al-based thermites, burn times of particles heated by ESD were substantially shorter than those observed for the same, laser-heated particles. Thus, it is confirmed experimentally that the burn rates of nanocomposite thermites prepared by arrested reactive milling can be controlled by the way they are ignited. The differences in the combustion mechanisms of the particles heated by laser and ESD were interpreted considering characteristic times required for the heat propagation through the particle, formation of a molten droplet of aluminum, and the rates of reaction in nanocomposite thermites heated up to the aluminum melting point by laser and ESD. This effect is chiefly due to the difference in the thickness of the Al_2O_3 film grown between Al and oxidizer during heating at respectively different rates. Considering that coalescence of the molten Al into a droplet takes a few μs, which could be further delayed for the ESD-heated particles by the temperature gradients, it is concluded that the redox reaction in the ESD-heated particles will proceed to a much greater extent than in the same particles heated by laser before the nanocomposite structure is lost due to Al melting. This explains a significant difference in the observed burn rates for the particles of the same nanocomposite thermites heated at different rates.

Finally taking into account each of the previous steps, a heterogeneous reaction model was built. It was examined whether it could reasonably describe the very high burn rates of the fully-dense nanocomposite thermite particles heated by ESD. It was shown that a model considering heterogeneous reactions occurring at the interfaces between CuO and Al in the stoichiometric nanocomposite 2Al·3CuO thermite describes

satisfactorily the experimentally observed short burn times and high temperatures for the particles subjected to very rapid heating by ESD pulse. The calculations showed the importance of preparing particles with sufficiently small CuO inclusions; larger inclusions remained under-reacted and served as heat sinks preventing the particle temperature increase. The model successfully predicted the combustion behavior of Al-CuO and thus achieved the overarching goal of determining the combustion mechanism behind nanocomposite thermites.

REFERENCES

1. Goldschmidt, H., *Method of producing metals and alloys.* United States Patent Office, 1897. *Patent US578868*: p. 2.

2. Goldschmidt, H., *Use of thermit for obtaining sound steel ingots.* Engineering (London), 1913. **94**(Copyright (C) 2015 American Chemical Society (ACS). All Rights Reserved.): p. 485-6.

3. Goldschmidt, H. and W. Mathesius, *Process of manufacturing homogeneous metal castings*, 1903. *Patent US733957A*, Germany.

4. Anon, *Field welding alternatives.* Modern Railroads, 1987. **42**(8): p. 39-40.

5. Fischer, S.H. and M.C. Grubelich, *Theoretical energy release of thermites, intermetallics, and combustible metals.* Procceedings International Pyrotechnic Seminar, 1998. **24th**(Copyright (C) 2015 American Chemical Society (ACS). All Rights Reserved.): p. 231-286.

6. Shaw, J., *Experience with flashwelded rails in london transport service.* Canadian Metallurgical Quarterly, 1982. **21**(1): p. 47-57.

7. Park, G.A., D.D. Domonoske, and R.P. Faherty, *Thermite welding of crane rails at Kasier Steel.* Iron and Steel Engineer, 1977. **54**(9): p. 77-82.

8. Walton, J.D.J. and N.E. Poulos, *Cermets From Thermite Reactions.* Journal of the American Ceramic Society, 1959. **42**(1): p. 40-49.

9. Odawara, O. and J. Ikeuchi, *Vacuum centrifugal - thermite process for producing ceramic-lined pipes.* Journal of the American Ceramic Society, 1986. **69**(4): p. C85-C86.

10. Danner, C.E. and J. Goldenson, *Analysis of thermite-type incendiary and pyrotechnic mixtures.* Analytical Chemistry, 1947. **19**(9): p. 627-630.

11. Wang, L.L., Z.A. Munir, and Y.M. Maximov, *Thermite reactions: their utilization in the synthesis and processing of materials.* Journal of Materials Science, 1993. **28**(14): p. 3693-3708.

12. Kim, S.H. and M.R. Zachariah, *Enhancing the rate of energy release from nanoenergetic materials by electrostatically enhanced assembly.* Advanced Materials, 2004. **16**(20): p. 1821-1825.

13. Schoenitz, M., T.S. Ward, and E.L. Dreizin. *Fully dense nano-composite energetic powders prepared by arrested reactive milling*. 2005. Chicago, IL.

14. Pantoya, M.L. and J.J. Granier, *Combustion behavior of highly energetic thermites: Nano versus micron composites.* Propellants, Explosives, Pyrotechnics, 2005. **30**(1): p. 53-62.

15. Yetter, R.A., G.A. Risha, and S.F. Son, *Metal particle combustion and nanotechnology.* in *The Combustion Institute Proceedings*, 2009. **32 II**: p. 1819-1838.

16. Kelly, M.D. and L.D. Abney, *Thermal profiles of thermite reactions.* in *SPIE - The International Society for Optical Engineering Proceedings*, 1985. **520**: p. 149-151.

17. Dreizin, E.L., *Metal-based reactive nanomaterials.* Progress in Energy and Combustion Science, 2009. **35**(2): p. 141-167.

18. Stamatis, D. and E.L. Dreizin. *Fully dense Al-CuO nanocomposite powders for energetic formulations*. 2008. Reno, NV.

19. Sundaram, D., V. Yang, and R.A. Yetter, *Metal-based nanoenergetic materials: Synthesis, properties, and applications.* Progress in Energy and Combustion Science, 2017. **61**: p. 293-365.

20. Elbasuney, S., et al., *Stabilized super-thermite colloids: A new generation of advanced highly energetic materials.* Applied Surface Science, 2017. **419**: p. 328-336.

21. Mastrangeli, M., et al. *Automated real-time control of fluidic self-Assembly of microparticles*. in *IEEE International Conference on Robotics and Automation Proceedings.* 2014.

22. Walter, K.C., D.R. Pesiri, and D.E. Wilson, *Manufacturing and performance of nanometric Al/MoO 3 energetic materials.* Journal of Propulsion and Power, 2007. **23**(4): p. 645-650.

23. Wang, H., et al., *Assembly and reactive properties of Al/CuO based nanothermite microparticles.* Combustion and Flame, 2014. **161**(8): p. 2203-2208.

24. Wang, H., et al., *Electrospray formation and combustion characteristics of iodine-containing Al/CuO nanothermite microparticles.* Combustion and Flame, 2015. **162**(7): p. 2823-2829.

25. Shin, M.S., et al., *Reaction characteristics of Al/Fe 2O 3 nanocomposites.* Journal of Industrial and Engineering Chemistry, 2012. **18**(5): p. 1768-1773.

26. Seo, H.S., et al., *Thermal behavior of Al/MoO3 xerogel nanocomposites.* Journal of Industrial and Engineering Chemistry, 2014. **20**(1): p. 189-193.

27. Malchi, J.Y., T.J. Foley, and R.A. Yetter, *Electrostatically self-assembled nanocomposite reactive microspheres.* ACS Applied Materials and Interfaces, 2009. **1**(11): p. 2420-2423.

28. Sullivan, K.T., J.D. Kuntz, and A.E. Gash, *Electrophoretic deposition and mechanistic studies of nano-Al/CuO thermites.* Journal of Applied Physics, 2012. **112**(2).

29. Li, X., et al., *Direct deposit laminate nanocomposites with enhanced propellent properties.* ACS Applied Materials and Interfaces, 2015. **7**(17): p. 9103-9109.

30. Jouet, R.J., et al., *Surface passivation of bare aluminum nanoparticles using perfluoroalkyl carboxylic acids.* Chemistry of Materials, 2005. **17**(11): p. 2987-2996.

31. Foley, T., C. Johnson, and K. Higa, *Inhibition of oxide formation on aluminum nanoparticles by transition metal coating.* Chemistry of Materials, 2005. **17**(16): p. 4086-4091.

32. Chintersingh, K.L., M. Schoenitz, and E.L. Dreizin, *Oxidation kinetics and combustion of boron particles with modified surface.* Combustion and Flame, 2016. **173**: p. 288-295.

33. Liu, X., et al., *Effect of purity and surface modification on stability and oxidation kinetics of boron powders.* Thermochimica Acta, 2017. **652**: p. 17-23.

34. Mehendale, B., et al., *Nanoenergetic composite of mesoporous iron oxide and aluminum nanoparticles.* Journal of Energetic Materials, 2006. **24**(4): p. 341-360.

35. Subramanium, S., et al., *Self-assembled ordered energetic composites of CuO nanorods and nanowells and Al nanoparticles with high burn rates*. Vol. 896. 2005.

36. Apperson, S., et al., *Generation of fast propagating combustion and shock waves with copper oxide/aluminum nanothermite composites.* Applied Physics Letters, 2007. **91**(24).

37. Bezmelnitsyn, A., et al., *Modified nanoenergetic composites with tunable combustion characteristics for propellant applications.* Propellants, Explosives, Pyrotechnics, 2010. **35**(4): p. 384-394.

38. Thiruvengadathan, R., et al., *Combustion characteristics of novel hybrid nanoenergetic formulations.* Combustion and Flame, 2011. **158**(5): p. 964-978.

39. Adams, D.P., *Reactive multilayers fabricated by vapor deposition: A critical review.* Thin Solid Films, 2015. **576**: p. 98-128.

40. Blickley, M.P., et al. *Low temperature annealing effects on magnetron sputtered Ni(V)/Al reactive coatings*. in *Materials Research Society Symposium Proceedings*. 2005.

41. Weihs, T.P., *Fabrication and characterization of reactive multilayer films and foils*, in *Metallic Films for Electronic, Optical and Magnetic Applications: Structure, Processing and Properties Proceedings*. 2013. p. 160-243.

42. Theodossiadis, G.D. and M.F. Zaeh, *Study of the kinetic and energetic reaction properties of multilayered aluminum–nickel nanofoils.* Production Engineering, 2017. **11**(3): p. 245-253.

43. Theodossiadis, G.D. and M.F. Zaeh, *In-situ investigation of the thermal reaction properties of multilayered aluminum–nickel nanofoils.* Production Engineering, 2017. **11**(4-5): p. 373-381.

44. Theodossiadis, G.D. and M.F. Zaeh, *Assessment of the technological potential and maturity of a novel joining technique based on reactive nanofoils.* Production Engineering, 2017. **11**(3): p. 237-243.

45. Schoenitz, M., T. Ward, and E.L. Dreizin. *Preparation of energetic metastable nano-composite materials by arrested reactive milling*. 2003. Boston, MA.

46. Schoenitz, M., T.S. Ward, and E.L. Dreizin. *Arrested reactive milling for in-situ production of energetic nanocomposites for propulsion and energy-intensive technologies in exploration missions*. 2005. Reno, NV.

47. Badiola, C., et al., *Nanocomposite thermite powders prepared by cryomilling.* Journal of Alloys and Compounds, 2009. **488**(1): p. 386-391.

48. Umbrajkar, S.M., et al., *Aluminum-rich Al-MoO3 nanocomposite powders prepared by arrested reactive milling.* Journal of Propulsion and Power, 2008. **24**(2): p. 192-198.

49. Schoenitz, M., S. Umbrajkar, and E.L. Dreizin, *Kinetic analysis of thermite reactions in Al-MoO3 nanocomposites.* Journal of Propulsion and Power, 2007. **23**(4): p. 683-687.

50. Williams, R.A., J.V. Patel, and E.L. Dreizin, *Ignition of fully dense nanocomposite thermite powders by an electric spark.* Journal of Propulsion and Power, 2014. **30**(3): p. 765-774.

51. Stamatis, D., et al., *Fully dense, aluminum-rich Al-CuO nanocomposite powders for energetic formulations.* Combustion Science and Technology, 2009. **181**(1): p. 97-116.

52. Williams, R.A., M. Schoenitz, and E.L. Dreizin, *Validation of the thermal oxidation model for Al/CuO nanocomposite powder.* Combustion Science and Technology, 2014. **186**(1): p. 47-67.

53. Williams, R.A., et al., *On gas release by thermally-initiated fully-dense 2Al·3CuO nanocomposite powder.* . International Journal of Energetic Materials and Chemical Propulsion, 2012. **11**(3): p. 275-292.

54. Dreizin, E.L., et al., *Particle Combustion Dynamics of Metal-Based Reactive Materials.* International Journal of Energetic Materials and Chemical Propulsion, 2011. **10**(4): p. 22.

55. Ermoline, A., M. Schoenitz, and E.L. Dreizin, *Reactions leading to ignition in fully dense nanocomposite Al-oxide systems.* Combustion and Flame, 2011. **158**(6): p. 1076-1083.

56. Ermoline, A., et al., *Preparation and characterization of granular hybrid reactive materials.* International Journal of Energetic Materials and Chemical Propulsion, 2010. **9**(3): p. 267-284.

57. Stamatis, D., et al. *Consolidation of reactive nanocomposite powders*. 2009. Denver, CO.

58. Stamatis, D., et al., *Aluminum burn rate modifiers based on reactive nanocomposite powders.* Propellants, Explosives, Pyrotechnics, 2010. **35**(3): p. 260-267.

59. Umbrajkar, S.M., M. Schoenitz, and E.L. Dreizin, *Exothermic reactions in Al-CuO nanocomposites.* Thermochimica Acta, 2006. **451**(1-2): p. 34-43.

60. Williams, R.A., et al., *Correlation of optical emission and pressure generated upon ignition of fully-dense nanocomposite thermite powders.* Combustion and Flame, 2013. **160**(3): p. 734-741.

61. Williams, R.A., et al., *Low-temperature exothermic reactions in fully-dense Al/MoO3 nanocomposite powders.* Thermochimica Acta, 2014. **594**(0): p. 1-10.

62. Stamatis, D., E.L. Dreizin, and K. Higa, *Thermal initiation of Al-MoO3 nanocomposite materials prepared by different methods.* Journal of Propulsion and Power, 2011. **27**(5): p. 1079-1087.

63. Umbrajkar, S.M., M. Schoenitz, and E.L. Dreizin, *Control of structural refinement and composition in Al-MoO3 nanocomposites prepared by arrested reactive milling.* Propellants, Explosives, Pyrotechnics, 2006. **31**(5): p. 382-389.

64. Stamatis, D. and E.L. Dreizin, *Thermal initiation of consolidated nanocomposite thermites.* Combustion and Flame, 2011. **158**(8): p. 1631-1637.

65. Stamatis, D., A. Ermoline, and E.L. Dreizin, *A Multi-Step Reaction Model for Ignition of Fully-Dense Al•CuO Nanocomposite Powders.* Combustion Theory and Modelling, 2012. **16**(6): p. 976-993.

66. Cabrera, N. and N.F. Mott, *Theory of the oxidation of metals.* Reports on Progress in Physics, 1949. **12**(1): p. 163-184.

67. Ermoline, A. and E.L. Dreizin, *Equations for the Cabrera-Mott kinetics of oxidation for spherical nanoparticles.* Chemical Physics Letters, 2011. **505**(1-3): p. 47-50.

68. Sullivan, K.T., et al., *Reactive sintering: An important component in the combustion of nanocomposite thermites.* Combustion and Flame, 2012. **159**(1): p. 2-15.

69. Manea, S., et al. *Electrical and electrostatic discharge solid rocket booster ignition*. in *45th AIAA/ASME/SAE/ASEE Joint Propulsion Conference and Exhibit*. 2009.

70. Bulian, C.J., J.A. Puszynski, and J.J. Swiatkiewicz. *Ignition sensitivity of nanoenergetics produced by various processing methods*. in *AIChE Annual Meeting, Conference Proceedings*. 2007. Salt Lake City, UT.

71. Skinner, D., D. Olson, and A. Block-Bolten, *Electrostatic discharge ignition of energetic materials.* Propellants, Explosives, Pyrotechnics, 1998. **23**(1): p. 34-42.

72. Roux, M., M. Auzanneau, and C. Brassy, *Electric spark and ESD sensitivity of reactive solids (primary or secondary explosive, propellant, pyrotechnics) part one: experimental results and reflection factors for sensitivity test optimization.* Propellants, Explosives, Pyrotechnics, 1993. **18**(6): p. 317-324.

73. Weir, C., M.L. Pantoya, and M.A. Daniels, *The role of aluminum particle size in electrostatic ignition sensitivity of composite energetic materials.* Combustion and Flame, 2013. **160**(10): p. 2279-2281.

74. Johnson, C.E., et al. *Thermite initiation processes and thresholds*. in *Materials Research Society Symposium Proceedings*. 2011.

75. Higa, K.T., *Energetic nanocomposite lead-free electric primers.* Journal of Propulsion and Power, 2007. **23**(4): p. 722-727.

76. Foley, T., et al., *Development of nanothermite composites with variable electrostatic discharge ignition thresholds.* Propellants, Explosives, Pyrotechnics, 2007. **32**(6): p. 431-434.

77. Williams, R.A., E. Beloni, and E.L. Dreizin, *Ignition of metal powder layers of different thickness by electrostatic discharge.* Journal of Propulsion and Power, 2012. **28**(1): p. 132-139.

78. Beloni, E., P.R. Santhanam, and E.L. Dreizin, *Electrical conductivity of a metal powder struck by a spark.* Journal of Electrostatics, 2012. **70**(1): p. 157-165.

79. Beloni, E. and E.L. Dreizin, *Model of heating and ignition of conductive polydisperse powder in electrostatic discharge.* Combustion Theory and Modelling, 2012. **16**(6): p. 976-993.

80. Dreizin, E.L. and M. Schoenitz, *Nano-composite energetic powders prepared by arrested reactive milling*, in *US Patent 7,524,355* 2009.

81. Williams, R.A., J.V. Patel, and E.L. Dreizin, *Ignition of Fully Dense Nanocomposite Thermite Powders by an Electric Spark.* Journal of Propulsion and Power, 2014. **in press**.

82. Shaw, W.L., et al., *Ignition of nanocomposite thermites by electric spark and shock wave.* Propellants, Explosives, Pyrotechnics, 2014. **in press**.

83. Stamatis, D., et al., *Consolidation and mechanical properties of reactive nanocomposite powders.* Powder Technology, 2011. **208**(3): p. 637-642.

84. Dreizin, E.L., A.V. Suslov, and M.A. Trunov, *General trends in metal particles heterogeneous combustion.* Combustion science and technology, 1993. **90**(1-4): p. 79-99.

85. Dreizin, E.L., *Phase changes in metal combustion.* Progress in Energy and Combustion Science, 2000. **26**(1): p. 57-78.

86. Pearse, R.W.B. and G. A.G., *The identification of molecular spectra*. Fourth Edition ed. 1976, London: Chapman and Hall. 397.

87. Beloni, E. and E.L. Dreizin, *Experimental study of ignition of magnesium powder by electrostatic discharge.* Combustion and Flame, 2009. **156**(7): p. 1386-1395.

88. Meek, J.M., *A theory of spark discharge.* Physical Review, 1940. **57**(8): p. 722-728.

89. Olsen, H.L., R.B. Edmonson, and E.L. Gayhart, *Microchronometric schlieren study of gaseous expansion from an electric spark.* Journal of Applied Physics, 1952. **23**(10): p. 1157-1162.

90. Monk, I., et al., *Electro-static discharge ignition of monolayers of nanocomposite thermite powders prepared by arrested reactive milling.* Combustion Science and Technology, 2015. **187**(8): p. 1276-1294.

91. Shaw, W.L., et al. *Using laser-driven flyer plates to study the shock initiation of nanoenergetic materials*. in *18th Biennial Intl. Conference of the APS Topical Group on Shock Compression of Condensed Matter*. 2013. Seattle, Washington: APS.

92. Shaw, W.L., et al., *Ignition of nanocomposite thermites by electric spark and shock wave.* Propellants, Explosives, Pyrotechnics, 2014. **39**(3): p. 444-453.

93. Wang, P. and J. Zhang, *Review on pyrotechnic cutting technology.* Hanneng Cailiao/Chinese Journal of Energetic Materials, 2010. **18**(4): p. 476-480.

94. Knapp, S., et al., *Modeling ignition and thermal wave progression in binary granular pyrotechnic compositions.* Propellants, Explosives, Pyrotechnics, 2014. **39**(3): p. 423-433.

95. Gromov, A., et al., *Nanometals in energetic systems: achievements and future.* Int. J. Energ. Mater. Chem. Propul., 2014. **13**(Copyright (C) 2015 American Chemical Society (ACS). All Rights Reserved.): p. 399-419.

96. Martirosyan, K.S., *Nanoenergetic gas-generators: Principles and applications.* Journal of Materials Chemistry, 2011. **21**(26): p. 9400-9405.

97. Bouma, R.H.B., et al., *Shear initiation of Al/MoO3-based reactive materials.* Propellants, Explosives, Pyrotechnics, 2007. **32**(6): p. 447-453.

98. Feng, J., et al., *Passivated iodine pentoxide oxidizer for potential biocidal nanoenergetic applications.* ACS Applied Materials and Interfaces, 2013. **5**(18): p. 8875-8880.

99. Dreizin, E.L., D.J. Allen, and N.G. Glumac, *Depression of melting point for protective aluminum oxide films.* Chemical Physics Letters, 2014. **618**: p. 63-65.

100. Ikemiya, N., et al., *Surface tensions and densities of molten Al2O3, Ti2O3, V2O5 and Nb2O5.* ISIJ International, 1993. **33**(1): p. 156-165.

101. Abdel-Aziz, A.K. and M.B. Kirshah, *The density and temperature dependence of the surface tension of molten bismuth, lead, and bismuth-lead alloys.* Z. Metallkd., 1977. **68**(Copyright (C) 2015 American Chemical Society (ACS). All Rights Reserved.): p. 437-9.

102. Friedman, R. and A. Macek, *Ignition and combustion of aluminum particles in hot, ambient gases.* Combust. Flame, 1962. **6**(Copyright (C) 2015 American Chemical Society (ACS). All Rights Reserved.): p. 9-19.

103. Friedman, R. and A. Macek, *Combustion studies of single aluminum particles.* Symp. (Int.) Combust., [Proc.], 1963(Copyright (C) 2015 American Chemical Society (ACS). All Rights Reserved.): p. 703-12.

104. Macek, A. *Fundamentals of combustion of single aluminum and beryllium particles*. 1967.

105. Macek, A. and J.M. Semple, *Combustion of boron particles at atmospheric pressure.* Combust. Sci. Technol., 1969. **1**(Copyright (C) 2015 American Chemical Society (ACS). All Rights Reserved.): p. 181-91.

106. Prentice, J.L., *On the combustion of single aluminium particles.* Combustion and Flame, 1965. **9**(2): p. 208-210.

107. Dreizin, E.L., *Experimental study of aluminum particle flame evolution in normal and micro-gravity.* Combustion and Flame, 1998. **116**(3): p. 323-333.

108. McBride, B.J. and S. Gordon, *Computer program for calculation of complex chemical equilibrium compositions and applications ii. Users manual and program description.* 1996: NASA RP 1311.

109. Spitzer, D., et al., *Energetic nano-materials: Opportunities for enhanced performances.* Journal of Physics and Chemistry of Solids, 2010. **71**(2): p. 100-108.

110. Comet, M., et al., *Phosphorus-based nanothermites: A new generation of energetic materials.* Journal of Physics and Chemistry of Solids, 2010. **71**(2): p. 64-68.

111. Comet, M., et al., *Phosphorus-based nanothermites: A new generation of pyrotechnics illustrated by the example of n-CuO/Red P mixtures.* Propellants, Explosives, Pyrotechnics, 2010. **35**(3): p. 220-225.

112. Reese, D.A., D.M. Wright, and S.F. Son, *CuO/Al thermites for solid rocket motor ignition.* Journal of Propulsion and Power, 2013. **29**(5): p. 1194-1199.

113. Sun, J., M.L. Pantoya, and S.L. Simon, *Dependence of size and size distribution on reactivity of aluminum nanoparticles in reactions with oxygen and MoO3.* Thermochimica Acta, 2006. **444**(2): p. 117-127.

114. Sanders, V.E., et al., *Reaction propagation of four nanoscale energetic composites (Al/M0O 3, Al/WO3, Al/CuO, and Bi2O3).* Journal of Propulsion and Power, 2007. **23**(4): p. 707-714.

115. Jacob, R.J., B. Wei, and M.R. Zachariah, *Quantifying the enhanced combustion characteristics of electrospray assembled aluminum mesoparticles.* Combustion and Flame, 2015.

116. Son, S.F., et al., *Combustion of nanoscale Al/MoO3 thermite in microchannels.* Journal of Propulsion and Power, 2007. **23**(4): p. 715-721.

117. Dutro, G.M., et al., *The effect of stoichiometry on the combustion behavior of a nanoscale Al/M0O3 thermite.* in Combustion Institute *Proceedings*, 2009. **32 II**: p. 1921-1928.

118. Bockmon, B.S., et al., *Combustion velocities and propagation mechanisms of metastable interstitial composites.* Journal of Applied Physics, 2005. **98**(6): p. 1-7.

119. Young, G., H. Wang, and M.R. Zachariah, *Application of nano-aluminum/nitrocellulose mesoparticles in composite solid rocket propellants.* Propellants, Explosives, Pyrotechnics, 2015. **40**(3): p. 413-418.

120. Dreizin, E.L. and M. Schoenitz, *Reactive and metastable nanomaterials prepared by mechanical milling*, in *Metal Nanopowders*. 2014, Wiley-VCH Verlag GmbH & Co. KGaA. p. 227-278.

121. Monk, I., M. Schoenitz, and E.L. Dreizin, *Modes of ignition of powder layers of nanocomposite thermites by electro-static discharge.* Journal of Energetic Materials, 2016. **in Press**.

122. Goroshin, S., et al. *Emission spectroscopy of flame fronts in aluminum suspensions*. 2007. Heidelberg.

123. Weismiller, M.R., J.G. Lee, and R.A. Yetter, *Temperature measurements of Al containing nano-thermite reactions using multi-wavelength pyrometry.* Proc. Combust. Inst., 2011. **33**(Copyright (C) 2015 American Chemical Society (ACS). All Rights Reserved.): p. 1933-1940.

124. Dreizin, E.L., *Experimental study of stages in aluminum particle combustion in air.* Combustion and Flame, 1996. **105**(4): p. 541-556.

125. Jacob, R.J., et al., *Energy release pathways in nanothermites follow through the condensed state.* Combustion and Flame, 2015. **162**(1): p. 258-264.

126. Standards, U.S.N.B.o., et al., *Phase diagrams for ceramists*. 1981: American Ceramic Society.

127. Goldchmidt, *The early years.* Goldchmidt Thermit Group.

128. Honda, K., et al., *New thermite welding repair technology: high strength gunned body and high safety structure.* Taikabutsu, 2013. **65**(Copyright (C) 2015 American Chemical Society (ACS). All Rights Reserved.): p. 439-442.

129. Jury, B.F., *Apparatus and method of aluminothermic welding of railway lines*, in *Patent WO201401435 9A2*. 2014, N. Z. . p. 29pp.

130. Yuan, X.Y., et al., *Novel method of thermite welding.* Science and Technology of Welding and Joining, 2010. **15**(1): p. 54-58.

131. Trunov, M.A., et al., *Effect of polymorphic phase transformations in Al2O3 film on oxidation kinetics of aluminum powders.* Combustion and Flame, 2005. **140**(4): p. 310-318.

132. Yetter, R.A., G.A. Risha, and S.F. Son. *Metal particle combustion and nanotechnology*. 2009. Montreal, QC.

133. Mukasyan, A.S., A.S. Rogachev, and S.T. Aruna, *Combustion synthesis in nanostructured reactive systems.* Advanced Powder Technology, 2015. **26**(3): p. 954-976.

134. Blobaum, K.J., et al., *Deposition and characterization of a self-propagating CuOx/Al thermite reaction in a multilayer foil geometry.* Journal of Applied Physics, 2003. **94**(5): p. 2915-2922.

135. Apperson, S.J., et al., *Characterization of nanothermite material for solid-fuel microthruster applications.* Journal of Propulsion and Power, 2009. **25**(5): p. 1086-1091.

136. Sutherland, G.T., P.J. Miller, and H.W. Sandusky, *Ordnance warheads with thermite heating-induced dispersal of molten metal charges*. 2006, The United States of America as Represented by the Secretary of the Navy, USA . p. 6pp.

137. Rossi, C., et al., *Nanoenergetic materials for MEMS: A review.* Journal of Microelectromechanical Systems, 2007. **16**(4): p. 919-931.

138. Chakraborty, P. and M.R. Zachariah, *Do nanoenergetic particles remain nano-sized during combustion?* Combustion and Flame, 2014. **161**(5): p. 1408-1416.

139. Sullivan, K.T., et al., *In situ microscopy of rapidly heated nano-Al and nano- Al/ WO3 thermites.* Applied Physics Letters, 2010. **97**(13).

140. Monk, I., M. Schoenitz, and E.L. Dreizin, *Modes of Ignition of Powder Layers of Nanocomposite Thermites by Electrostatic Discharge.* Journal of Energetic Materials, 2016. **35**(1): p. 29-43.

141. Monk, I., M. Schoenitz, and E.L. Dreizin, *Modes of ignition of powder layers of nanocomposite thermites by electrostatic discharge.* Journal of Energetic Materials, 2017. **35**(1): p. 29-43.

142. Dreizin, E.L. and M. Schoenitz, *Reactive and Metastable Nanomaterials Prepared by Mechanical Milling*, in *Metal Nanopowders: Production, Characterization, and Energetic Applications*. 2014, Wiley Blackwell. p. 227-278.

143. Schoenitz, M., T. Ward, and E.L. Dreizin. *Preparation of energetic metastable nano-composite materials by arrested reactive milling*. in *Synthesis, Characterization and Properties of Energetic/Reactive Nanomaterials*. 2003. Boston, MA.

144. Chintersingh, K.L., et al., *Combustion of boron particles in products of an air–acetylene flame.* Combustion and Flame, 2016. **172**: p. 194-205.

145. Corcoran, A., et al., *Combustion of fine aluminum and magnesium powders in water.* Combustion and Flame, 2013. **160**(10): p. 2242-2250.

146. Corcoran, A., et al., *Combustion of mechanically alloyed Al·Mg powders in products of a hydrocarbon flame.* Combustion Science and Technology, 2014. **187**(5): p. 807-825.

147. Wang, S., A. Corcoran, and E.L. Dreizin, *Combustion of magnesium powders in products of an air/acetylene flame.* Combustion and Flame, 2015. **162**(4): p. 1316-1325.

148. Wang, S., S. Mohan, and E.L. Dreizin, *Effect of flow conditions on burn rates of metal particles.* Combustion and Flame, 2016. **168**: p. 10-19.

149. Dreizin, E.L., *On the mechanism of asymmetric aluminum particle combustion.* Combustion and Flame, 1999. **117**(4): p. 841-850.

150. Badiola, C. and E.L. Dreizin, *On weak effect of particle size on its burn time for micron-sized aluminum powders.* Combustion Science and Technology, 2012. **184**(12): p. 1993-2007.

151. Badiola, C. and E.L. Dreizin, *Combustion of micron-sized particles of titanium and zirconium.* in *Combustion Institute Proceedings*, 2013. **34**(2): p. 2237-2243.

152. Fischer, S.H. and M.C. Grubelich, *Theoretical energy release of thermites, intermetallics, and combustible metals*, in *Other Information: Supercedes report DE98005512; PBD: Jun 1998; PBD: 1 Jun 1998*. 1998. p. Medium: ED; Size: 59 pages.

153. Jensen, J.E., C.D. Center, and B.N. Laboratory, *Brookhaven National Laboratory selected cryogenic data notebook*. 1980: Brookhaven National Laboratory, Associated Universities, Inc.

154. Bainbridge, I.F. and J.A. Taylor, *The surface tension of pure aluminum and aluminum alloys.* Metallurgical and Materials Transactions A: Physical Metallurgy and Materials Science, 2013. **44**(8): p. 3901-3909.

155. Chen, Y., et al., *Heat transfer modelling of rail thermite welding,* in *The Institution of Mechanical Engineers Proceedings*, Part F: Journal of Rail and Rapid Transit, 2006. **220**(3): p. 207-217.

156. Lloyd, C.A.C., *A method for joining metals by thermite welding*, in *Patent ZA2013002126A*. 2013, Thermitrex Pty Limited, S. Afr. . p. 22pp.

157. Dreizin, E.L. and M. Schoenitz, *Mechanochemically prepared reactive and energetic materials: a review.* Journal of Materials Science, 2017. **52**(20): p. 11789-11809.

158. Yang, L.C. *Ignition transfer effectiveness from primers to physically separated pyrotechnic boosters*. in *49th AIAA/ASME/SAE/ASEE Joint Propulsion Conference*. 2013.

159. Sullivan, K.T., et al., *Quantifying dynamic processes in reactive materials: An extended burn tube test.* Propellants, Explosives, Pyrotechnics, 2015. **40**(3): p. 394-401.

160. Dreizin, E.L., et al., *Particle combustion dynamics of metal-based reactive materials.* International Journal of Energetic Materials and Chemical Propulsion, 2011. **10**(4): p. 297-319.

161. Monk, I., M. Schoenitz, and E.L. Dreizin, *The effect of heating rate on combustion of fully dense nanocomposite thermite particles.* Combustion Science and Technology, 2018. **190**(2): p. 203-221.

162. Stamatis, D., A. Ermoline, and E.L. Dreizin, *A multi-step reaction model for ignition of fully-dense Al-CuO nanocomposite powders.* Combustion Theory and Modelling, 2012. **16**(6): p. 1011-1028.

163. Atkinson, A., *Transport processes during the growth of oxide films at elevated temperature.* Reviews of Modern Physics, 1985. **57**(2): p. 437-470.

164. Fehlner, F.P. and N.F. Mott, *Low-temperature oxidation.* Oxidation of Metals, 1970. **2**(1): p. 59-99.

165. Trunov, M.A., M. Schoenitz, and E.L. Dreizin, *Effect of polymorphic phase transformations in alumina layer on ignition of aluminium particles.* Combustion Theory and Modelling, 2006. **10**(4): p. 603-623.

166. Ermoline, A., D. Stamatis, and E.L. Dreizin, *Low-temperature exothermic reactions in fully dense Al-CuO nanocomposite powders.* Thermochimica Acta, 2012. **527**: p. 52-58.

167. Monk, I., et al., *Combustion characteristics of stoichiometric al-cuo nanocomposite thermites prepared by different methods.* Combustion Science and Technology, 2017. **189**(3): p. 555-574.

168. Mohan, S., M.A. Trunov, and E.L. Dreizin, *Heating and ignition of metal particles in the transition heat transfer regime.* Journal of Heat Transfer, 2008. **130**(10).

169. Vummidi, S.L., et al. *Characterization of fine aluminum powder coated with nickel as a potential fuel additive*. 2010. Orlando, FL.

170. Jeurgens, L.P.H., et al., *Structure and morphology of aluminium-oxide films formed by thermal oxidation of aluminium.* Thin Solid Films, 2002. **418**(2): p. 89-101.

171. Wright, P.G., *On the discontinuity involved in diffusion across an interface (the δ of Fuchs).* Discussions of the Faraday Society, 1960. **30**: p. 100-112.

172. Fuchs, N.A., *On the stationary charge distribution on aerosol particles in a bipolar ionic atmosphere.* Geofisica Pura e Applicata, 1963. **56**(1): p. 185-193.